Aus der Neurochirurgischen Klinik und Poliklinik

Klinik der Universität München

Direktor: Prof. Dr. Jörg-Christian Tonn

Paracrine humanin signaling promotes glioma chemoresistance

Dissertation

zum Erwerb des Doktorgrades der Medizin

an der Medizinischen Fakultät der

Ludwig-Maximilians-Universität zu München

vorgelegt von

Jiying Cheng

aus

Hunan, P.R. China

2023

Mit Genehmigung der Medizinischen Fakultät

der Universität München

Berichterstatter:	Prof. Dr. Rainer Glaß
Mitberichterstatter:	PD Dr. Bogdana Suchorska Prof. Dr. Karim-Maximilian Niyazi Prof. Dr. Nathalie Albert
Dekan:	Prof. Dr. med. Thomas Gudermann
Tag der mündlichen Prüfung:	26.10.2023

Table of Contents

Abstract

Transcriptomic analysis of human tumor-associated macrophages (TAMs) in glioblastoma (GBM) revealed the upregulation of the mitochondrial ribosomal subunit MT-RNR2, which contains an open reading frame for the signaling peptide Humanin (HN). Immunohistochemistry confirmed the high expression of HN in TAMs. *In vitro* assays with multiple human stem-like GBM cell lines disclosed that nanomolar range of HN can prompt tumor cell expansion and chemoresistance to temozolomide (TMZ). A series of experiments showed that HN binds to extracellular receptor GP130 (IL6ST) and stimulates MAPK (ERK)-related signaling pathway to enhance human glioma stem cell (GSCs) viability. Mechanistically, HN promoted the ATR-dependent DNA-repair machinery in GSCs via induction of the DNA-clamp component HUS1. Exogenous delivery or overexpression of HN in orthotopic GBM mouse models also confirmed HN effect in inducing chemoresistance to TMZ in GBM. Blockade of the GP130 with exogenous delivery of GP130 inhibitor SC144 or the brain permeant, FDA-approved drug bazedoxifene acetate blocked HN-mediated chemoresistance both *in vitro* and *in vivo*, and exhibited survival benefit. Overall, we identified a peptide that can induce the expansion of GBM and the chemoresistance to TMZ, which can be a potential predictive marker of chemoresistance to GBM.

Zusammenfassung

Transkriptomische Screenings von Hirntumor-Parenchymzellen zeigten tumorunterstützende Eigenschaften der Glioblastoms (GBM)-Mikroumgebung, schlossen aber mitochondrial angereicherte Gensätze weitgehend aus. Hier zeigten wir, dass das mitochondriale Transkript von GBM-Parenchymzellen zur Therapieresistenz beiträgt. Wir untersuchten das nicht-kodierende Transkriptom von menschlichen GBM-assoziierten myeloischen Zellen (TAM) und beobachteten eine Hochregulierung der mitochondrialen ribosomalen Untereinheit MT-RNR2, die ein ORF für das Signalpeptid Humanin (HN) enthält. In der Immunhistochemie ergab sich, dass HN vor allem in TAMs vorkommt. In-vitro-Tests bei einer Reihe von stammzellähnlichen GBM-Zellen menschlichen Ursprungs (GSC) ergaben, dass nanomolare HN-Konzentrationen die Expansion der Tumorzellen und die Chemoresistenz gegenüber Temozolomid (TMZ) fördern können. In einer Reihe von genetischen und pharmakologischen Experimenten sowie in Western-Blotting zeigten wir, dass extrazelluläres HN die Lebensfähigkeit von GSC durch Stimulation des GP130 (IL6ST)-Rezeptors und die MAPK (ERK)-Aktivierung erhöhen. Das Ansprechen auf HN unterlag einer interindividuellen Heterogenität und war vor allem bei GSCs mit hoher Expression der IL6ST-Untereinheit zu beobachten. Mechanistisch gesehen förderte HN die ATR-abhängige DNA-Reparaturmechanismen in GSCs über die Induktion der DNA-Clamp-Komponente HUS1. Durch die exogene Verabreichung von HN in orthotopen GBM-Mausmodellen oder durch die Überexpression, insbesondere einer sekretierten HN-Variante, konnten die in vitro-Befunde rekapituliert werden. Die Inhibierung des GP130 mit dem hirngängigen, von der FDA zugelassenen, Medikament Bazedoxifenacetat (BZA) bewirkte eine verminderte HN-vermittelte Chemoresistenz sowohl in vitro als auch in vivo. Insgesamt haben wir einen klinisch anwendbaren Wirkstoff und einen prädiktiven Marker zur Verhinderung von Chemoresistenz in einem humanspezifischen GBM-Modell identifiziert.

List of abbreviations

7-AAD	7-Amino-Actinomycin D
aCSF	Artificial cerebrospinal fluid
AD	Alzheimer‘s Disease
AMPK	Adenosine monophosphate-activated protein kinase
APP	Amyloid precursor protein
ATM	Ataxia telangiectasia, mutated
ATR	ATM and RAD3-related
BAK	BCL-2 antagonist or killer
BAX	BCL2-associated X protein
BBB	Blood brain barrier
BCL-2	B-cell lymphoma 2
BH3	BCL2 homology domain 3
BID	BH3-interacting domain death agonist
BIM	BCL2-interacting mediator of cell death
BIMEL	Extra long BIM
BMDMs	Bone marrow-derived macrophages
BSA	Bovine serum albumin
BZA	Bazedoxifene acetate
CCL2	C-C chemokine ligand 2
CCR2	C-C chemokine receptor type 2
cDNA	Complementary DNA
CHK	Checkpoint kinases
CNTFR	Ciliary neurotrophic factor receptor
CSF1	Colony-stimulating factor 1
CX3CL1	C-X3-C motif chemokine ligand 1
CX3CR1	C-X3-C motif chemokine receptor 1
DAB	3, 3'-diaminobenzidine

DAPI	4′,6-diamidino-2-phenylindole
EGF	Epidermal growth factor
eNOS	Endothelial nitric oxide synthase
ERK	Extracellular signal-regulated kinases
FACS	Fluorescence-activated cell sorting
FAD	Familial AD
FCRLS	Fc receptor-like S, scavenger receptor
FDA	US Food and Drug Administration
FGF	Fibroblast growth factor
fMLF	Formyl-methionyl-leucyl-phenylalanine
FPR	Formylpeptide receptor
FPRL1	FPR like-1
GBM	Glioblastoma multiforme
GDNF	Glial cell-derived neurotrophic factor
GFP	Green fluorescence protein
GM-CSF	Granulocyte macrophage colony-stimulating factor
GP130	Glycoprotein 130
GPR34	G protein-coupled receptor 34
GSCs	Glioma stem cells
GSK-3β	Glycogen synthase kinase-3β
GTEx	The Genotype-Tissue Expression
HEXB	Hexosaminidase subunit beta
hiPSC-MG	Human microglia-like cells from induced pluripotent stem cells
HN	Humanin
HNG	Humanin-S14G
IBA1	Ionized calcium-binding adapter molecule 1
IFN-γ	Interferon-γ
IGFBP	Insulin-like growth factor binding protein
IL	Interleukin

JAK	Janus kinase
JNK	C-Jun N-terminal kinase
LPS	Lipopolysaccharide
Ly-6C	Lymphocyte antigen 6 complex
LYVE-1	Lymphatic vessel endothelial hyaluronan receptor 1
MCL-1	Myeloid-cell leukemia 1
MDSC	Myeloid-derived suppressor cell
MEK	Mitogen-activated protein kinase kinase
MIC-1	Macrophage inhibitory cytokine-1
MRC1	Mannose receptor C-type 1
mRNA	Messenger RNA
MTOC	Multiple microtubule organizing centers
NADPH	Nicotinamide adenine dinucleotide phosphate
OPN	Osteopontin
ORF	Open reading frame
ox-LDL	Low density lipoprotein
P2RY12	Purinergic receptor P2Y12
p75NTR	75kDa neurotrophin receptor
PBS	Phosphate buffered saline
PDGFB	Platelet derived growth factor subunit B
PDGFRβ	Platelet-derived growth factor receptor beta
PFA	Paraformaldehyde
PI3K	Phosphatidylinositol-3-kinase
PU.1	Purine-rich box1
qPCR	Quantitative PCR
RNAseq	RNA sequencing
rRNA	Ribosomal RNA
SALL-1	Spalt-like transcription factor 1
SLC2A5	Solute carrier family 2 member 5

SOCS3	Suppressors of cytokine signaling 3
STAT3	Signal transducer and activator of transcription 3
STI1	Stress-inducible protein 1
TAMs	Tumor-associated macrophages
TCGA	The Cancer Genome Atlas
TEK-2	Tunica interna-endothelial cell kinase 2
TGF-β	Transforming growth factor-beta
TMEM119	Transmembrane protein 119
TMZ	Temozolomide
VEGF	Vascular endothelial growth factor
WHO	World Health Organization

List of figures

List of tables

1. Introduction

1.1 Glioblastoma

Gliomas are the most common primary intracranial tumors[1]. They account for approximately 30% of all intracranial tumors and more than 80% of all malignant brain tumors[2]. According to their histological features, gliomas can be classified into astrocytomas, oligodendrogliomas, and ependymomas[3]. Gliomas are also categorized by grade (I to IV) according to the World Health Organization (WHO) Classification of Tumors of the Central Nervous System based on pathological evaluation, with WHO grade I indicating low risk and surgically removable tumors and WHO grade IV referring to malignant tumors with poor prognosis[4]. Glioblastoma multiforme (GBM) is a WHO-grade IV astrocytoma and the most common and aggressive primary intracranial tumor, with a median survival of approximately 16 months[5]. Previously, GBM was classified into four subtypes according to its bulk transcriptional profile: classical, neural, proneural, and mesenchymal[6]. However, this has been revised, as the neuronal subtype is largely defined by cells from the tumor environment[7]. Recently, based on an integrative approach combining bulk sequencing using The Cancer Genome Atlas (TCGA) dataset, single-cell RNA sequencing (RNAseq), and lineage tracing of glioblastoma models, researchers revealed that GBM cells share similarity with a limited set of cellular states: neural progenitor-like, oligodendrocyte-progenitor-like, astrocyte-like, and mesenchymal-like[8]. This provides a more profound view of the heterogeneity of GBM, in which each tumor contains cells in multiple states and cellular states can dynamically alter to one or another. GBM is characterized by high infiltration of resident microglia and recruitment of macrophages from the periphery, as well as extensive invasiveness of tumor cells to neighboring healthy tissue[9, 10]. The complexity and heterogeneity of the tumor microenvironment, as well as the formation of chemoresistance, contribute to the poor prognosis of glioblastoma[11, 12].

1.2 Tumor microenvironment

The expansion of tumor cells relies on their close interactions with the microenvironment[13, 14]. In general, GBM consist of tumor cells, glioma stem cells (GSCs), immune cells such as resident microglia, bone marrow-derived macrophages (BMDMs), dendritic cells, granulocytes and lymphoid cells, as well as non-immune cells including astrocytes, endothelial cells, and pericytes. Each component plays a role in the tumor mass and may influence therapeutic results[8, 15-19]. Tumor-associated macrophages (TAMs) are an abundant population in GBM, accounting for more than 30% of the tumor mass and have a negative impact on patient survival[20, 21].

There are two types of macrophages in the tumor microenvironment: BMDMs and brain-resident macrophages, namely microglia. Microglia migrate from the yolk sac to the central nervous system during embryogenesis and self-renew in the brain[22, 23]. Under physiological conditions, microglia account for up to 20% of the glial cell population and play an important role in sustaining the neural network development, clearance of apoptotic cells, and immune surveillance[24, 25]. After pathological insults monocytes can infiltrate the brain through blood vessels and differentiate into BMDMs[26]. Alhough microglia and BMDMs have two distinct origins, they exhibit several similar features. Microglia and BMDMs have several common markers, such as ionized calcium-binding adapter molecule 1 (IBA1), F4/80, purine-rich box1 (PU.1), CD11b and CD68[27-29]. Earlier studies suggested that it may be possible to distinguish microglia from BMDMs through their CD45 and CD11b expression levels, with $CD11b^{high}/CD45^{low}$ indicating resident microglia and $CD11b^{high}/CD45^{high}$ indicating BMDMs[30, 31]. However, it is important to note that CD45 levels can be upregulated during inflammation, experimental autoimmune encephalomyelitis, glioma, and aging[32-34]. Another study using immunostaining for the C-X3-C motif chemokine receptor 1 (CX3CR1) or the C-C chemokine receptor type 2 (CCR2) showed that most TAMs were $CCR2^{+}$ $CX3CR1^{-}$ BMDMs and, to a lesser extent, $CCR2^{-}CX3CR1^{+}$ resident microglia[35]. This method was challenged because others have later demonstrated that CX3CR1 expression was also detectable in BMDMs, and

the expression level increased when BMDMs differentiated into macrophages[36]. Recently, an increasing number of microglia-specific markers have been identified, such as the purinergic receptor P2Y12 (P2RY12), transmembrane protein 119 (TMEM119), spalt-like transcription factor 1 (SALL-1), solute carrier family 2 member 5 (SLC2A5), Fc receptor-like S, scavenger receptor (FCRLS), G protein-coupled receptor 34 (GPR34) and hexosaminidase subunit beta (HEXB), among which only HEXB is stably expressed in both physical and pathological conditions[37-43]. Markers such as lymphatic vessel endothelial hyaluronan receptor 1 (LYVE-1), CD163, mannose receptor C-type 1 (MRC1) and CD206 have also been identified in macrophages located in specific regions, such as perivascular and meningeal macrophages, also referred to as border-associated macrophages[41-44].

The contributions of microglia and BMDM in GBM tissue differ depending on the strategies used to distinguish these two types of cells, the tumor model used in different studies, and the observation time point in tumor progression. In studies where CD45 levels were used for the discrimination of microglia and BMDM, it was reported that more microglia occur in early tumor progression and BMDMs gradually increase in later phases, but remain less frequent than microglia, in mouse and rat xenograft tumor models[31, 45, 46]. In other studies where a genetically modified DF-1 cell line with platelet-derived growth factor subunit B (PDGFB) transfection was used as a GBM model in mice, researchers observed that, based on either CD45 expression level or transgenic mouse model (*Cx3cr1*$^{GFP/+}$*Ccr2*^{RFP}), infiltrating macrophages can occupy up to 83% of the myeloid population at the end-point of tumor-bearing mice[47]. In chimeric models generated through busulfan application and bone marrow transplantation, the results differed depending on busulfan dosage[48]. A higher concentration of busulfan induced more BMDMs in the tumor mass as well as in the naive brain, indicating that busulfan administration alone can cause non-specific infiltration of BMDMs.

In GBM, TAMs are recruited to the tumor area through multiple mechanisms. Osteopontin (OPN) is a chemokine secreted by tumor cells and bind to integrin αvβ5 on TAMs, thereby stimulating the recruitment of TAMs and crosstalk between tumor cells and TAMs[49]. Other tumor-secreted cytokines that play important roles in TAM recruitment include the C-X3-C motif chemokine ligand 1 (CX3CL1), glial cell–derived neurotrophic factor (GDNF), granulocyte macrophage colony-stimulating factor (GM-CSF), colony-stimulating factor 1 (CSF1), and macrophage inhibitory cytokine-1 (MIC-1)[10]. TAMs in the GBM microenvironment can further attract more macrophages to the tumor area. Chemokine C-C chemokine ligand 2 (CCL2) is mainly produced by BMDMs especially $CD163^+$-infiltrating macrophages, and resident microglia in the tumor microenvironment, and is critical for the recruitment of $CCR2^+$ lymphocyte antigen 6 complex $(Ly\text{-}6C)^+$ monocytic myeloid-derived suppressor cells (MDSCs) which block anti-tumor immunity and induce immunosuppression[50]. Elevated expression of CCL2 in GBM is related to reduced overall survival[51]. The blockade of CCL2/CCR2 was shown to prolong survival in experimental mouse glioma models[52, 53]. Tumor cells secrete chemokines to attract TAMs; TAMs, in turn, release factors that support tumor progression and invasion, such as interleukin (IL)-6, IL-1β, epidermal growth factor (EGF), transforming growth factor-beta (TGF-β), and stress-inducible protein 1 (STI1) [21].

The distribution of TAMs is highly heterogeneous both spatially and temporally. A higher TAMs density is observed in the tumor center than in the infiltration area, and also an accumulation of TAMs in perivascular regions is often observed[54]. Microglia are mainly located at the tumor border, whereas BMDMs are largely confined to the tumor mass[47, 55]. Previous studies have indicated that TAMs polarize into two categories upon activation: M1 pro-inflammation phenotype and M2 anti-inflammation phenotype[56]. This classification was introduced based on the *in vitro* stimulation of different cytokines, where the M1 phenotype is induced by lipopolysaccharide (LPS)/interferon-γ (IFN-γ) and M2 is induced by IL-10/IL-4[57]. In early studies, TAMs in GBM were considered to mainly adopt the M2 phenotype, representing a pro-

tumoral and immunosuppressive identity[58]. However, recent studies have shown that this classification is oversimplified because even if a macrophage adopts one phenotype, it still maintains the potential to reverse the polarization status. Also, there are intermediate stages between the extremes of the M1/M2 classification[59-62].

In addition to the direct crosstalk between tumor cells and TAMs, TAMs can affect other components in the tumor microenvironment. For example, TAMs affect the stability of the vasculature and blood-brain barrier (BBB) in tumor masses[63, 64]. TAMs can express vascular endothelial growth factor (VEGF) to promote angiogenesis and increase BBB permeability[64]. In addition, TAMs can produce inflammatory IL-1β and induce non-integrity of the BBB, thus causing edema in GBM, which can be blocked by dexamethasone[65]. In addition, tunica interna-endothelial cell kinase 2 $(TEK\text{-}2)^{+}$ TAMs located in the perivascular area enhance the growth of *de novo* endothelial cells by releasing IL-6[66].

1.3 GBM and DNA repair

The strong resistance of GBM to chemotherapy and radiotherapy is a main reason for the poor survival in patients, and one of the key factors that drives chemoresistance is the DNA damage repair system in tumor cells[67]. Under physiological conditions, this protective system maintains the stability of genetic information in homeostatic or proliferative cells over generations[68]. However, in a pathological context, the repair system counteracts treatments that aim to damage DNA and destroy tumor cells[69]. When DNA damage occurs, one initial reaction of the repair system is to arrest the cell cycle, which provides time to initiate DNA repair. At this point cells may still be forced to undergo apoptosis when DNA damage is too extensive and therefore not repairable[70]. Temozolomide (TMZ) is one of the most commonly used chemotherapeutics for GBM patients. TMZ causes DNA single-strand damage and halts DNA replication[71]. Important kinases involved in the DNA stress response are ataxia telangiectasia mutated (ATM) and ATM and RAD3-related (ATR) kinases, which are recruited to the site of DNA damage, and activate checkpoint kinases 1 and

2 (CHK1 and CHK2), subsequently slowing the cell cycle[72]. Cell fates are determined according to the severity of DNA damage, as well as the cellular sensitivity of the damages. Cells can become senescent, exit the cell cycle, enter apoptotic programs, or enter/continue the cell cycle, after DNA repair. Most of the long-term cell arrests in S or G2/M phase result in irreversible exits of the cell cycle, after which cells either become senescent or undergo apoptosis. In contrast, cell arrest in the G1 phase can result in senescence or quiescence[73-75].

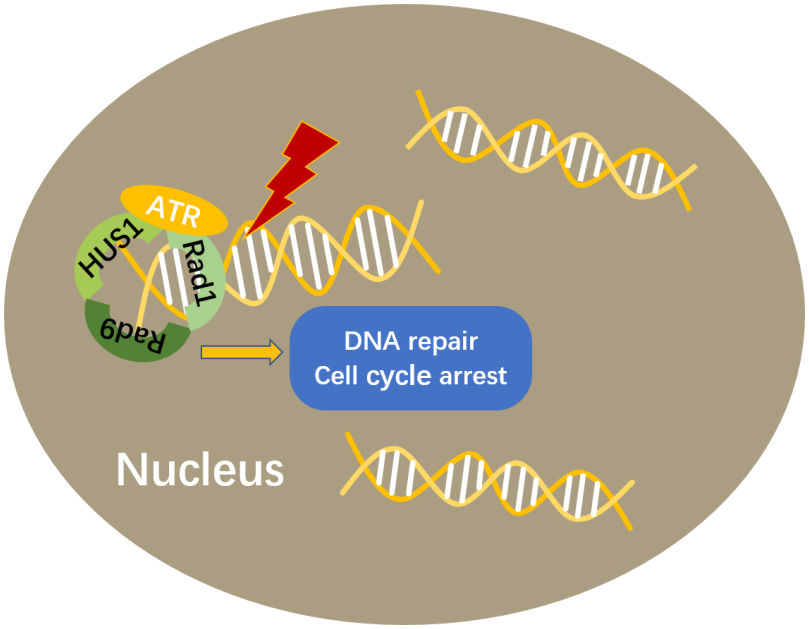

Figure 1. 3: HUS1 /ATR-dependent DNA repair mechanisms. The repair of DNA damage is controlled by the ATR, which is recruited to stalled or collapsed replication forks together with the 9-1-1 (Rad9-Rad1-HUS1) DNA clamp complex. These molecules cooperatively enable a time window for DNA repair and promote recovery from a DNA replication arrest.

1.4 Humanin

The peptide Humanin (HN) was discovered in 2001 when researchers studied neurons that survive in Alzheimer's disease (AD) by using death-trap screening of amyloid precursor protein (APP) mutant-expressing neuronal cells transfected with a complementary DNA (cDNA) library based on the occipital lobe of an AD patient where an area remained intact during the disease[76].

1.4.1 The structure of Humanin

HN is a 24 amino acid peptide encoded by mitochondrial DNA MT-RNR2 (16S ribosomal RNA [rRNA])[77, 78]. Previous study has shown that there are HN messenger RNA (mRNA)-liked sites on both mitochondrial genome and nuclear genome. However, the size of HN mRNA is more identical to HN mRNA-liked sequence on mitochondrial DNA[79]. Besides, the difference between HN mRNA and HN mRNA-liked site on nuclear genome is in the open reading frame (ORF) of HN, which is of great importance for the transportation of HN across the endoplasmic reticulum, whereas the difference between HN mRNA and HN mRNA-liked site on mitochondrial DNA presents outside of the HN-ORF[78, 79]. Moreover, mitochondria-specific translation inhibitors, rather than cytoplasmic ones, decrease HN levels[80]. These evidences indicate that the HN encoding sequence is in mitochondria, rather than in nuclei.

The primary structure of HN plays an essential role in its bioactivity such as its protective effects against familial AD (FAD) gene-induced cytotoxicity and the secretion of HN[77]. Various amino acid residues play distinct roles in HN signaling; for example, the cysteine on position 8 and serine on position 14 is essential for the protective effect against FAD-induced cytotoxicity and the leucine on position 9 is important for peptide secretion. The substitution of different amino acids in HN was used to study their mechanism of action. Neuronal cells transfected with HN-L9R, which cannot be secreted, showed no neuroprotective effects[81]. When applied as a synthetic peptide, HN-L9R can suppress neuronal cell death, indicating that HN functions through paracrine[76]. HN-S14G (HNG), an HN derivative in which the serine in position 14 is replaced by glycine, has 1000-fold higher neuroprotective efficiency against FAD than HN[82]. Nuclear magnetic resonance revealed structural alterations in some more efficient derivatives, such as HNG and HN-DSer14[83]. The difference in cytoprotective efficiency between HN and its derivatives may be due to their structural stability under physiological temperature[84], as well as their homodimerization and isomerization efficacy[85].

1.4.2 The expression of Humanin

In human tissues, HN-ORF-hybridizable polyA+ RNA has been detected in various organs, such as the heart, kidneys, liver, skeletal muscles, gastrointestinal tract, and brain. Brain expression is higher in the cerebellum and occipital lobe, which are also found to remain intact during AD attack[76, 77]. In mice, HN expression was found in colon and testis of young mice using Western Blotting and in AD neurons and glia using immunohistochemistry[78].

1.4.3 Humanin receptors and interacting proteins

◆ Intracellular interacting proteins

HN interacts with different members of the B-cell lymphoma 2 (BCL-2) family which bind to the outer mitochondrial membrane and are essential for the regulation of apoptosis[86]. One of the BCL-2 members is BCL2-associated X protein (BAX), which plays a pro-apoptotic role in physiology and pathology. It remains in the cytoplasm in an inactive state, and moves to the mitochondria under lethal stress, for example, when sensing the release of apoptogenic proteins[87]. HN can interact with BAX, suppress the translocation of BAX, and therefore block the cytotoxicity triggered by some BAX-involving mechanisms, such as Aβ-induced cytotoxicity and serum deprivation *in vitro* [88, 89]. Moreover, the interaction between HN and BAX does not depend on extracellular receptors[90]. Other members of the BCL-2 family are BCL2 homology domain 3 (BH3)-interacting domain death agonist (BID) and BCL2-interacting mediator of cell death (BIM), of which the latter has three isoforms short BIM, long BIM and extra long BIM (BIMEL) depending on the mRNA splicing variety. HN inhibits the pro-apoptotic effect of BIMEL and BID, independent of BAX, by counteracting the BIMEL-induced release of mitochondrial apoptosis-related proteins and inhibiting the oligomerization of BCL-2 antagonist or killer (BAK) which destabilize the mitochondrial membrane, indirectly resulting in decreased release of cell death-related proteins[89, 91, 92].

Another intracellular HN-interacting protein is insulin-like growth factor (IGF)-binding protein-3 (IGFBP-3). IGFBP-3 is part of the IGF axis, which has been shown to be of great importance in maintaining cell proliferation and inhibiting apoptosis under physiological conditions, as well as in some diseases, such as cancer[93, 94]. IGFBPs function in both an IGF-dependent and IGF-independent manner. By binding to IGFBPs, IGFs extend their half-life in the circulation to 30–90 min depending on the IGF subtype. IGFBPs function in an IGF-independent manner by binding to integrin receptors and many other proteins that affect cell function, such as type V TGF-β receptor and receptor protein tyrosine phosphatase β[95]. IGFBP-3 is mostly secreted by the liver under normal conditions, whereas under pathological conditions, its level was found to be increased in tumors of breast cancer and GBM[96, 97]. IGFBP-3 binds to cell surface receptors to enter cells and translocate into the nucleus where it functions by interacting with ligand-dependent transcription factors[98]. IGFBP-3 has also been reported to interact with HN, as well as some non-cytoprotective HN mutants. The binding domain of IGFBP-3 for HN is located within its C-terminal domain. At a low concentration, IGFBP-3 does not affect the viability of cells and potentiates the protective effect of HN against neuronal cell death induced by Aβ1-43. When present at higher concentrations, IGFBP-3 causes cell apoptosis; however, this can be blocked by HN[99]. The interaction between HN and IGFBP-3 is regulated by importin-β[100]. Reports show that IGFBP-3 is highly expressed in GBM, but whether HN interacts with IGFBP-3 in GBM remains unclear[101]. In addition, growth hormones and IGF-1 are potent negative HN regulators[102]. Prolyl endopeptidase is a possible HN-degrading enzyme that regulates the homeostasis of intracellular HN[103].

◆ Extracellular receptors

In addition to the above-mentioned intracellular function, HN can also be secreted, controlled by an intracellular endoplasmic reticulum-Golgi transport mechanism[77]. HN can stimulate the membrane formylpeptide receptor (FPR). In humans, the FPR family was originally found in myeloid cells that have a high affinity for the chemotactic peptide formyl-methionyl-leucyl-phenylalanine (fMLF) produced by

bacteria. FPR responds to low concentrations of fMLF, whereas FPR like-1 (FPRL1) responds to higher concentrations[104]. In mice, the corresponding analogs are defined as FPR1 and FPR2. FPRL1 and murine homolog FPR2 are expressed on monocytes and microglia and can mediate the activation and endocytosis of cells upon Aβ42 attack[105]. HN was confirmed to rescue Aβ-induced cytotoxicity by competitively binding to human FPRL1 and mouse FPR2 and activating the downstream pathway mediated by extracellular signal-regulated kinases 1/2 (ERK1/2)[106].

Glycoprotein 130 (GP130) is an important subunit of many cytokine receptors, and it has been reported that GP130 inhibition is a potential treatment for GBM [107, 108]. Ciliary neurotrophic factor receptor (CNTFR) may dimerize with the interleukin-27 receptor (IL-27R, WSX-1), and then hetero-trimerize with GP130 to form a complex to mediate HN effect; it is also possible that only two subunits of the three receptors assemble to accept signals from HN[109]. In response to this, the Janus kinase/ signal transducer and activator of transcription 3 (JAK/STAT3) axis, possibly together with multiple other JAK cascades such as JAK/phosphatidylinositol-3-kinase (PI3K)/AKT and JAK/mitogen-activated protein kinase kinase (MEK)/ERK signaling pathways[110], are activated, as GP130 usually simultaneously activates various pathways.

The 75kDa neurotrophin receptor (p75NTR) is a Gi protein-coupled receptor that induces Aβ neuronal death through downstream signaling involving c-Jun N-terminal kinase (JNK), nicotinamide adenine dinucleotide phosphate (NADPH) oxidase, and caspase-3. The P75-like apoptosis-inducing death domain, which shares a similar structure with p75NTR in transmembrane and intracellular domains, heterodimerizes with p75NTR and facilitates neurotoxicity triggered by Aβ through the Gi rather than Go protein. HN can bind to p75NTR and block apoptosis through the afore mentioned mechanism[111]. Studies have also shown that p75NTR is associated with resistance

to GBM therapy[112, 113]. However, it is unclear whether HN participates in the establishment of resistance.

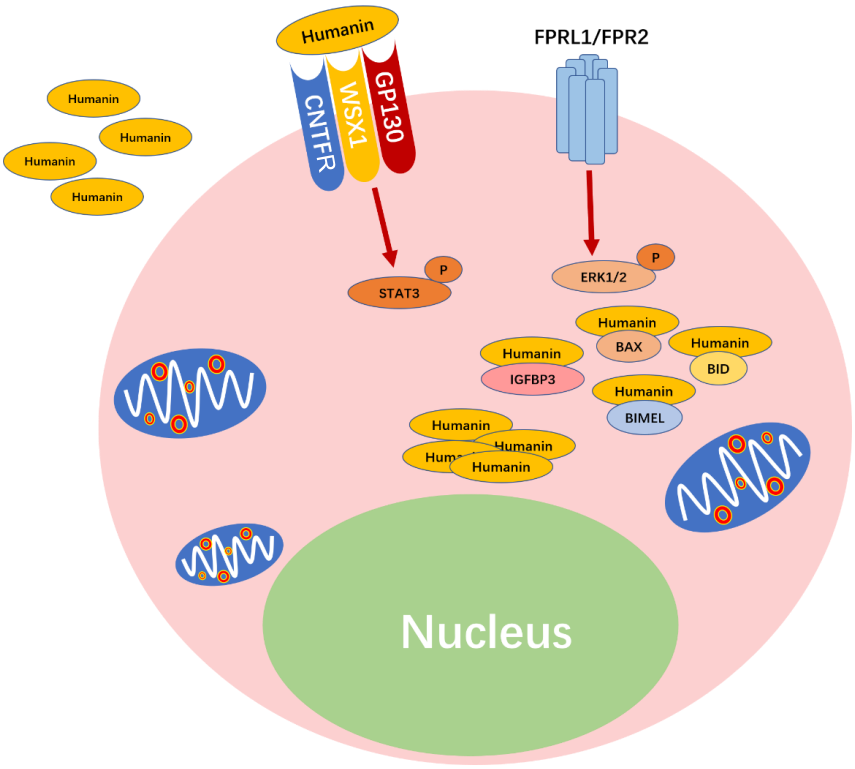

Figure 1.4.3: Humanin intracellular and extracellular binding partners and associated signaling pathways. HN is transcribed from mitochondrial genome, and act on both intracellular and extracellular proteins. Intracellular binding partners include BAX, BID, and IGFBP3. Receptors on cell surface are trimeric CNTFR/WSX1/GP130 and FPRL1/FPR2. Downstream signaling pathways are STAT3 and ERK1/2 involved pathways.

1.4.4 Humanin and diseases

◆ Humanin and cardio-cerebrovascular disease

HN can rescue human cerebrovascular smooth muscle cells from Aβ-induced cell death[114]. HN in the circulation modulates coronary endothelial cell function and protects vascular endothelial cells from hyperoxia, oxidative stress induced by oxidized low density lipoprotein (ox-LDL), and apoptosis caused by high blood glucose[115-118]. HNG helps to lower cholesterol levels and to decrease ox-LDL uptake in macrophages, thereby repressing the formation of foam cells in atherosclerosis[119]. HN is highly expressed in several cell types in unstable carotid plaques[120]. It prevents

atherosclerotic plaque progression in hypercholesterolemic apolipoprotein E-deficient mice[121]. HN and HNG protect the brain and heart from cerebral and myocardial ischemia/reperfusion injury in mice through the suppressors of cytokine signaling 3 (SOCS3)/STAT3/ myeloid-cell leukemia 1 (MCL-1) axis, ERK and PI3K/AKT pathways, and the adenosine monophosphate-activated protein kinase (AMPK)/ endothelial nitric oxide synthase (eNOS)-related pathway[122-131]. Oligodendrocytes are protected in a hypoxic/ischemic neonatal model through HNG pre-treatment[132]. In addition, HNG improves recovery outcomes after traumatic brain injury and intracerebral hemorrhage through the PI3K-AKT/ glycogen synthase kinase-3β (GSK-3β) signaling pathway in mice[133, 134].

◆ Humanin and cancer

HN protects cells from damage during chemotherapy. Bortezomib, a proteasome inhibitor, is widely used in the treatment of cancers, such as mantle cell lymphoma and multiple myeloma[135, 136]. However, as an anticancer medication, it has some side effects such as bone growth impairment, which can be reduced by the administration of HNG without influencing the anticancer effects[137]. In addition, HNG enhances the cardiac protective effect of dexrazoxane against toxicity induced through the chemotherapeutic drug doxorubicin[138]. Moreover, HN ameliorates male germ cell apoptosis caused by chemotherapy[139] and strengthens chemotherapy-induced tumor suppression[140]. However, HN can also protect tumor cells. Previous research has shown that HN exhibits a pro-tumor effect in breast cancer and impairs the efficiency of chemotherapy[141]. Rattin, a rat homolog of HN, is expressed in physiological pituitary cells as well as in pituitary tumors, and blocks the pro-apoptotic effect of tumor necrosis factor alpha (TNF-α) on pituitary cells[142]. Silencing HN increases the apoptosis of pituitary tumor cells and enhances the survival rate in animal experiments[143]. Moreover, HN was overexpressed in gastric cancer revealed by suppression subtractive hybridization, in which HN plays a role in chemoresistance[144]. Similarly, 16S rRNA transcription is upregulated in lymphomas, in which HN is a potential oncopeptide[79].

1.5 Study aims

By comparing fluorescence-activated cell sorting (FACS)-purified macrophages from GBM patient-derived biopsies to microglia from tumor-free human brains (obtained during resection of hippocampal sclerosis), we identified 100 differentially expressed genes, among which we observed the mitochondrially encoded 16S rRNA (MT-RNR2), which contains a small ORF for the peptide HN. Immunofluorescence staining confirmed increased expression of HN. To determine the role of HN in GBM, we asked the following questions:

a) Is MT-RNR2 translated into HN?
b) Do tumor cells have HN receptors?
c) Does HN exert cytoprotective effects on GBM cells?
d) Which receptor does HN bind to in GBM cells? Is HN a paracrine or an intracellular signaling core in GBM?
e) Which signaling pathways does HN activate?
f) Does HN affect other components in the tumor microenvironment? Does it induce protection of tumor cells and resistance to chemotherapy?
g) Is HN signaling a therapeutic target in GBM?

2. Materials

2.1 Devices

Table 2.1 Devices

Devices	**Company**
Balances-AG204	Mettler Toledo
Balances-MonoBloc	Mettler Toledo
BD Calibur	BD Bioscience, San Jose, CA
Becherglas (250, 500, 1000 mL)	DURAN Group GmbH, Wertheim, Germany
Centrifuge	Thermo Fisher Scientific
Centrifuge 5415R	Eppendorf AG, Hamburg, Germany
Clamp Mount Micromanipulators	ADInstruments
Clean Bench	Thermo Fisher Scientific, Waltham, MA, USA
CO_2 incubators	BINDER, Tuttlingen, Germany
Countess II FL Automated Cell Counter	Thermo Fisher Scientific
Digital Vortex mixer	VWR, Radnor, Pennsylvania, USA
DOSE IT peristaltic pump	Integra Biosciences AG, Zizers, Switzerland
Drying block	Whatman GmbH, Dassel, Germany
Fridge (4°C, -20°C, -80°C)	LIEBHERR, Bulle, Switzerland
Magnetic Hotplate Stirrer VMS-C7-2	VWR International GmbH, Darmstadt, Germany
Menzel microscope coverslips (24 × 50 mm)	Gerhard Menzel GmbH, Braunschweig, Germany
Microliter syringe (1 µL)	Hamilton Company, Reno, NV, USA

Micropipette (10 µL, 20 µL, 100 µL, 200 µL, 1000 µL)	Eppendorf
Microwave	Siemens
MS2 mini shaker	IKA, Staufen, Germany
Perfusion system Dose IT P910	Integra Biosciences
Pipet Boy Comfort	Integra Biosciences AG, Zizers, Switzerland
Pipet-Aid XP2	Drummond Scientific Company, Pennsylvania, United States
Sea Star Shaker	Biozyme Scientific GmbH, Oldendorf, Germany
Slide 2003 Microtome	Pfm Medical, Cologne, Germany
Stereotactic Frame	Stoelting Co., Wood Dale, IL, USA
Surgical instruments	Medizinisches Lager Klinikum der Universität München, Munich, Germany
Water bath	Memmert GmbH + Co. KG, Schwabach, Germany
WTW Multical bench pH Meter (pH 526)	Sigma-Aldrich, Saint Louis, MO, USA

2.2 Consumables

Table 2.2 Consumables

Consumables	**Company**
µ Columns #130-042-701	Miltenyi Biotec, USA
µMACS^{TM} Separator	Miltenyi Biotec, USA
µ-Slide 8 well ibidi #80827	ibidi GmbH, Germany
8-well culture slide	Falcon
Alzet Brain Infusion Kit 3	ALZET
Alzet Osmotic Pump Model 1002	ALZET
BD Microlance^{TM} 3	Becton Dickinson

Centrifuge Tube (15, 50 mL)	TPP Techno Plastic Products AG, Trasadingen, Switzerland
Costar Stripettes (5, 10 and 25 mL)	Corning Incorporated, Corning, NY, USA
Cover slips	Gerhard Menzel
Dako Pen	Dako Germany, Hamburg, Germany
Eppendorf tubes (0.5, 1 and 2 mL)	Eppendorf AG, Hamburg, Germany
Ethibond excel (5-0)	Ethicon, Germany
Falcon tubes (15 and 50 mL)	VWR International GmbH, Darmstadt, Germany
Falcon® Cell strainer 40 µm #352340	Life science, Durham, USA
Greiner Cryo.S™ vials	Greiner Bio-one GmbH, Frickenhausen, Germany
Microtome Blade A35	Feather
Parafilm	Biozym Scientific GmbH, Hessisch Oldendorf, Germany
Pipette Tip (0-10, 20-200, 100-1000 µL)	Gilson S.A.S, Villiers-le-Bel, France
Pipettes (0-10, 20-200, 100-1000 µL)	Eppendorf AG, Hamburg, Deutschland
Round glass coverslip 10 mm	Menzel GmbH & Co KG
Safe-Lock Tubes 1.5 mL	Eppendorf AG, Hamburg, Germany
Scalpel (#15, #23)	Feather
Single use filter unit 0.2 µm #7699822	LABSOLUTE, Th. Geyer GmbH & Co. KG
Spritzen BD Discardit II (5 and 10 mL)	Becton Dickinson, Franklin Lakes, NJ, USA
STRIPETTE (5, 10, 25, 50 mL)	Corning, New York, USA

Superfrost Ultra Plus microscope slides	Thermo Fisher Scientific, Waltham, MA, USA
Syringe (1 mL, 5 mL, 10 mL, 50 mL)	B. Braun Melsungen AG
Syringe needle (20G, 21G, 27G, 30G)	B. Braun Melsungen AG
Tissue culture flasks (T25, T75, T150)	TPP Techno Plastic Products AG, Trasadingen, Switzerland
Tissue culture plate (12, 24, 96 well)	TPP Techno Plastic Products AG, Trasadingen, Switzerland
Tissue-Tek Cryomold (15 mm×15 mm×15 mm)	Sakura Finetek

2.3 Cell culture materials

Table 2.3 Cell culture materials

Medium/ reagent	**Company**	**Catalogue number**
Aqua (sterilized)	B.Braun Melsungen AG, Melsungen, Germany	6724092.00.00
B-27 supplement(50 ×)	Gibco, NewYork, USA	17504-044
DMEM/F12 Medium	Gibco, NewYork, USA	11320-74
Dulbecco's MEM (DMEM)	Biochrom GmbH, Berlin, Germany	FG0415
Fetal Bovine Serum (FBS)	Biochrom GmbH, Berlin, Germany	S0615
hEGF	PeproTech GmbH, Hamburg, Germany	AF-100-15
hFGF	PeproTech GmbH, Hamburg, Germany	100-18B

MEM Non-Essential Amino Acids Solution (100 ×)	Life Technologies, New York, USA	11140-050
PBS (sterilized)	Apotheke Klinikum der Universität München, Munich, Germany	L20170802-03
Penicillin-Streptomycin (P/S)	Life Technologies, Bleiswijk Netherlands	10378-016
StemPro Accutase Cell Dissociation Reagent	Gibco, NewYork, USA	A11105-01
Trypan Blue solution	Sigma, UK	T8154
Trypsin/EDTA solution(10 ×)	Biochrom GmbH, Berlin, Germany	L2153

2.4 Reagents and chemicals

Table 2.4 Reagents and chemicals

Reagents and chemicals	**Company**
[Gly14]-Humanin (HNG) #H54838	Designer BioScience
µMACS Protein A Microbeads #130-071-001	Miltenyi Biotec, USA
0.9% NaCl (sterilized)	B.BRAUN Melsungen AG, Melsungen, Germany
Aceton #5025.1	Roche Diagnostics GmbH, Rotkreuz, Switzerland
Aqua ad injectabilia	B. Braun Melsungen AG, Melsungen, Germany
AZ20 #5198	Tocris Bioscience, Bristol, UK
Bazedoxifene acetate #PZ0018	Sigma-Aldrich, Saint Louis, MO, USA

Bepanthen® Eye- and Nose- cream	Bayer HealthCare, Leverkusen, Germany
Braunol® #3864154	B. Braun Melsungen AG, Melsungen, Germany
Bovine Serum Albumin, Fraction V #9048-46-8	BIOMOL GmbH, Hamburg, Germany
$CaCl_2 \cdot 2H_20$	Carl Roth GmbH + Co. KG, Karlsruhe, Germany
Citric acid # C0759	Sigma-Aldrich, Saint Louis, MO, USA
Corn Oil #C8267	Sigma-Aldrich, Saint Louis, MO, USA
Cryomatrix	Thermo Fisher Scientific, Waltham, MA, USA
DAB-DC135c006	DCS Labline
DAB-substrate-PC136R100	DCS Labline
Dako Antibody Diluent #S3002	Dako Germany, Hamburg, Germany
Dako Biotinylated link #0690	Dako Germany, Hamburg, Germany
Dako Cytomation Pen #S2002	Dako Germany, Hamburg, Germany
DAPI	Sigma Aldrich
Dimethyl sulfoxide (DMSO) #D5879	Sigma-Aldrich, Saint Louis, MO, USA
Donkey serum	Sigma-Aldrich, Saint Louis, MO, USA
Entellan® mounting medium	Merck, Darmstadt, Germany
Eosin G-solution 0.5%	Carl Roth GmbH + Co. KG, Karlsruhe, Germany
Ethylene glycol	Sigma-Aldrich, Saint Louis, MO, USA
EtOH 70%	Apotheke Klinikum der Universität München, Munich, Germany
EtOH 96%	Apotheke Klinikum der Universität München, Munich, Germany
EtOH 99%	Apotheke Klinikum der Universität München, Munich, Germany

G418 Disulfate #A6798,0050	PanReac AppliChem, Darmstadt, Germany
Glycerol	Sigma-Aldrich, Saint Louis, MO, USA
HCl	Sigma-Aldrich, Saint Louis, MO, USA
Human EGFR Phosphorylation Array #AAH-PER-1-4	RayBiotech.Inc, GA, USA
Human RTK Phosphorylation Array #AAH-PRTK-1-4	RayBiotech.Inc, GA, USA
Humanin #H51588-0005	Designer BioScience
Hydrogen peroxide #K44176709 304	Merck KGaA, Darmstadt, Germany
Isopropanol #9866.6	Roche Diagnostics GmbH, Rotkreuz, Switzerland
KCl	Sigma-Aldrich, Saint Louis, MO, USA
Ketaminhydrochlorid (Ketavet, 100 mg/mL)	Pfizer, New York City, NY, USA
Lipofectamine® 3000 Transfection kit #L3000-001	Invitrogen, Life Technology Corp, CA
Meyer's Hemalaun	Carl Roth GmbH + Co. KG, Karlsruhe, Germany
$MgCl_2 \cdot 6H2O$	Sigma-Aldrich, Saint Louis, MO, USA
Mounting medium for fluorescence microscopy	Ibidi, Martinsried, Germany
$Na_2HPO_4 \cdot 7H2O$	Sigma-Aldrich, Saint Louis, MO, USA
NaCl	Merck, Darmstadt, Germany
$NaH_2PO_4 \cdot H2O$	Sigma-Aldrich, Saint Louis, MO, USA
NaOH	Sigma-Aldrich, Saint Louis, MO, USA
Narcoren®	Merial
OPTI-MEM® #31985-062	Gibco, New York, USA
Paraformaldehyde	Sigma-Aldrich, Saint Louis, MO, USA
Poly-d-lysine #P6407	Sigma-Aldrich, Saint Louis, MO, USA

Puromycin #SC-108071A	Santa Cruz, CA, USA
Rabbit IgG isotype control #31235	Invitrogen, Life Technology Corp, CA
Rompun (2%) & Xylazine	Bayer Vital GmbH, Leverkusen, Germany
Roti® Histol	Carl Roth GmbH + Co. KG, Karlsruhe, Germany
SC144 hydrochloride #SML0763	Sigma-Aldrich, Saint Louis, MO, USA
Sodium Tetraborate decahydrate	Sigma-Aldrich, Saint Louis, MO, USA
Sucrose	Sigma-Aldrich, Saint Louis, MO, USA
Temozolomide #T2577	Sigma-Aldrich, Saint Louis, MO, USA
Tissue-Tek®O.C.T.™ compound	Sakura Finetek USA
Tri-Natriumcitrat- Dihydrate	Roche Diagnostics GmbH, Rotkreuz, Switzerland
Triton X-100	Roche Diagnostics GmbH, Rotkreuz, Switzerland
Tween-20	Sigma-Aldrich, Saint Louis, MO, USA
Vectastain Elite ABC Kit (peroxidase standard) PK-6100	Vector, Burlingame, CA, USA

2.5 Primary antibodies

Table 2.5 Primary antibodies

Primary antibody	**Dilution**	**Company**	**Catalogue number**
Goat anti- IBA1	1:200	Abcam	ab5076
Goat anti- PDGFR-β	1:200	R&D Systems	AF1042
Mouse anti- IDH1-R132H	1:200	Dianova	DIA-H09
Mouse anti human-nuclei	1:200	Millipore	MAB1281
Rabbit anti cleaved caspase3	1:200	Cell signaling	9664
Rabbit anti humanin	1:200	Invitrogen	PA1-41325

Rabbit anti human GAPDH	1:500	Abcloal	AC036
Rabbit anti HUS1	1:200	Invitrogen	PA5-109839
Rat anti-CD31	1:50	Becton Dickinson	550274

2.6 Secondary antibodies and other dyes

Table 2.6 Secondary antibodies and other dyes

Reagents	**Dilution/ Concentration**	**Company**	**Catalogue number**
7-AAD	0.5 μg/1mL	BD Pharmingen	559925
Alexa Fluor 488 donkey anti goat	1:500	Jackson Immuno Research	705-545-147
Alexa Fluor 488 donkey anti rabbit	1:500	Jackson Immuno Research	711-545-152
Alexa Fluor 594 donkey anti rabbit	1:500	Jackson Immuno Research	711-585-152
Alexa Fluor 594 donkey anti rat	1:500	Jackson Immuno Research	712-585-150
Alexa Fluor 647 donkey anti rabbit	1:500	Jackson Immuno Research	711-606-152
Alexa Fluor 647 donkey anti- rat	1:500	Jackson Immuno Research	712-605-153
Cy3 donkey anti goat	1:500	Jackson Immuno Research	705-165-147
Cy5 donkey anti mouse	1:500	Jackson Immuno Research	715-175-150
Dapi 4',6-Diamidin-2-phenylindole (DAPI)	2 μg/mL	Sigma	D9564

SiR-tubulin kit	1 μL/mL	SPIROCHROME	#SC002

2.7 Vectors

Table 2.7 Vectors

Vectors	Company
Histone2B-GFP lentiviral particles	GenTarget Inc
HN_C8A-mutant_pcDNA3.1(+)-P2A-eGFP	Genscript
HN_L9R-mutant_pcDNA3.1(+)-P2A-eGFP	Genscript
HN_WT-ORF_pcDNA3.1(+)-P2A-eGFP	Genscript

2.8 Microscopy

Table 2.8 Microscopy

Microscope	**Company**
Axio Observer A1 inverse fluorescence microscope	Carl Zeiss Microscopy GmbH, Jena, Germany
Axioskop 2 light microscope	Carl Zeiss Microscopy GmbH, Jena, Germany
Axiovert 135 TV fluorescence microscope	Carl Zeiss Microscopy GmbH, Jena, Germany
Axiovert 25 fluorescence microscope	Carl Zeiss Microscopy GmbH, Jena, Germany
BMS D1-223A light microscope	Breukoven b. v., Capelle aan den Ijssel, Netherlands
Inverted Leica DMi8 with Leica DFC9000 GT sCMOS camera	Leica Microsystems Vertrieb GmbH, Wetzlar, Germany
Leica confocal laser microscope SP8	Leica Microsystems Vertrieb GmbH, Wetzlar, Germany

Leica M205 FA stereo microscope with Leica DFC7000 T camera	Leica Microsystems Vertrieb GmbH, Wetzlar, Germany

2.9 Software

Table 2.9 Software

Software	**Company**
AngioTool	National Cancer Institute, Bethesda, Maryland
Axiovision Rel. 4.8/ 4.9 software	Carl Zeiss Microscopy GmbH, Jena, Germany
FCS Express	De Novo Software, CA, USA
GraphPad PRISM 6	Graph Pad Software Inc., La Jolla, CA, USA
Image J	NIH, Bethesda, MD, USA
Leica LAS X Core offline version 1.9	Leica Microsystems Vertrieb GmbH, Wetzlar, Germany
Leica Microsystems LAS SP8	Leica Microsystems Vertrieb GmbH, Wetzlar, Germany
Microsoft Office 2016	Microsoft, Redmond, WA, USA
NoteExpress	Beijing Aegean hailezhi Technology Co., Ltd., Beijing, China

2.10 Human GBM specimens and tumor-free brain tissue

All human specimens were obtained from the tissue bank of Neurosurgical Research Laboratory, University Clinics Munich, LMU. All human GBM were diagnosed by neuropathologists according to WHO criteria.

3. Methods

3.1 *In vitro* experiment

3.1.1 Cell culture

The mouse GBM cell line GL261 was cultured under adherent conditions in Dulbecco's Modified Eagle Medium (DMEM) containing 1× MEM non-essential amino acids, 10% fetal bovine serum (FBS), and 1% penicillin-streptomycin (100 units/mL penicillin and 100μg/mL streptomycin). Human primary, stem-like GBM cell (hGBM) NCH644, NCH684 and GBM20 were cultured in DMEM-F12 medium supplemented with 1× B27, 10 ng/mL human EGF, 10 ng/mL human fibroblast growth factor (FGF), and 1% penicillin-streptomycin. All cells were maintained in a 37°C humidified incubator with 95% O_2 and 5% CO_2. The culture medium was changed once or twice weekly according to the growth rate. GL261 cells were split with trypsin when the cells occupied over 80% of the culture flask. Cells were passaged with accutase when big spheres formed.

3.1.2 Cell transfection and maintenance

Cells were prepared as a single cell suspension and seeded at a density of 500,000 cells/2mL per well in 6-well plates. Transfection was performed using Lipofectamine™ reagent, according to the manufacturer's protocol. The HN-WT plasmid (HN_WT-ORF_pcDNA3.1(+)-P2A-eGFP), HN-L9R plasmid (HN_L9R-mutant_pcDNA3.1(+)-P2A-eGFP) and HN-C8A plasmid (HN_C8A-mutant_pcDNA3.1(+)-P2A-eGFP) were transfected into NCH644 and NCH684 cells. All three plasmids harbored the antibiotic (G418) resistance gene. To select transfected cells, the antibiotic (G418) kill curve was tested for each cell line before transfection. Selection was performed for 2 weeks at a concentration of 400μg/mL for NCH684 and 600μg/mL for NCH644, approximately 2 weeks after transfection. To maintain the culture, half the antibiotic concentration was applied.

3.1.3 Cell-counting experiment

3.1.3.1 Cell-counting experiments of Humanin over-expressing cells

The transfected cell lines NCH644 HN-WT, NCH644 HN-C8A and NCH644 HN-L9R were plated at a density of 100,000 cells (low density) or 1,000,000 cells (high density) in 2 mL growth factor-deprived medium (DMEM-F12 medium without EGF or FGF) in 6-well plates. Each group was prepared in triplicate. For the low-density group, the cells were counted 6 d after plating. For the high-density group, the cells were counted on day 2. Each experiment was independently repeated at least thrice.

Low density groups: High density groups:

Figure 3.1.3.1a: Schedule for cell-counting experiments of Humanin over-expressing cells at different cell densities. Schedule for the low-density seeding group is shown on the left and that of the high-density group is presented on the right. Detailed information is provided in the above section.

Previously, we confirmed that the GP130 inhibitor SC144 can block the protective effect of HN[145]. For the experimental groups with SC144 200 nM treatment, the inhibitor was added on day 0.

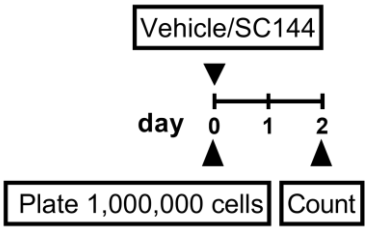

Figure 3.1.3.1b: Schedule for cell-counting experiments of Humanin over-expressing cells at high densities with vehicle/SC144. Cells were seeded and treated with vehicle/200nM SC144 at day 0, and counted at day 2.

3.1.3.2 Cell-counting experiments of conditioned-medium-treated cells

To prepare the conditioned medium, NCH684 HN-WT, NCH684 HN-C8A, and NCH684 HN-L9R cells were seeded in plates at a concentration of 100,000 cells/mL in a growth factor-deprived medium. After 48 h, the cells were centrifuged at 400 G for 5 min, and the supernatant was collected. Conditioned medium was aliquot and kept at -20°C. NCH644 cells (20,000) were plated in 500 μL conditioned medium in a 24-well plate. Three wells were prepared for each treatment group. The conditioned medium was changed every other day. The NCH644 cells were counted on day 7.

For experiments with the inhibitor, vehicle/SC144 (200 nM) was added when the conditioned medium was changed.

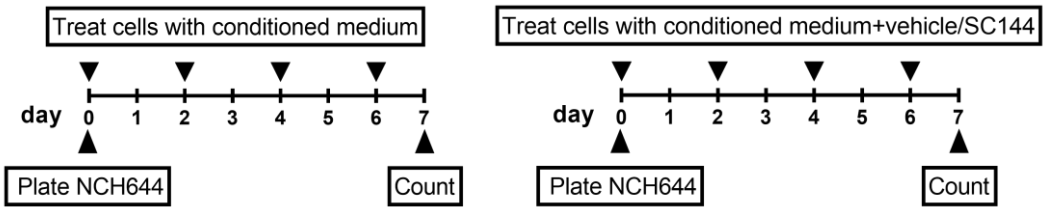

Figure 3.1.3.2: Schedule for cell-counting experiments of conditioned-medium-treated cells with or without SC144. Left timeline shows experiment with conditioned medium only. Right timeline presents cell-counting experiment with conditioned medium and SC144.

3.1.3.3 Cell-counting experiments of bazedoxifene acetate (BZA)

We aimed to further confirm the effect of HN through GP130 using another inhibitor, BZA[108], which is a US Food and Drug Administration (FDA)-approved BBB permeable GP130 inhibitor.

NCH644 cells were seeded at 100,000 cells per well in 2 mL medium on day 0, and vehicle bovine serum albumin (BSA)/HN (200 nM) and vehicle/BZA were added to the cells every other day. Cells were counted on day 7, and 100,000 cells were returned to the culture. Cells were counted again on day 14.

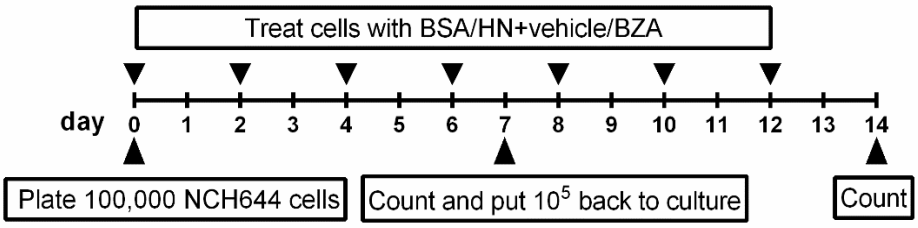

Figure 3.1.3.3: Schedule for cell-counting experiments of BZA. Cells were seeded and treated every other day as shown above. At day 7, cells were counted and only 100,000 were put back to culture. Cells were counted again at day 14.

3.1.3.4 Cell-counting experiments with ATR inhibitor AZ20

To test the involvement of the DNA repair-related ATR pathway in HN downstream effect, ATR inhibitor (ATRi) AZ20 was applied in a cohort of cell-counting experiments in HN-sensitive hGBM to see if it can block the increased proliferation induced by HN peptide treatment (indicated as low density groups in the figure). 100,000 NCH644/NCH684/GBM20 cells in 2 mL medium were plated in 6-well plates on day 0 and treated with BSA/HN and vehicle/ATRi every other day. Cells were counted on day 6. The effect of AZ20 was also verified in HN-overexpressing cell line and HN-mutant cell lines (indicated as high density groups in the figure). AZ20 was applied to the NCH644 HN-WT, NCH644 HN-C8A and NCH644 HN-L9R cell lines at the density of 1,000,000 cells in 2 mL medium. Cells were treated with vehicle/ATRi on day 0, and counted on day 2.

Low density groups:

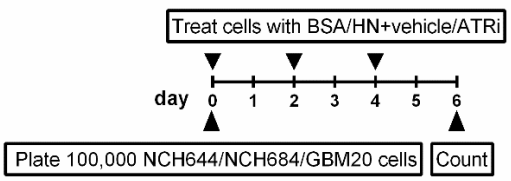

High density groups:

Figure 3.1.3.4: Schedule for cell-counting experiments with ATR inhibitor AZ20. Left timeline shows experiment with low cell density treated with exogenous HN. Right schedule presents experiment with high cell density of HN-WT/mutant transfected hGBM.

3.1.4 Cell preparation for live-time imaging

3.1.4.1 Fluorescence labelling for cells

NCH644 cells were transduced with Histone2B-green fluorescence protein (GFP) using a lentiviral vector. One day before transduction, single-cell suspensions were prepared and seeded in 6-well-plate at a density of 100,000 cells in 2 mL complete medium. For transduction, the lentiviral particles were thawed at room temperature and added to the cells. The cells were returned to the incubator and examined daily. When an adequate number of GFP^+ cells appeared, puromycin (0.5 μg/mL) was added for antibiotic selection, as the lentivirus also carries a puromycin-resistance gene. Visualization of the cellular structure was achieved using Tubulin-SiR dye, which is discussed in the following section.

3.1.4.2 Cell preparation

For time-lapse imaging, an 8-well μ chamber (from ibidi) was coated with poly-D-lysine at a concentration of 50 μg/mL for 30 min, washed with sterilized distilled water, and air-dried for 1 h. NCH644 Histone2B-GFP cells were plated at a density of 500,000 cells in 500 μL of medium in each well. Four groups were included: 1) BSA, 2) BSA+TMZ 100 μM, 3) HN 200 nM, and 4) HN 200 nM+TMZ 100 μM. After confirming that the cells were properly attached to the slides, the medium was replaced with fresh medium with the corresponding reagents and Tubulin-SiR (1 μL/mL). The cells were then incubated at 37°C for 2 h before imaging.

3.1.4.3 Time-lapse imaging

Images were captured using an inverted Leica DMi8 motorized live-cell fluorescence microscope equipped with Leica DFC9000 GT sCMOS camera. The microscope was equipped with chamber to enable regulation of the temperature from ambient to 37°C. CO_2 was added and a “water immersion micro dispenser” allowed long-term observations without the evaporation of immersion water. The HCX PL FL L 40×/0.60 CORR PH2 objective was used, and consecutive images were captured every 3 min. The entire imaging process was conducted for 72 h.

3.1.5 Immunodepletion

HN-conditioned medium was obtained from NCH684 cells overexpressing the HN-WT peptide (medium was conditioned for 2 d). Immunodepletion (or generation of HN-undepleted controls) was performed using an HN antibody (or IgG istotype control) and protein A binding magnetic microbeads (Figure 3.1.5). First, the conditioned medium was incubated on ice for 30 min with HN antibody/IgG isotype control and 10%v/v protein A magnetic beads. The µ-Columns® were set on the MACS® MultiStand and rinsed with 70% ethanol as elution buffer, followed by rinsing with DMEM-F12 medium. Then, the conditioned medium was loaded onto the µ columns. HN was immunocaptured on the magnetic beads and the beads were retained on the column. All flow-through of this column was thereby HN-depleted. NCH644 cells were then cultured at a density of 40,000 cells/mL in 150µL of HN-depleted or control medium in pre-coated 96-well plates for 5 d. Three technical replicates were prepared for each experiment. Subsequently, the cells were fixed with paraformaldehyde (PFA) (4%w/v in 1×phosphate-buffered saline [PBS]). The effect of immunodepletion was evaluated by cell counting. Cells were stained with 4',6-diamidino-2-phenylindole (DAPI) and fluorescent nuclei were counted with fluorescence microscope under a 20× objective. For each plate, five random optical fields were captured and cell number was averaged. Cells samples were also stained for HUS1. Images were captured using a fluorescence microscope with a 40× objective. For each plate, three views were captured and HUS1 intensity was analysed using ImageJ software.

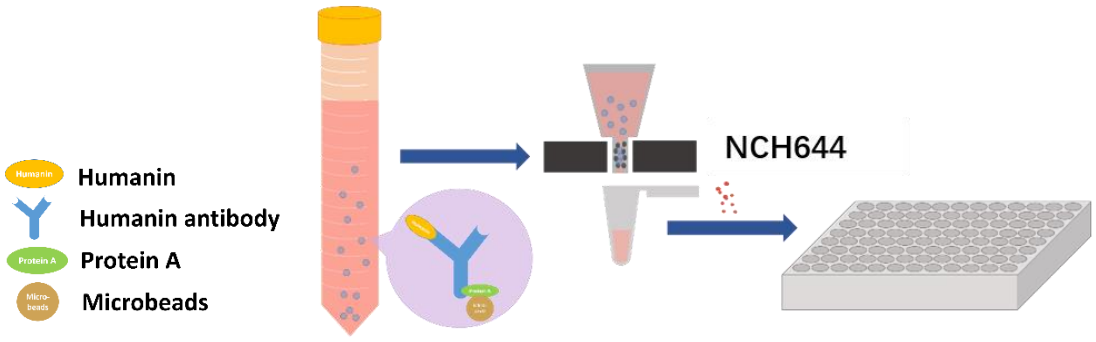

Figure 3.1.5: Schematic workflow of immunodepletion experiments using conditioned medium. Conditioned medium was removed from NCH684 HN-WT. Immunodepletion was

performed using a mixture of HN antibody (versus IgG istotype controls) and protein A-bound magnetic microbeads, then the mixture was loaded onto µ-Columns® set on the MACS® MultiStand. The flow-through medium was used to culture NCH644. NCH644 were plated at the density of 40,000 cells/mL in 150 µL HN-depleted or control medium in pre-coated 96-well plates for 5 d. Three technical replicates were prepared for each experiment.

3.1.6 Cell cycle analysis

NCH644 cells were cultured in growth factor-free medium under the following conditions: 1) BSA, 2) BSA+TMZ 100 µM, 3) HN 200 nM, and 4) HN 200 nM+TMZ 100 µM, with 500,000 cells in 2 mL medium for each condition. Compounds were added every other day and the cells were cultured for 5 d. On day 5, the cells were collected and split into single cell suspension using accutase, followed by three washes with ice-cold PBS. The cells were then fixed with ice-cold 70% ethanol at 4°C for 30 min. After fixation, the cells were centrifuged, and ethanol was discarded, followed by washing three times with PBS. Cells were filtered through a 40 µm strainer before resuspension in PBS. Then, 7-Amino-Actinomycin D (7-AAD) was added to stain nuclei at the concentration of 0.25 µg/500 µL on cell suspension, and incubated for 10 min before analysis. Data acquisition was performed using BD Calibur at a low flow rate. FACS data analysis was performed using FCS Express software.

3.2 *Ex vivo* experiment

Mouse brain culture samples were generously provided by Dr. Charlotte Flüh's group from Max-Delbrück-Center for Molecular Medicine (MDC). Briefly, mouse brains were obtained and sectioned into 200 µm slices for culture using vibratome. The endogenous microglia was depleted using clodronate liposomes[146]. Human microglia-like cells from induced pluripotent stem cells (hiPSC-MG)[147] and/or the hGBM line NCH644 were inoculated into cultured mouse brain slices[145]. Five groups were included in this experiment: 1) naive brain (no hiPSC-MG, no NCH644), 2) NCH644, 3) hiPSC-MG, 4) NCH644+hiPSC-MG, and 5) NCH644+hiPSC-MG+SC144. At the end of the experiment the slices were fixed in 4% PFA for 3 h. Samples were stored in 1× Tris-buffered saline at 4°C until use. Immunofluorescence staining of cultured mouse brain samples was performed as follow. First, the samples

were washed with PBST (PBS+0.1%Tween-20) thrice (5 min for each time), and transferred to primary antibody which was diluted in dilution buffer (5% donkey serum+0.3%Triton-100 in PBS). Samples were incubated at 4℃ for 24 h, and then were washed thrice with 30 min each time. The secondary antibody with the fluorophore was incubated at room temperature for 4 hours, followed by washing (3×30 minutes). Finally, the samples were stained with DAPI for 30 min and washed with PBS for 10 min.

3.3 *In vivo* experiment

3.3.1 Animals

All animal experiments were conducted according to the protocols of the local authorities and the regulations of the National Guidelines for Animal Protection, Germany. All animals were kept in Walter Brendel Centre with sufficient food and water *ad libitum* in standard cages in a cabinet with 12 h light and dark cycle. Mice were examined daily and sacrificed when they were symptomatic or at specific timepoints, depending on the experimental plan.

3.3.2 Tumor inoculation

The mice were anesthetized intraperitoneally (i.p.) with a mixture of 2% Rompun (0.3 mL), 10% ketamine (1.02 mL) and 0.9% NaCl (4.86 mL) at a dosage of 7μL/kg. The mice were then disinfected (on the head) with 7.5% povidone-iodine and eye-protected with Bepanthen® cream, and a midline incision was made on the skin above the skull. After stabilization of the stereotactic frame in the flat-skull position, a puncture was carefully and gently made on the skull with a 21G needle at the coordinate of 1 mm anterior and 2 mm right to the bregma. The needle of a 22G Hamilton syringe was rinsed thoroughly with decreasing concentrations of ethanol (99%, 70%, and 50%), sterilized distilled water, and 1×PBS before taking tumor cells. Tumor cells were prepared at a density of 100,000 cells/μL in culture medium. 1 μL cell suspension was injected into each mouse 3 mm under the skull in 2 min. The needle was slowly

withdrawn at 1 mm/min after injection. The inoculated mice were then sutured and returned to the cages.

3.3.3 Intracerebral drug application

One day before the operation, artificial cerebrospinal fluid (aCSF) was prepared as follows: 1) solution A was prepared by mixing 500 mL sterile water, 8.66 g NaCl, 0.244 g KCl, 0.206 g $CaCl_2 \cdot 2H_2O$, and 0.163 g $MgCl_2 \cdot 6H_2O$; 2) solution B was prepared by dissolving 0.214 g $Na_2HPO_4 \cdot 7H_2O$ and 0.027 g $NaH_2PO_4 \cdot H_2O$ in 500 mL sterile water; 3) solutions A and B was combined in a 1:1 ratio and the solution was filtered through a 0.22 μm filter. Mini-pumps (Alzet mini-osmotic pump model 2004, 0.25 μL per hour, lasts around 28 d) were filled with either 200 μL aCSF or 100 nM HN dissolved in aCSF. All prepared mini-pumps were pre-warmed by immersion in aCSF under 37°C for overnight. After NCH644 inoculation, mini-pumps were directly installed by gently pushing the pump under the skin of the backs of mice and stabilizing the needle into the puncture point.

3.3.4 Administration of BZA

BZA was dissolved in 10%v/v dimethyl sulfoxide (DMSO) and 90%v/v corn oil and i.p. injected at 4 mg/kg or 40 mg/kg in mice[108, 148]. BZA was injected from day 7 after tumor inoculation and was applied five times a week until the end of the experiment. The control group was injected with the vehicle.

3.3.5 Administration of TMZ

TMZ was dissolved in 5%v/v DMSO and 95%v/v saline at a concentration of 5 mg/mL, and was maintained on a shaker until use. Mice were injected i.p. with 50 mg/kg from day 7 after tumor inoculation[149]. The control group was injected with the vehicle. The exact injection schedules are introduced according to each experiment in the results section.

3.4 Histology and immunostaining

3.4.1 Tissue preparation

The mice were anesthetized with Narcoren® and perfused with PBS, followed by 4% PFA solution. Brains and other organs of interest were collected and immersed in 4% PFA at 4°C for 24 h for post-fixation. The organs were then transferred to a hypertonic sucrose solution (30% w/v in 1× PBS). The organs were embedded in Cryomatrix^{TM} and frozen in the vapor phase of liquid nitrogen after equilibrating to the osmotic pressure as the sucrose solution. The brains were cut into 40 μm sections using a microtome and placed in cryoprotective liquid (with 25% glycerol, 25% ethylene glycol and 50% 1×PBS) for later use. The sectioned samples were stored in a 24-well plate and maintained at -20°C in a freezer.

3.4.2 Cell slide preparation for immunofluorescence staining

Round glass (diameter: 12 mm) coverslips were placed in a 24-well plate and covered with 500 μL poly-d-lysine (50 μg/mL) in each well for 1 h at room temperature. After coating, the coverslips were rinsed twice with sterilized water and left to air-dry for 1 h. NCH644 HN-WT, NCH644 HN-C8A and NCH644 HN-L9R were split into single cell and plated at a density of 250,000 cells in 500μL growth factor-deprived medium per well. After 2 d of culture, cells were examined using microscope to determine if they were attached to the coverslip. The coverslips with adherent cells were gently rinsed with PBS and fixed with 4% PFA. The attached cells were then subjected to immunofluorescence staining.

3.4.3 Hematoxylin and eosin (H&E) staining

The samples of interest were mounted on slides and promptly dried. H&E staining was performed in glass wares as follows: 1) the slides were immersed in 100% ethanol for 30 s for dehydration; 2) the sections were then transferred to Mayer's hematoxylin solution for nuclei dye for 2 min; 3) the sections were rinsed with running distilled water for 5 min; 4) then, the sections were moved to 0.5% eosin solution for cytoplasm staining for 30 s; 4) briefly, the slides were rinsed in distilled water and transferred to

increasing concentrations of ethanol for dehydration (1 min in 70%, 96% and 100% ethanol, respectively); 5) then the slides were transferred to Roti®-Histol for 1 min; 6) Entellan® was mounted on each slide before covering the coverslips; and 7) the stained sections were allowed to dry under the hood. Images for H&E staining were captured using Carl Zeiss Axioskop 2 microscope with Axiovision Rel. 4.9 software.

3.4.4 Immunofluorescence staining for mouse brain and cell samples

The brain samples of interest were collected from cryoprotective liquid and placed in washing buffer PBST in a 12-well plate and washed for thrice with 5 min each time. This step was to rinse off the remaining cryoprotective reagent before staining. The samples were then transferred to blocking solution (5% normal donkey serum in 0.3% Triton X-100) for 1 h at room temperature. After blocking, the brain sections were directly transferred to the primary antibody solution and incubated at 4 °C overnight. On the second day, the brain samples were rinsed thrice in washing buffer with 5 min each time before being transferred to a secondary antibody. Incubation was then performed at room temperature for 2 h, followed by a washing step, as described previously. The sections were then mounted on slides and air dried for 15 min. After the nuclear staining with DAPI, the slides were washed by rinsing in distilled water shortly. Finally, the slides were mounted with fluorescence mounting medium and covered with coverslips. As the cell samples were already on the coverslip, the mounting medium was dropped onto the slides, and the round coverslip with cells attached on it was covered on slides with the cell side facing the slide.

3.4.5 Immunofluorescence staining for human GBM samples

Human paraffin-embedded samples were processed with the following steps for deparaffinization and antigen retrieval before staining:

1. The tissue sections were immersed in Histol for 10 min at room temperature for deparaffinization.
2. The samples were immersed in ethanol with decreasing gradients (100%, 96%, 70%, and 50%), each step for 30 s.

3. The samples were fixed in 70% Aceton at -20°C for 10 min.

4. Then, the samples were washed with PBST, thrice with 5 min each time.

5. The samples were then cooked at 100 °C in Citrat Bufffer (1.8 mM Citric acid and 8.2 mM tri-Natriumcitrat-Dihydrat, adjusted to PH 6.0 with 2 mM NaOH) for 20 min.

6. The samples were cooled for 20 min to room temperature.

7. This was followed by washing thrice with PBST, for 5 min each time.

8. The samples were then circled with a hydrophobic Dako Cytomation Pen.

The immunostaining procedure was continued following the steps described previously in section 3.4.4.

3.4.6 Immunohistochemistry for mouse xenograft samples

Paraffin-embedded mouse xenograft samples were first subjected to deparaffinization and antigen retrieval steps, as described in section 3.4.5. Endogenous peroxidase activity was blocked with 3% hydrogen peroxide for 15 min at room temperature. The slides were then rinsed and blocked with 10% donkey serum in PBS for 30 min. the primary antibody was incubated for 1 h at room temperature, followed by 30 min incubation with a biotinylated secondary antibody. Finally, the sections were labelled with avidin-biotin-peroxidase for 30 min. The washing steps (thrice, 5 min each time) were applied between each antibody incubation interval. Signal visualization was achieved by incubation in 3,3'-diaminobenzidine (DAB) solution until the desired stain intensity developed. The samples were rinsed with tap water to prevent further signal development.

3.5 Microscopy

A Zeiss Axioskop-2 light microscope was used to perform imaging for H&E staining and immunohistochemistry. Evaluation of HUS1 fluorescence staining from immunodepletion experiments was performed using an Axio Observer A1 inverse fluorescence microscope. All other fluorescence staining was imaged using Leica confocal laser microscope SP8 confocal. A 20× objective with glycerol immersion was used for most quantifications. A 40× objective with glycerol immersion was used for

higher magnification. All formats were set to 1024×1024 with a scan speed of 200-400 Hz. All channels were imaged separately to avoid crosstalk. The navigator function of the LAS X software package was used when an overview image was required. All images intensity were adjusted according to the respective negative controls. Tile scan was performed for the area that required more information from thicker layer. Confocal images were later processed with LAS X (Leica) for further adjustment and export.

3.6 Quantification

3.6.1 Tumor volume quantification

Mouse brains were cut horizontally for tumor volume quantification. Sections with tumor were collected every 0.4 mm in the dorsoventral axis (Z-axis), mounted, and stained with H&E. Later, the tumor area(A) in each section was measured using Axiovision Rel. 4.9 software. The tumor volume(V) was calculated as $V = (Z_{top} - Z_{bottom}) \times (A_{top} + \cdots + A_{bottom}) \div n$, where Z is the section coordinate relative to the bregma in the atlas and n is the number of sections with tumors.

3.6.2 Quantification of tumor vasculature

The endothelial cell marker CD31[150] and pericyte marker platelet-derived growth factor receptor beta (PDGFRβ)[151] were stained in the mouse samples for quantification (for the staining procedure please see previous chapter). A minimum of three confocal images of the tumor area were captured using a 20× objective for each animal using the same setting between each compared group. For pericyte coverage quantification, images were processed using ImageJ software for further analysis. Images were converted to 8-bit images after being processed into the software. The overlapping area of CD31 and PDGFRβ was extracted using "Process-Image Calculator". The overlapping area and CD31 area were selected for measurement by selecting "Image-Adjust-Threshold". The measurement was preset to "limit to the threshold". Finally, in the read-out, "Area" of the overlap and CD31 were used for the calculation. Pericyte coverage was defined as $PDGFR\beta^{+}CD31^{+}$area/$CD31^{+}$area. The vessel area was quantified using AngioTool software based on CD31 staining.

3.6.3 Quantification of fluorescence intensity

HUS1 staining was performed on slides attached with cells. Three images were obtained with a 40× objective using confocal microscopy for each cell line. Subsequently, the images were imported into ImageJ software for intensity quantification. Images were first converted to an 8-bit format, then the stained area was selected in "Image-Adjust-Threshold". The mean intensity value was obtained by selecting "Analyze-Measure".

3.7 Microarray

Human GBM samples and controls (patients with lateral sclerosis) were collected and split into single cell suspension. The samples were stained with CD11b and CD45 and sorted using flowcytometry. $CD45^{+}CD11b^{+}$ cells were collected from patients with GBM and controls. 10,000 cells were collected from each sample and stored at -80 ℃. For microarray hybridization, mRNA was isolated from samples and converted into cDNA; the cDNA was labeled with biotin. Later, the labeled and fragmented single strand cDNA was spiked with cDNA hybridization controls, which served as an internal control for sensitivity and accuracy of the hybridization reaction as well as the wash and staining procedure. The spiked cDNA samples were hybridized at 45°C for 16.5 h on separate Affymetrix GeneChip® HuGene ST 2.0 Arrays. After hybridization, microarrays were stained in two binding cycles using anti-biotin antibodies and a streptavidin-phycoerythrin conjugate. Subsequently, the microarrays were washed with increasing stringency and conserved in holding buffer using the Affymetrix GeneChip® 3000 Fluidics Station in combination with the Affymetrix GeneChip® Command Console (AGCC) - Fluidics Control Software v4.0.0. Fluorescent signal intensities were detected with the Affymetrix GeneChip® 3000 Scanner and AGCC Scan Control Software v4.0.0 (Affymetrix). Automatic grid was arranged and raw data were processed to generate image and intensity files by the AGCC software. The software tools AGCC Viewer v4.0.0 and Expression Console v1.4.1.46 (both Affymetrix) were used for visualization of the performance of microarray analysis.

3.8 RNA sequencing

NCH644, NCH684, and GBM20 were used for RNA sequencing. The same number of cells for each cell line was plated under both the control and HN 200 nM conditions. After 72 h, cells were counted and cell pallets were gained, resuspended in 100 µL Trizol, and stored at -80 °C. Samples were sent to single cell discoveries for bulk RNA sequencing. For the analysis, the obtained data were first filtered to remove genes with no or nearly no expression of the indicated gene dataset across all samples. The resulting dataset contained 16329 genes. The data were then normalized and transformed using regularized log transformation, which normalizes the data with respect to library size and transforms the count data to the log2 scale in a manner that minimizes the differences between samples for genes with small counts. The normalized dataset was later used to assess sample similarities and to calculate the fold changes between samples of interest. For the comparisons without sample replicates, the fold difference for each gene was calculated in a pair-wise fashion. The normalized log-transformed data were used to calculate pairwise differences. Single-sample Gene Set Enrichment Analysis (ssGSEA) was applied to analyze cell cycle related genes, which were extracted from the molecular signature database under ontology gene sets (MSigDB, http://www.broadinstitute.org/gsea/msigdb) using the ssGSEA method of the R software Gene Set Variation Analysis (GSVA) package.

3.9 Statistic analysis

All statistical analyses were performed using GraphPad Prism 6 software. The unpaired Student’s t-test was used to determine the difference between two independent groups. Welch’s t-test was used for the comparison with heterogenous variance between two groups. For groups greater than two, one-way analysis of variance (ANOVA) followed by Tukey's or Sidak's multiple comparisons test was used. The log-rank (Mantel-Cox) test was used to determine survival differences. Statistical significance was set at $P < 0.05$.

4. Results

4.1 MT-RNR2 is upregulated in TAM

Many previous studies about TAMs focused on the nuclear encoded transcriptome and only to a smaller number of researches on the non-coding mRNA levels. The current RNAseq bioinformatic methods may exclude information on mitochondrially encoded genes as they rely on parameters for data quality control. Therefore, as an alternative strategy to explore non-coding or mitochondrial RNA (MT-RNA) plus mRNA in TAM we performed bulk transcriptomics with microarrays without filtering out MT-RNA. To this end we purified TAMs from GBM biopsies or microglia from tumor-free human brains (from hippocampal sclerosis patients) by FACS according to established protocols using CD11b and CD45 as myeloid cell markers (Figure 4.1A, B). Gene ontology analysis of differentially expressed genes between TAM and tumor-free microglia revealed a strong enrichment of mitochondrial metabolic pathways in TAM (Figure 4.1B). Among the top five genes in TAM we observed the mitochondrially encoded 16S rRNA (MT-RNR2), which contains a small ORF for the peptide HN (Figure 4.1C). We assumed that HN is an interesting target to explore the impact of mitochondrially encoded gene on GBM development.

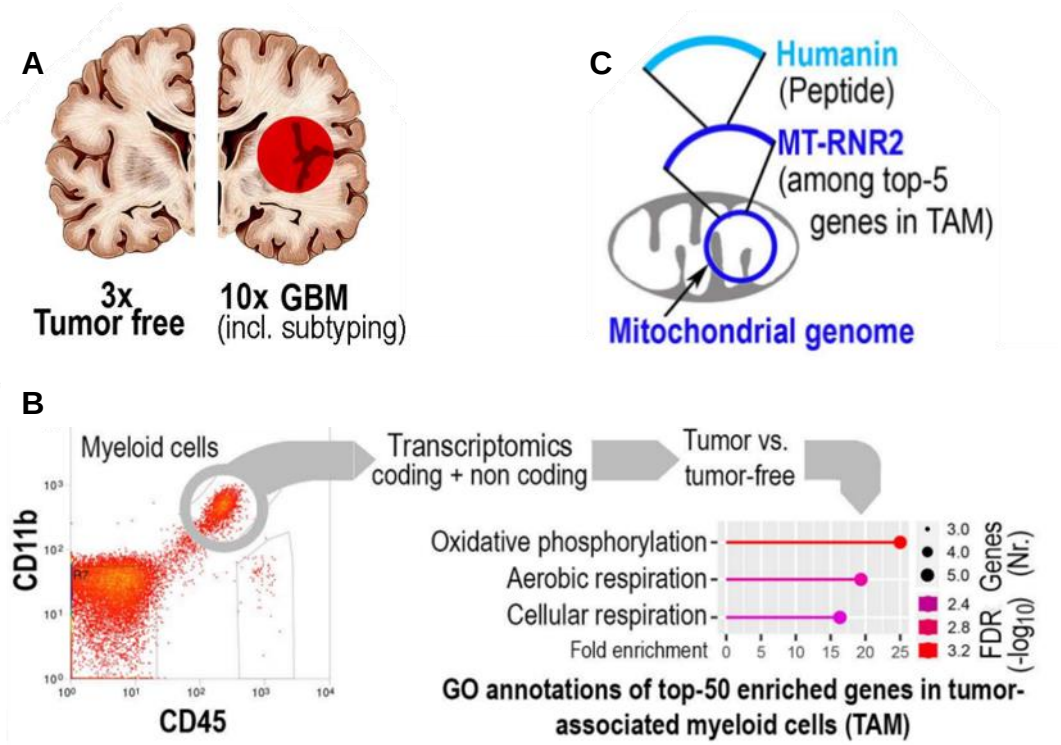

Figure 4.1: MT-RNR2 is upregulated in TAM. (A-B) Myeloid cells purified (using CD11b and CD45 as markers) from biopsies of hippocampal sclerosis (tumor free) or GBM, underwent transcriptomic profiling and bioinformatic analysis, which showed an enrichment for gene expression pattern associated with aerobic metabolic pathways in TAM as compared to controls. **(C)** The mitochondrial ribosomal RNA encoding gene MT-RNR2 is among the top-5 upregulated genes in TAM. MT-RNR2 contains an ORF for the peptide HN.

4.2 Humanin is preponderant in TAMs and partly expressed in GBM cells

Since a specific antibody for HN is available, we investigated if the MT-RNR2 gene would be translated into HN, which should then be detectable in TAM. Indeed, we found, by confocal inspection of human GBM samples (immunofluorescently labeled for HN and the myeloid cell marker IBA1) that HN was strongly expressed in TAM (Figure 4.2). Therefore, MT-RNR2 (or MT-RNR2 encoded HN) is preponderant in TAM as compared to microglia associated with neurodegeneration.

In addition, the immunofluorescence experiments indicated that HN was not exclusively expressed TAM, but also in other intra-tumoral cells (Figure 4.2). In order to test the presence of HN in brain tumor cells we immunostained isocitrate

dehydrogenase (IDH) mutant astrocytoma with an antibody for the detection of the IDH1-R132H variant and found HN in IDH-mutant cells[152].

All in all, a set of independent methods consistently showed that expression of HN is much stronger in GBM than in tumor free specimen.

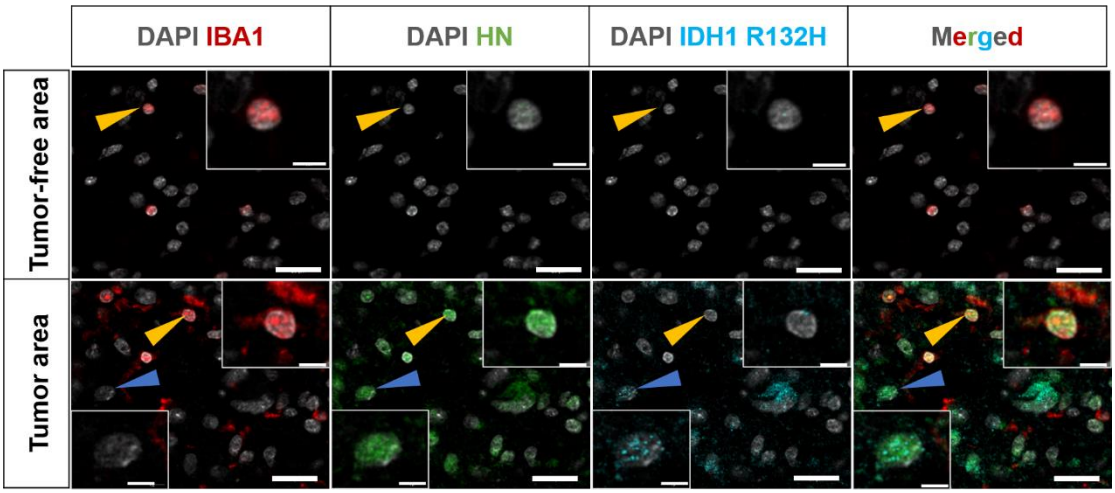

Figure 4.2: Humanin is highly expressed in TAMs in human GBM. Confocal pictures of immunofluorescence staining of HN in the tumor area (lower row) compared with the tumor-free area (upper row). IBA1, HN, IDH1 R132H, and DAPI staining was performed. $IBA1^+$ TAM or microglia are indicated with **yellow** arrows, and IDH1 $R132H^+$ tumor cells are shown with **blue** arrows. The cells with arrows are also shown in magnified pictures. Scale bar (in unmagnified pictures) =20 µm, scale bar (in magnified pictures) =5 µm.

4.3 Nanomolar Humanin concentrations drive tumor cell expansion and chemoresistance to TMZ

Transcriptomics of human GBM TAMs indicated upregulation of the mitochondrial ribosomal subunit MT-RNR2 which contains an ORF for the human-specific signaling peptide HN (Figure 4.1). Immunohistochemistry revealed that HN was preponderant in TAMs and partly expressed in GBM cells (Figure 4.2). Therefore, it is important to determine whether HN exerts any physiological/pathological role in GBM. To address this question, we previously conducted a HN-sensitivity experiment using patient-derived hGBM in which we identified HN-sensitive hGBM (NCH644 and GBM20) that increased expansion and accelerated chemoresistance when applying nanomolar concentration of HN. Furthermore, we identified HN-insensitive hGBM (Line2, Line10,

and Line11) that only reacted to micromolar concentration of HN treatment[145]. Among the HN-sensitive hGBM, NCH644 was the most sensitive cell line that responded to HN at concentration as low as 20 nM. In the present study, we identified another HN-sensitive hGBM, NCH684. Cells cultures were growth factor deprived and partly the chemotherapeutic TMZ, with or without addition of HN/HNG (a mutant HN variant with increased potency) [82], were administrated to the NCH684. We found that, HN/HNG treatment did not significantly enhance the proliferation of NCH684 cells. However, when TMZ was added, at 100 µM or 300 µM, HN/HNG treatment augmented resistance to TMZ (Figure 4.3).

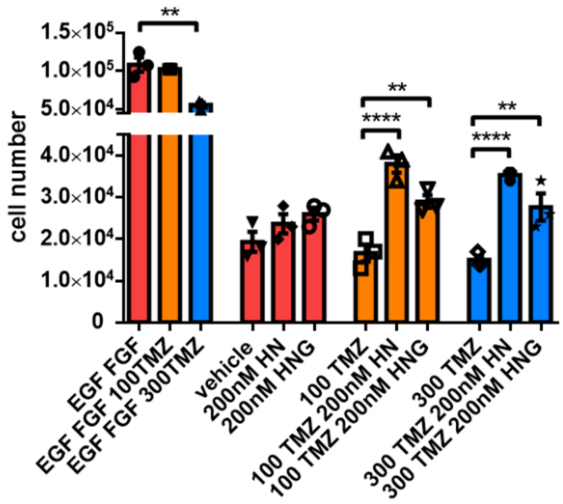

Figure 4.3: Nanomolar concentrations of Humanin or HNG exhibit cytoprotective effects on patient-derived hGBM NCH684, and induce chemoresistance to TMZ. Cells were treated with HN/HNG, TMZ or the vehicle in medium with (indicated by "EGF FGF" in group name)/without growth factor every other day. Cell numbers were counted on day 7. The same-color columns illustrate the same TMZ concentrations. Symbols in the graph represent technical replicates. Values are presented as mean ± standard error of the mean (SEM). One-way ANOVA followed by Sidak's multiple comparisons test was used to determine statistical significance. $^{**}P \leq 0.01$, $^{****}P \leq 0.0001$.

4.4 A secreted Humanin isoform is required to promote tumor cell expansion

Exogenous HN peptide can boost the proliferation of HN-sensitive hGBM within a certain HN concentration range[145], suggesting that HN modulates cell viability through intracellular or extracellular pathways. To investigate if intra- or extracellular signaling predominates HN-induced protumorigenic effects, we generated GBM cells

(NCH644) stably expressing wild type HN peptide (HN-WT; potentially mediating intra- and extra-cellular effects) or GBM cells expressing HN mutants that cannot be secreted (HN-L9R; these retain intracellular biological activity) or have no function at all (HN-C8A)[153]. Cell numbers of these genetically manipulated GBM were quantified in our assay (Figure 4.4). In the first cohort of experiments, cells were seeded at the density of 50,000/ml. At the experimental endpoint, no difference in proliferation between the groups was observed (Figure 4.4A). We wondered if this was due to the low HN concentration at this low seeding density. To address this question, we conducted another experiment with higher seeding density (500,000/ml). At the experimental endpoint HN-WT cells had grown to much higher cell numbers as compared to GBM expressing HN mutants (Figure 4.4B), the intracellularly active HN-L9R promoted viability only very moderately (as compared to the inactive HN-C8A controls). Altogether, these results indicates that: 1) in HN-overexpressing cell lines, the HN effect is cell density-dependent, indicating an HN concentration-dependent effect on NCH644 proliferation; and 2) HN has a strong protumorigenic effect in secreted form.

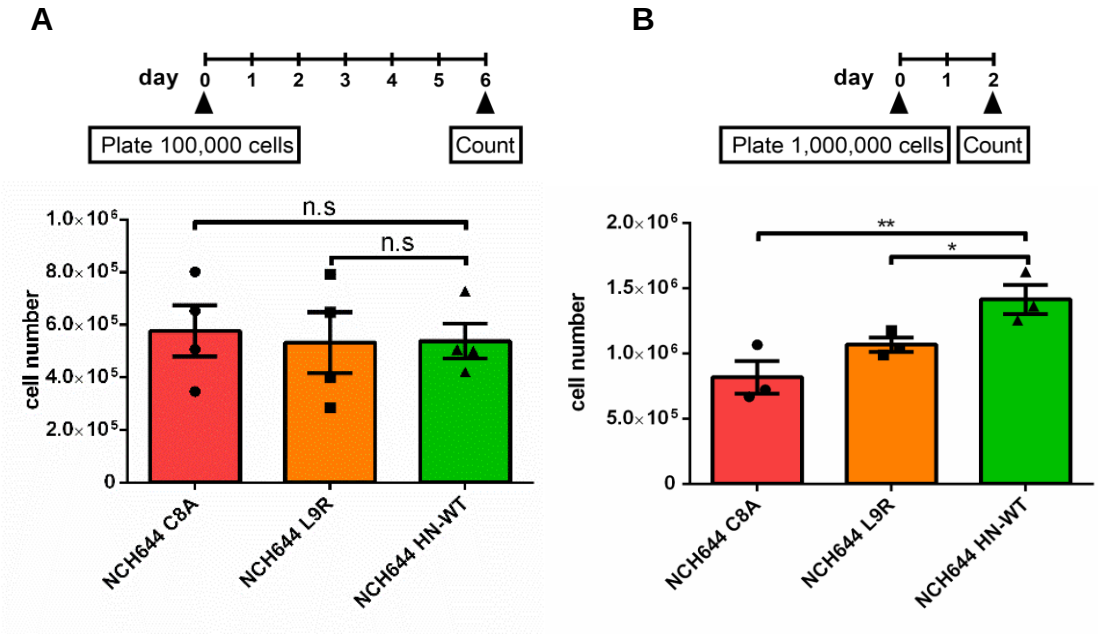

Figure 4.4: hGBM (NCH644) overexpressing a Humanin-WT peptide expand faster than NCH644 cells expressing an inactive (Humanin-C8A) or non-secreted (Humanin-L9R)

isoform. (A) Cells were plated in a 6-well plate at a low density of 100,000 cells/well (in 2 mL medium without growth factor) and were counted 6 d after plating. **(B)** Cells were plated in a 6-well plate at a high density of 1,000,000 cells/well (in 2 mL medium without growth factor) and were counted 2 d after plating. Each experiment was averaged from three technical replicates and results from these individual experiments are indicated with symbols. Values are presented as mean ± SEM. One-way ANOVA followed by Tukey's multiple comparisons test was used to determine statistical significance. *$P \leq 0.05$, **$P \leq 0.01$, n.s: not significant.

4.5 Humanin-release promotes GBM expansion

To further explore a physiological/pathological role of HN released from hGBM transfected to overexpress the HN-WT peptide, two experiments were performed. First, we used the conditioned medium from NCH684 HN-WT, NCH684 HN-C8A (function-nullified mutant) and NCH684 HN-L9R (non-secreted mutant) to culture HN-sensitive hGBM NCH644 (Figure 4.5A). Cell numbers were counted in each condition 7 d after seeding. The result showed that conditioned medium from NCH684 HN-WT significantly increased the proliferation of NCH644 compared with the conditioned medium from NCH684 HN-C8A and NCH684 HN-L9R (Figure 4.5B). In the second experiment, we generated conditioned medium from NCH684 HN-WT cells, that was later either incubated with beads combined with IgG isotype control or with HN specific antibody (depleted), beads (and immuno-captured molecules) were retained in the column and the flow-through HN containing or depleted medium was used to culture GBM cells (Figure 4.5C). By quantifying hGBM cell numbers we observed that the HN-WT induced tumor promoting effect was fully abrogated by HN immunodepletion but was preserved in controls (Figure 4.5D). Collectively, these results demonstrated the secretion of HN and its pro-tumorigenic effect on HN-sensitive hGBM.

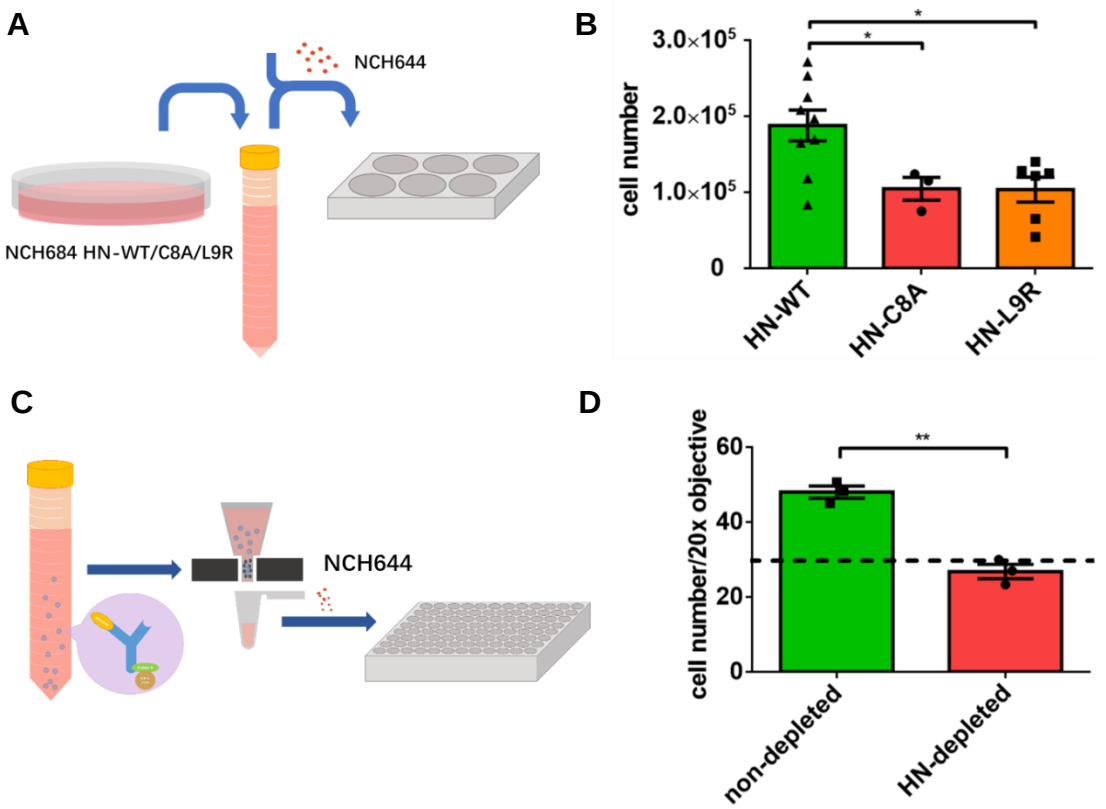

Figure 4.5: Secreted Humanin boosts GBM expansion. (A) Workflow for the NCH644 proliferation experiment using conditioned medium. Medium was collected 48 h after plating and used to culture NCH644. NCH644 was plated in the conditioned medium at the density of 20,000 cells/500µL in 24-well-plate. Cell proliferation was evaluated on day 7. **(B)** Comparison of NCH644 cell number after 7 d of culture with conditioned medium from NCH684 HN-WT, NCH684 HN-C8A and NCH684 HN-L9R. **(C)** Schematic overview of immunodepletion experiment. NCH644 was plated at a density of 40,000 cells/mL in 150 µL HN-depleted/non-depleted (using HN antibody/IgG isotype control with protein A binding magnetic microbeads) conditioned medium from NCH684 HN-WT in pre-coated 96-well-plate. Cells were counted on day 5 after fixation and DAPI staining and visualized using fluorescence microscopy with 20× objective. For each plate, five views were counted and cell numbers were averaged. **(D)** NCH644 cell numbers on non-depleted and HN-depleted conditions. Dotted line indicates the baseline cell number with control medium without adding beads or flowing through column. For each independent experiment, three technical replicates were prepared. Each independent experiment is represented by one symbolic dot in the graph. Values are presented as mean ± SEM. The t test was used to compare significant difference between two groups; one-way ANOVA followed by Tukey's multiple comparisons test was used to determine statistical significance between three groups. *$P \leq 0.05$, **$P \leq 0.01$.

4.6 Humanin activation of GP130 receptor promotes hGBM expansion

4.6.1 GP130 inhibitor SC144 blocks tumor promoting effect of Humanin

Our experiments showed that extracellularly applied synthetic HN peptide or recombinant HN in secreted form promoted hGBM expansion. Previously Several membrane receptors for HN have been reported, such as the trimeric interleukin receptor (CNTFR/ WSX-1/ IL6ST) and formyl peptide receptors (FPRL1/FPR2)[104, 109]. To further investigate the receptor for HN in hGBM, we quantified the mRNA expression levels of these receptor subunits in both HN sensitive and insensitive hGBM by qPCR (Figure S4.6.1a). We detected the subunits of the trimeric interleukin receptor in all hGBM, but formyl peptide receptors were undetectable.

In order to further verify HN signaling through CNTFR/ WSX-1/ IL6ST receptor in hGBM, we first focused on IL6ST (GP130) subunit, which activates several second messenger after HN or IL6 binding[154, 155]. We used SC144 in HN-sensitive NCH644 cultured in conditioned medium from NCH684 HN-WT and two mutant lines. Results revealed that 200nM SC144 (versus control) fully blocked the growth promoting effect of HN from HN-WT conditioned medium (Figure 4.6a A). SC144 concentration was tested (Figure S4.6.1b) in advance to avoid toxicity by high concentration. In the second experiment, we used SC144 in GBM expressing HN-WT, HN-L9R or HN-C8A. As expected, HN-WT tumor cells (controls without SC144) out-proliferated all other experimental groups, which was fully blocked by the application of 200 nM SC144 (Figure 4.6a B).

4.6.2 GP130 inhibitor BZA blocks tumor promoting effect of Humanin

BZA is a GP130 inhibitor approved by the FDA that has also been reported to efficiently penetrate the BBB[108, 148]. Before using this inhibitor in our *in vivo* experiments, we tested this inhibitor *in vitro.* First, the working concentration of BZA was tested, we chose a concentration of BZA that did not affect tumor cell expansion (when BZA was applied alone). NCH644 cells were plated at 100,000 cells per well in 2 mL medium without growth factor and treated with vehicle/HN 50 nM plus 150 nM

BZA every other day (NCH644 reacted to HN from 10 nM to 200 nM[145]). Cells were counted on day 14. Cells treated with 50nM HN exhibited significantly higher cell numbers than control group. By adding 150 nM BZA, the growth promoting effect of HN was fully blocked (Figure 4.6a C).

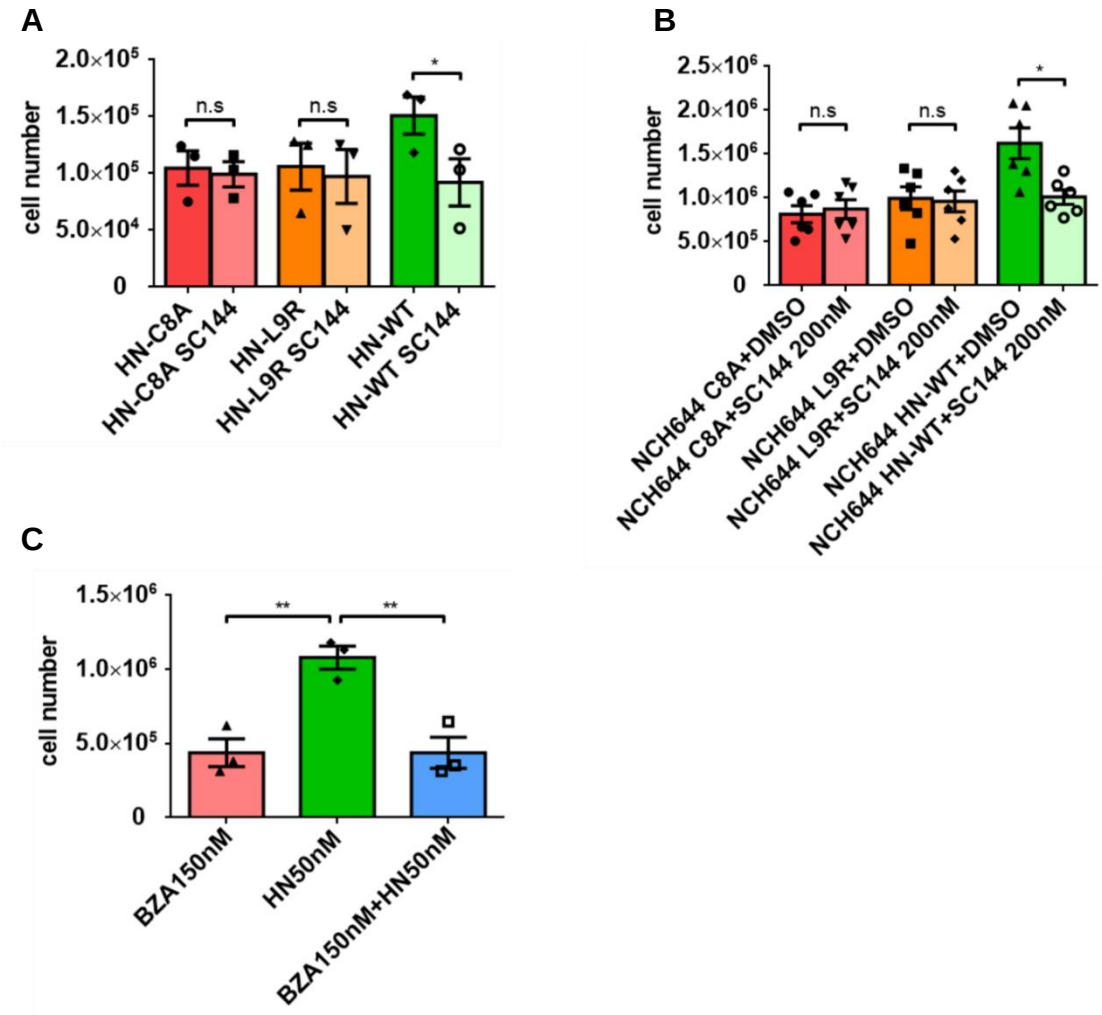

Figure 4.6a: Humanin activation of the GP130 receptor subunit promotes hGBM expansion. **(A)** NCH644 cultured with GP130 inhibitor SC144 and conditioned medium from NCH684 HN-WT, NCH684 HN-C8A, and NC684 HN-L9R. Cells were counted on day 7 and cell numbers were compared between each condition. **(B)** NCH644 overexpressing HN-WT or HN-mutant peptides were seeded in triplicate at density of 1,000,000 cells/well in 2 mL medium with/without SC144 treatment in growth factor-deprived medium and counted on day 2. **(C)** The FDA-approved BBB-permeable GP130 inhibitor BZA was tested on NCH644 to verify its effect on HN. Cells were plated at the density of 100,000 cells/well in 2 mL non-growth factor medium and cultured for 14 d. On day 7, cells were split and counted; only 100,000 cells were returned to the culture. HN, BZA, or the vehicle were added every other day. Cells were counted again on day 14. For each independent experiment, three technical replicates were prepared. Each independent experiment is represented by one symbolic dot in the graph. Values are presented as mean ± SEM. One-way ANOVA followed

by Sidak's multiple comparisons test was used to determine statistical significance in different groups in (A) and (B); one-way ANOVA followed by Tukey's multiple comparisons test was used in (C). *$P \leq 0.05$, **$P \leq 0.01$, n.s: not significant.

4.6.3 The GP130(IL6ST)/MAPK(ERK) signaling pathway is activated by Humanin

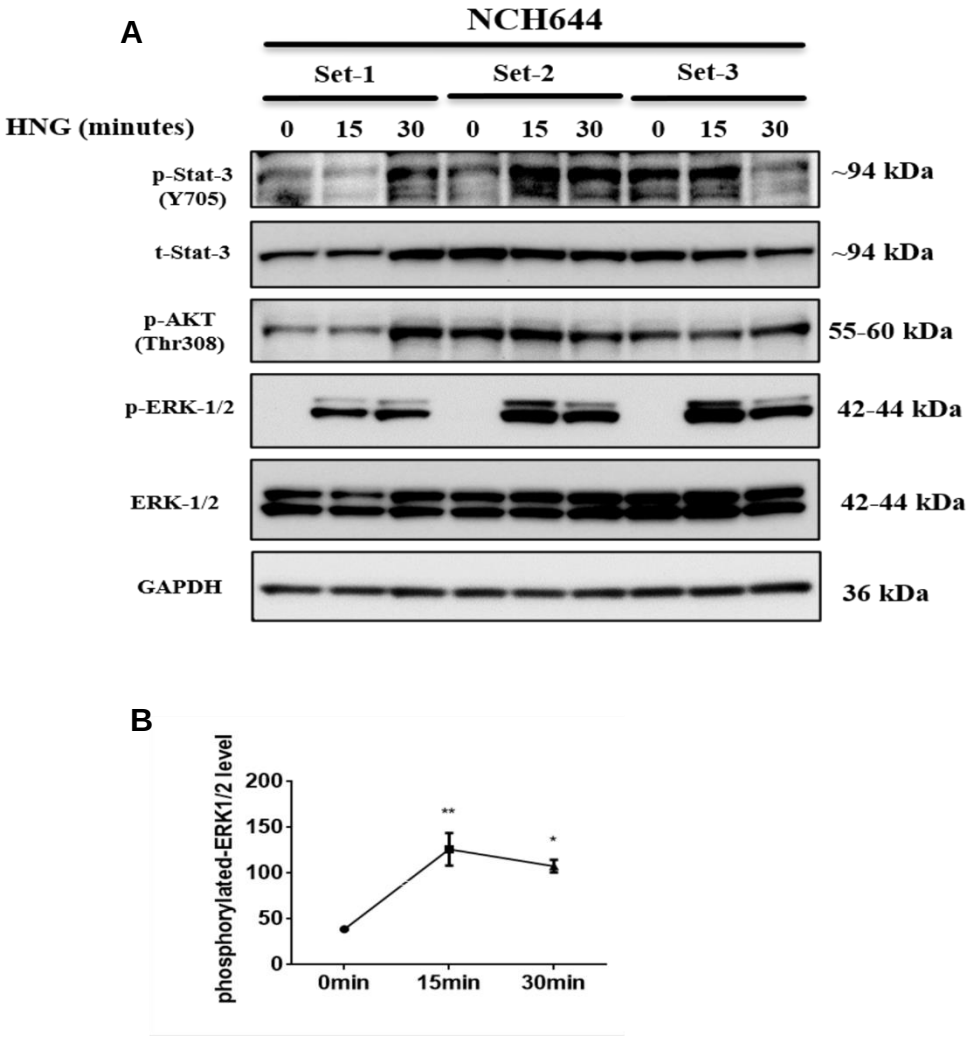

Figure 4.6b: ERK1/2 plays a role in Humanin signaling. (A) Fifteen minutes after 20 nM HNG treatment phosphorylated ERK1/2 expression increased compared with that at 0 min. STAT3 (phosphorylation on Y705) and AKT (phosphorylation on Thr308) was already active under control conditions (0 min.) and not further activated by HNG. **(B)** Western Blot results show that phosphorylated-ERK1/2 level was significantly higher after 15 min and 30 min compared with that at 0 min. Three independent experiments are indicated as Set 1-3 in the graph. Values are presented as mean ± SEM. One-way ANOVA followed by Tukey's multiple comparisons test was used to determine statistical significance at three time points. *P≤0.05, **P≤0.01. kDa= 1,000 Daltons.

The GP130 receptor subunit plays an important role in transducing signal in physiology and pathology including GBM[155, 156]. Activation of STAT3 related pathway by

IL6-binding to GP130 was an essential mechanism in inducing irradiation resistance in GBM[157]. Therefore, we expected that HN would also activate STAT3[154, 158]. But surprisingly, from Western Blotting experiments we observed a rapid activation of MAPK (ERK1/2) after 20 nM HNG treatment on hGBM, whereas STAT3 or AKT activity was not altered (Figure 4.6b). This result indicated HN-triggered signaling through GP130 in GBM may differ from the canonical mechanism that induce irradiation resistance. Furthermore, we investigated why phosphorylated-STAT3 (p-STAT3) level in HN-sensitive hGBM NCH644 was already high before HNG application. We found that HN-sensitive GBM express much higher CD109 than HN-insensitive GBM (data not shown). Previous study showed that CD109 dimerizes with GP130 and thereby stimulates p-STAT3[159], which may explain the high baseline level of p-STAT3. This point is being investigated by our lab currently.

In addition, as the canonical ERK signaling pathway is often related to receptor tyrosine kinases[160], we also had a look at the activation of these receptors by immuno-blotting assay to see if there is any involvement of other receptors for HN. However, no differences were observed (HN 100nM 25min vs control) in a tyrosine kinases-receptor activation immuno-array or in an EGF-receptor activation immuno-array (Figure S4.6.3).

4.7 RNAseq indicates that Humanin promotes expression of the DNA-clamp component HUS1

HN prompted tumor expansion by inducing resistance towards the chemotherapeutic TMZ. To explore how this process was controlled mechanistically we conducted a series of RNAseq studies with HN sensitive hGBM. First, we identified differentially expressed genes in HN stimulated NCH644 versus vehicle-treated controls and found that HN affected various signaling pathways (Figure 4.7a A). When repeating the experiment with other HN-sensitive hGBM lines (GBM20 and NCH684) and screening out the consistantly expressed genes (in NCH644, GBM20 and NCH684) we revealed molecular networks related to: the ATR controlled DNA damage pathway,

neurodegeneration and apoptosis (Figure 4.7a B). From the network we focused on HUS1, an ATR-dependent DNA repair related gene. This gene has pathological relevance in GBM. Survival analysis based on TCGA and the Genotype-Tissue Expression (GTEx) database showed that HUS1 expression levels correlate with GBM patient survival. Higher HUS1 expression was associated with shorter survival (Figure 4.7a C). Interestingly, GP130 (IL6ST) was highly transcribed after HN treatment in the HN-sensitive hGBM (Figure S4.7). In the experiments presented in the previous sections of this study, we showed evidence to support that a GP130 inhibitor can block tumor promoting effect of HN, indicating GP130 as a HN-activated receptor. Here, we also observed the upregulation of GP130 after HN treatment, which highlights an additional aspect of the HN signal transduction, suggesting a positive feedback between HN and GP130.

HUS1 is a crucial component of the 9-1-1 (RAD9A-RAD1-HUS1) complex, a circular clamp that can sense the DNA damage and is loaded onto the impaired site under chemotherapy stress and genome instability[161, 162]. Proper function of the 9-1-1 complex is critical for recruiting repair factors and scaffolding the ATR signaling pathway for DNA repair[163]. Activation of the ATR pathway is commonly observed in GBM[164], particularly after chemotherapy. However, the role of HUS1 in GBM remains unclear. Therefore, in the present study, we focused on this gene and studied its relationship with HN in GBM. In addition, several ATR inhibitors have already entered clinical trials as treatments for GBM[165, 166]. These results illustrate the importance of the HUS1-related ATR DNA repair pathway, in which HN is also involved.

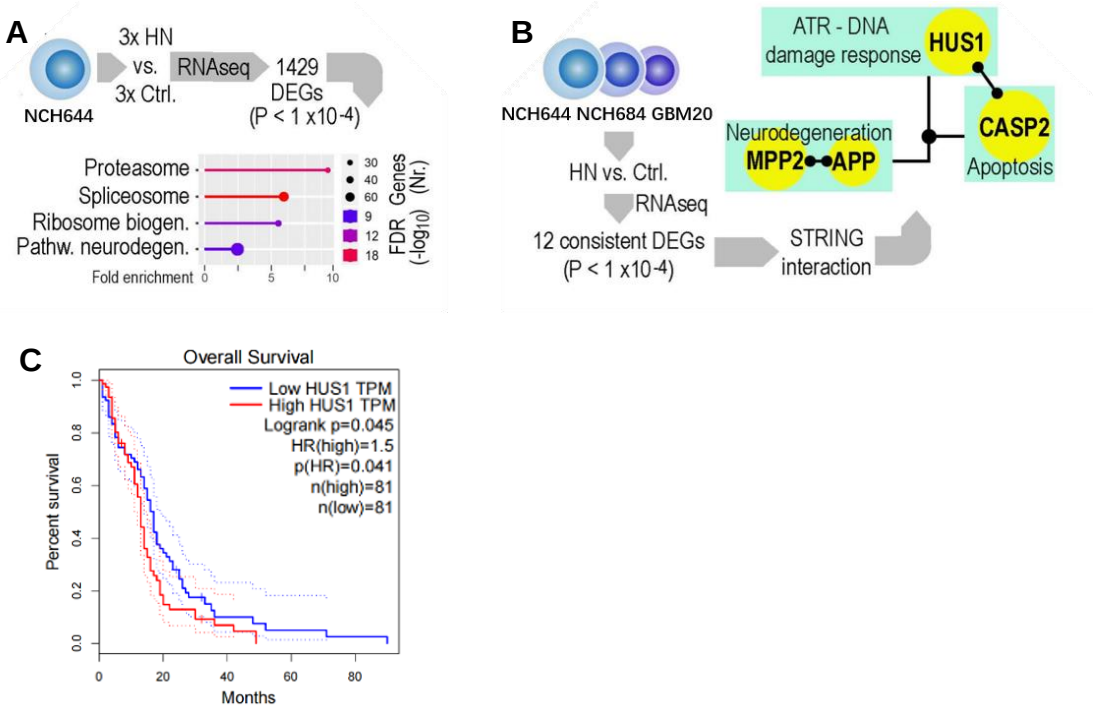

Figure 4.7a: Humanin promotes transcription of the DNA-clamp component HUS1. (A) NCH644 cells were stimulated with HN or vehicle (Ctrl.) underwent transcriptomics and differentially expressed genes were analyzed by bioinformatics. **(B)** Experiments described in (A) were repeated with NCH684 and GBM20, providing 12 consistent differentially regulated genes, of which several components assembled in a network. **(C)** Survival of patients with GBM with high and low HUS1 transcription. Plot was generated using GEPIA with data from TCGA and the Genotype-Tissue Expression (GTEx).

To verify HUS1 upregulation after HN treatment, as indicated by RNAseq, we first performed HUS1 immunostaining on cell samples of NCH644 overexpressing HN-WT, HN-C8A or HN-L9R. Immuno-intensity for HUS1 was compared between the three lines. Representative images from confocal microscopy are shown in Figure 4.7b A. The over-/under-exposure maps, in which blue and black indicate high- and low-intensity areas, illustrate the intensity differences. Fluorescence intensity analysis with the ImageJ software showed a significantly higher intensity of HUS1 in NCH644 HN-WT than in the two mutant lines (Figure 4.7b C). This suggests that HN can increase HUS1 expression. This result also implies HUS1 elevation relies on a secreted HN with exogenous function, rather than endogenous signaling. Second, we analyzed HUS1 expression by immunofluorescence staining of the sample from the immunodepletion experiment, as described in Figure 4.5C. Expression of HUS1 was augmented by

conditioned medium from HN-secreting cells (isotype control), but not after immunodepletion of HN from conditioned medium (Figure 4.7b B and D).

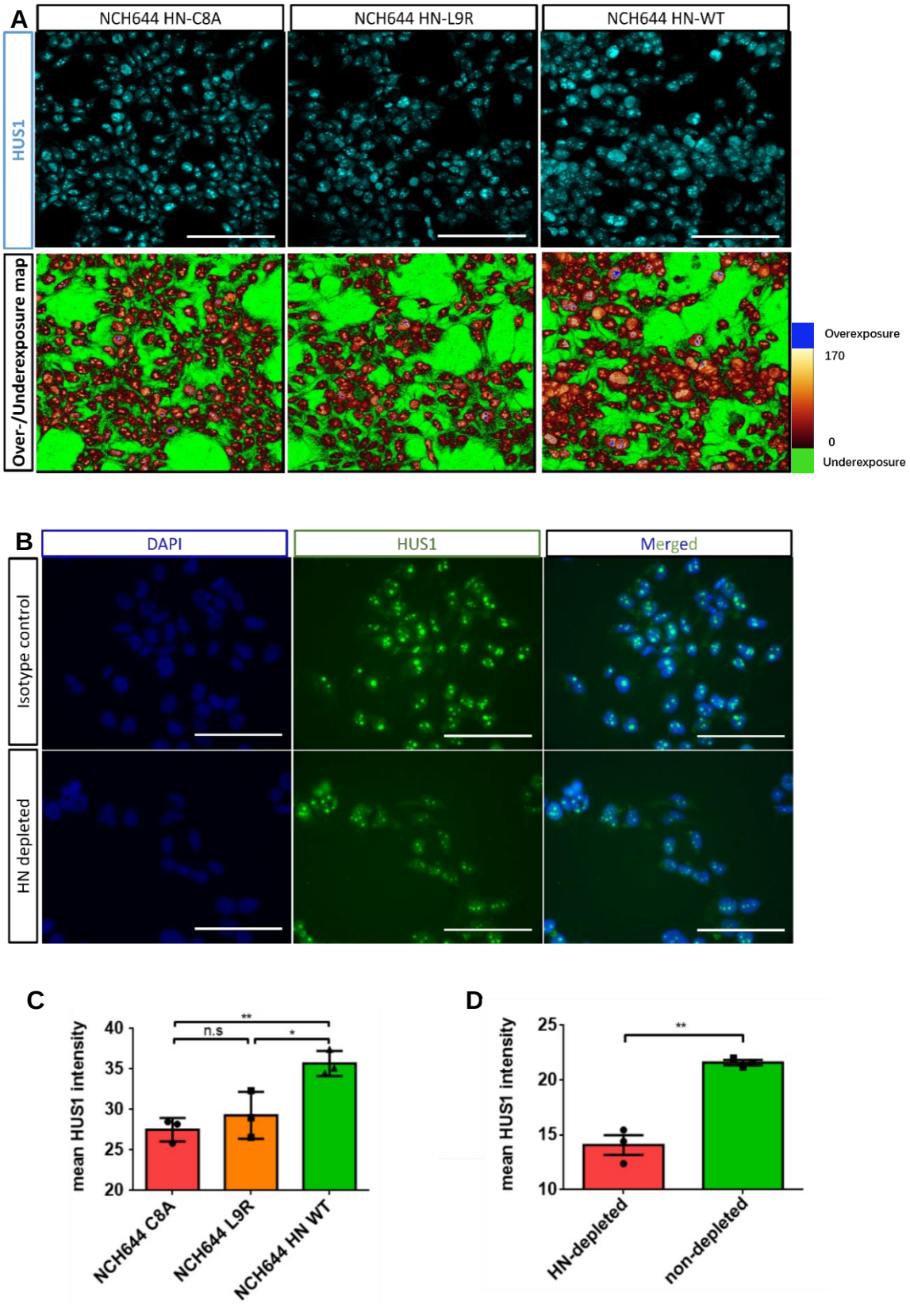

Figure 4.7b: Humanin promotes expression of the DNA-clamp component HUS1. (A) Three transfected cell lines were plated with high density on pre-coated slides (1,000,000 cells/2 mL in non-growth factor medium). Cells were fixed and stained with HUS1 2 d after culture. The upper row indicates HUS1 signal and the lower row shows the over-/underexposure map to better present the intensity; bright blue and orange areas show high intensities, darker color shows low intensities. **(B)** NCH644 was plated at a density of 40,000 cells/mL in 150 µL HN-depleted/non-depleted (using HN antibody/IgG isotype control with protein A binding magnetic microbeads) conditioned medium from NCH684 HN-WT in a pre-coated 96-well-plate. Cells were fixed on day 5 and stained with HUS1. Pictures were captured using a fluorescence microscope with 40× objective. **(C)** Quantification for the HUS1 intensity was performed using ImageJ. **(D)** For each well in the immunodepletion experiment, three views were imaged and the intensities were averaged. In each independent experiment, three technical replicates were prepared. Each independent experiment is represented by one symbolic dot in the graph. Values are presented as mean ± SEM. One-way ANOVA followed by Tukey's multiple comparisons test was used to determine significant differences in three groups, t test was used to compare statistic difference between two groups. **P*≤0.05, ***P*≤0.01, n.s=not significant. Scale bar=200 µm (A), Scale bar=100 µm (B).

4.8 Humanin promotes the ATR-dependent DNA-repair machinery

To further investigate the role of the HN-stimulated (HUS1-related) ATR-dependent DNA repair pathway, we used the ATR inhibitor AZ20[167] to determine whether it can block the cytoprotective effect of HN under growth factor deprivation and during chemotherapy. First, AZ20 concentration was tested (Figure S4.8), we chose a concentration that did not alter the tumor growth when applied alone. Then, NCH644 overexpressing HN-WT and two other mutant cell lines were treated with AZ20 (versus control). The experiment revealed that AZ20 can counteract the HN induced growth promoting effect in NCH644 HN-WT hGBM (Figure 4.8A). Next, we tested if AZ20 can also block HN-induced chemoresistance in NCH644, NCH684 and GBM20 cells. As shown in the Figure 4.8B-D, 0.1 µM AZ20 alone did not alter the expansion of these hGBM lines, while it counteracted the cytoprotective effect by 100 nM (200nM for GBM20 and NCH684) HN under condition with or without 100µM TMZ, thus indicated that HN induced chemoresistance was ATR-dependent. Furthermore, HN (200 nM) also mediated GBM20 (Figure 4.8C) and NCH684 (Figure 4.8D) protective effect in the presence of high concentration of TMZ, which was blocked by AZ20.

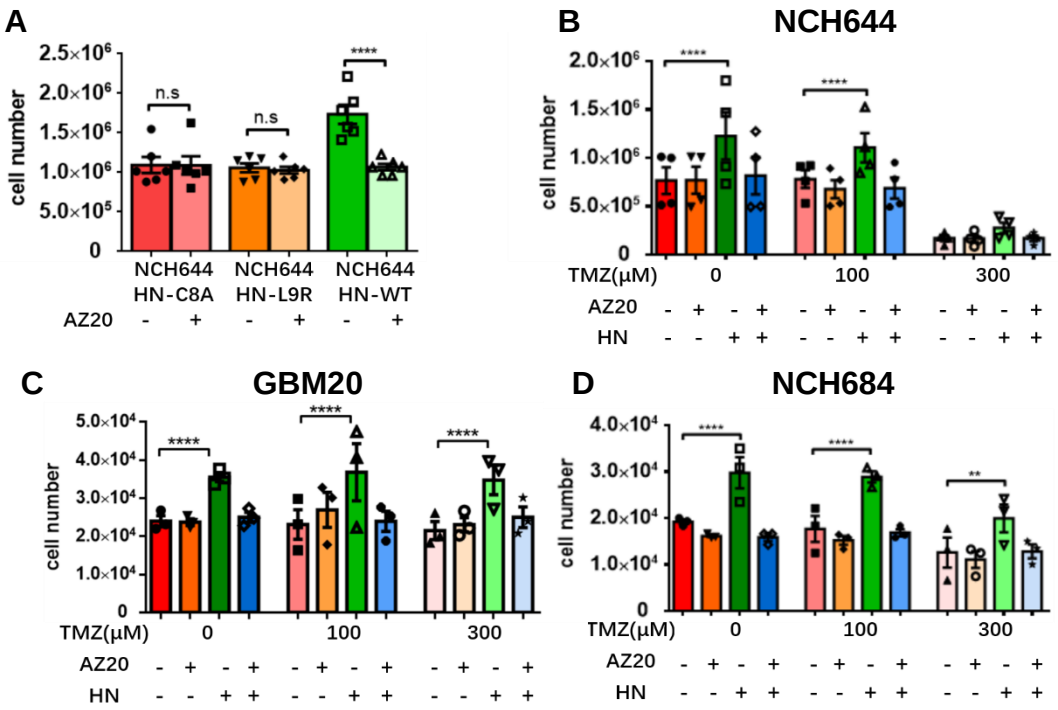

Figure 4.8: ATR inhibitor blocks the Humanin promoted chemoresistance. (A) NCH644 HN-WT, NCH644 HN-C8A, and NCH644 HN-L9R were plated at a high density of 1,000,000 cells in 2 mL non-growth factor medium and treated with vehicle/0.1 μM ATRi AZ20. Cells were counted on day 2. **(B-D)** NCH644, GBM20 and NCH684 were plated at 100,000 cells/2 mL in non-growth factor medium and treated with HN (100 nM HN for NCH644, and 200nM HN for GBM20 and NCH684). TMZ at concentrations of 100 μM or 300 μM, and 0.1 μM AZ20 were applied every other day. Cells were counted on day 6. Three technical replicates were prepared in each independent experiment, and every individual experiment is represented by a symbolic dot in the graph. Values are illustrated as mean ± SEM. One-way ANOVA followed by Tukey's multiple comparisons test was used to determine significant differences between groups. ***P*≤0.01, *****P*≤0.0001, n.s=not significant.

4.9 Effect of Humanin on the cell cycle

4.9.1 Cell cycle analysis reveals rescue effects of Humanin under TMZ treatment

We found that the DNA repair-related HUS1/ATR signaling is upregulated in HN-treated HN-sensitive hGBM; this prompted us to further investigate whether HN alters the cell cycle[168]. First, based on our NCH644 bulk RNAseq data (HN-treated vs. control), we conducted Single-sample Gene Set Enrichment Analysis (ssGSEA) to evaluate the separate enrichment scores for samples according to a cell cycle-related gene set[169, 170]. Each ssGSEA enrichment score indicates the extent to which the genes in a particular gene set are coordinately up- or down-regulated within a sample.

We observed a higher cell cycle related gene set enrichment score in HN-treated NCH644 cells than in the vehicle-treated control cells (Figure 4.9.1A). In addition, we performed cell cycle analysis using flow cytometry. NCH644 cells was treated under different conditions for 5 d as described here: 1) BSA, DMSO, 2) BSA, TMZ 100 µM, 3) HN 200 nM, DMSO, and 4) HN 200 nM, TMZ 100 µM (Figure 4.9.1 B). HN-treated cells showed a significant decrease in the apoptotic subG1 peak under chemotherapy using TMZ compared with the condition without HN, indicating that HN rescued GBM cells from TMZ-triggered apoptosis. We did not observe significant changes in other phases of cell cycle through this analysis (Figure 4.9.1 C and D).

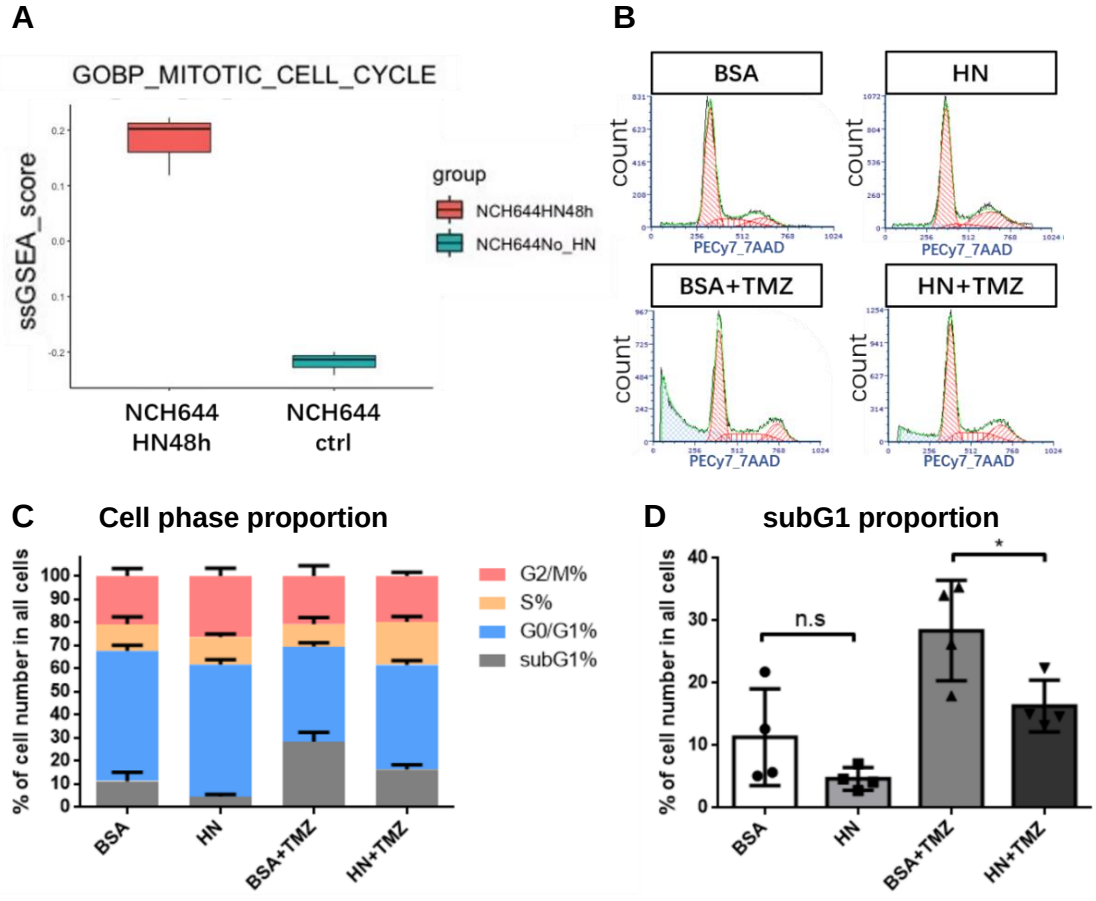

Figure 4.9.1: Humanin reduces apoptosis caused by TMZ. (A) ssGSEA shows up-regulation of cell cycle-related genes in the HN treated sample (NCH644 with 48 h HN treatment) compared with control (with three technical replicates for each group). **(B)** Cell cycle analysis of NCH644 cells treated in different condition with HN, TMZ, or vehicle. Cells were cultured for 5 d and the corresponding compounds were added every other day. Cells were then harvested and digested into single cells. Fixation was performed using 70% ice-cold ethanol for 30 min. Cells were washed with PBS and resuspended with PBS. 7-AAD was added to the cells at the concentration 0.25 µg/500 µL for the nuclei staining. Samples were run at low speed. Cell cycle analysis was achieved using FCS

express software. Debris and duplets were excluded by gating. Histograms are shown with the fitted curve for the subG1, G0/G1, S, and G2/M phases. **(C)** Different portions of cell phase in each experimental group. **(D)** Statistical analysis of subG1% in all cells between different conditions. Every individual experiment is represented by a symbolic dot in the graph. Values are illustrated as mean ± SEM. One-way ANOVA followed by Tukey's multiple comparisons test was used to determine significant difference between groups. *$P \leq 0.05$, n.s=not significant.

4.9.2 Live imaging indicates altered mitosis and cell fate induced by Humanin

Due to the high heterogeneity of tumor cell division[171, 172], we examined the cell cycle more profoundly by live imaging. We used NCH644 cells transduced with Histone2B-GFP[173, 174] and tubulin stained with Tubulin-SiR[175]. Cells were cultured under the following conditions: 1) BSA, 2) BSA+TMZ 100 μM, 3) HN 200 nM, and 4) HN 200 nM +TMZ 100 μM, all in medium without growth factors. All the conditions were imaged in parallel for 3 d with 3 min intervals under a 40× objective and each view contained at least 50 cells.

Time-lapse images were analyzed for cell mitosis in each single cell. In the 3-day imaging slot, most of the cells (>70%) in each condition underwent mitosis. During imaging, we observed many abnormal mitoses. When non-transformed cells go through mitosis, typically two centrosomes are formed and are located at the two poles of the cell, on which the microtubules attach[176]. As mitosis progresses, the microtubules attach to the duplicated DNA that aligns at the equator of the cells, and each spindle of the tubule drags one copy of the chromosome to one end of the cell, until all chromosomes are separated. Errors occurring at any step during mitosis can cause abnormal division and therefore lead to an unbalanced distribution of chromosomes[177]. During imaging, we captured some normal mitoses as just described (Figure 4.9.2a A and B). However, a large number of mitoses was found to be abnormal. This was expected under the very challenging, growth factor deprived, culture conditions[178]. Multipolar mitosis was frequently observed (Figure 4.9.2a D), and is common in tumor cell proliferations[179]. In some cases, remodeling of multiple microtubule organizing centers (MTOC)[180] occurred and deteriorated cell division, leading to formation of multi-micronucleated structures (Figure 4.9.2a E)[181, 182].

We also observed some cells without nuclei that died after a short period of time (Figure 4.9.2b D). Another interesting finding was that closely opposed cells were more likely to divide synchronically; sometimes cells fused and underwent mitosis.

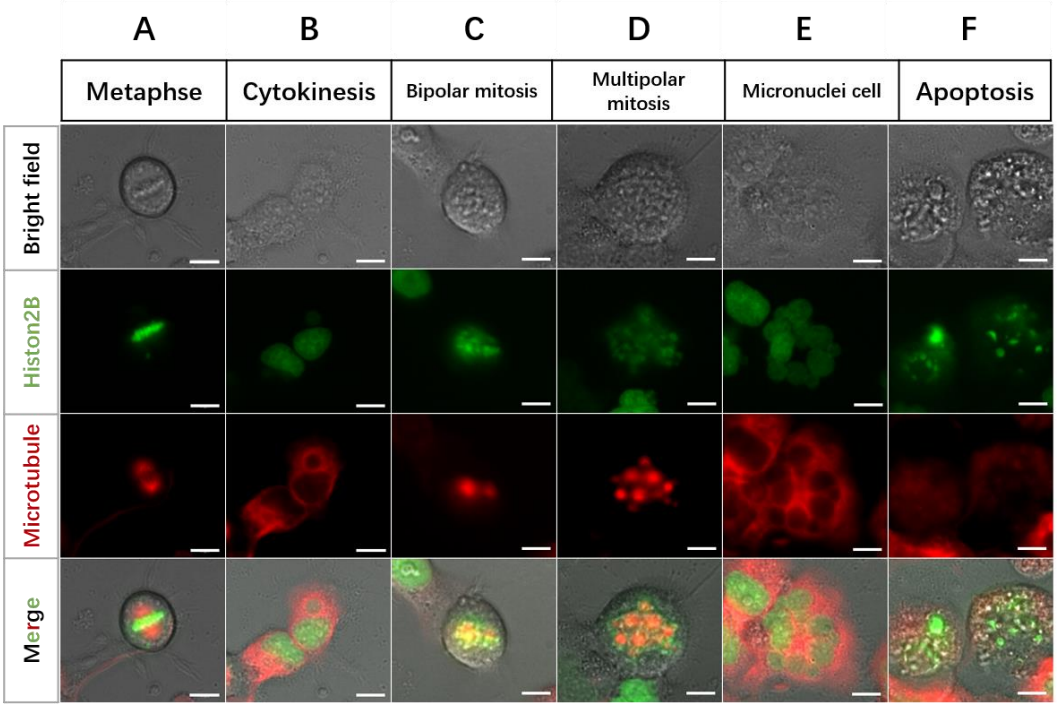

Figure 4.9.2a: Live imaging shows abnormal mitosis and apoptosis of hGBM. Live imaging for NCH644 cultured with HN, TMZ or vehicle. Transduction of Histone2B-GFP (**green**) and Tubulin-SiR **(red**) dye was applied for the visualization of cell structure and chromosome. Cells were plated at the density of 500,000 cells/500 uL in each chamber in pre-coated ibidi 8 well µ slides and imaged using a Leica upright fluorescence microscope in the dark incubator with temperature, humidity, and CO_2 maintenance. **(A)** Metaphase in normal mitosis. **(B)** Normal cytokinesis of the diving cell shown in A. **(C)** Abnormal metaphase without metaphase plate in the middle of the cell; the MTOCs are inequal in size. **(D)** Abnormal mitosis with multiple MTOCs. **(E)** Cytokinesis after metaphase such as in C or D; nuclei are not separated and micronuclei formed instead. **(F)** Apoptosis. Scale bar=10 µm.

To explore the effect of HN on mitosis, the behavior of each cell under each condition was recorded over time. The time-lapse cell profiles are illustrated in Figure 4.9.2b A. Each line in the graph refers to one cell, and different colors represent the cell status. In the HN and HN+TMZ groups, compared with the BSA or BSA+TMZ groups, fewer cells died without going through mitosis, and a higher percentage of all the cells underwent mitosis, although the differences were not statistically significant (Figure S4.9.2 A). The frequency of multipolar mitosis tended to increase with chemotherapeutic stress under HN treatment compared to non-HN control (Figure

S4.9.2 B). We also examined the percentage of the cells that underwent a second mitosis. In the BSA control group (BSA is vehicle for HN), approximately 60% of the cells that completed the first mitosis underwent the second mitosis. This percentage decreased significantly when TMZ was applied. Interestingly, when treated with HN+TMZ, the percentage did not change significantly as compared to the group that received HN treatment alone (Figure 4.9.2b B). Besides, as mentioned previously, we observed some cells without nuclei (without Histone2B-GFP) that died a short period after mitosis. An example of this is shown in Figure 4.9.2b D. This phenomenon was notably more apparent in the non-HN-treated groups (Figure 4.9.2b C).

A

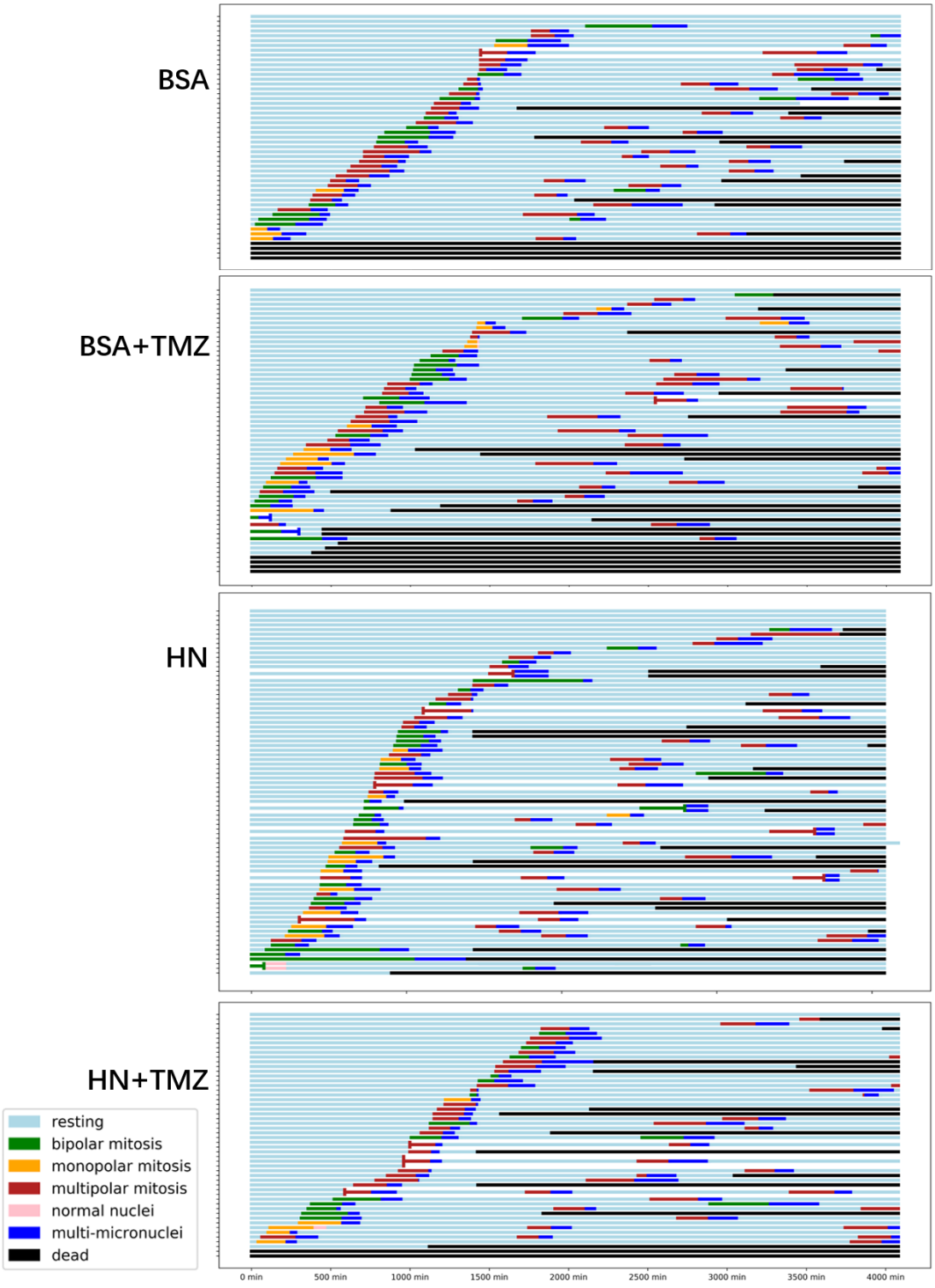
BSA
BSA+TMZ
HN
HN+TMZ
resting
bipolar mitosis
monopolar mitosis
multipolar mitosis
normal nuclei
multi-micronuclei
dead
0 min
500 min
1000 min
1500 min
2000 min
2500 min
3000 min
3500 min
4000 min

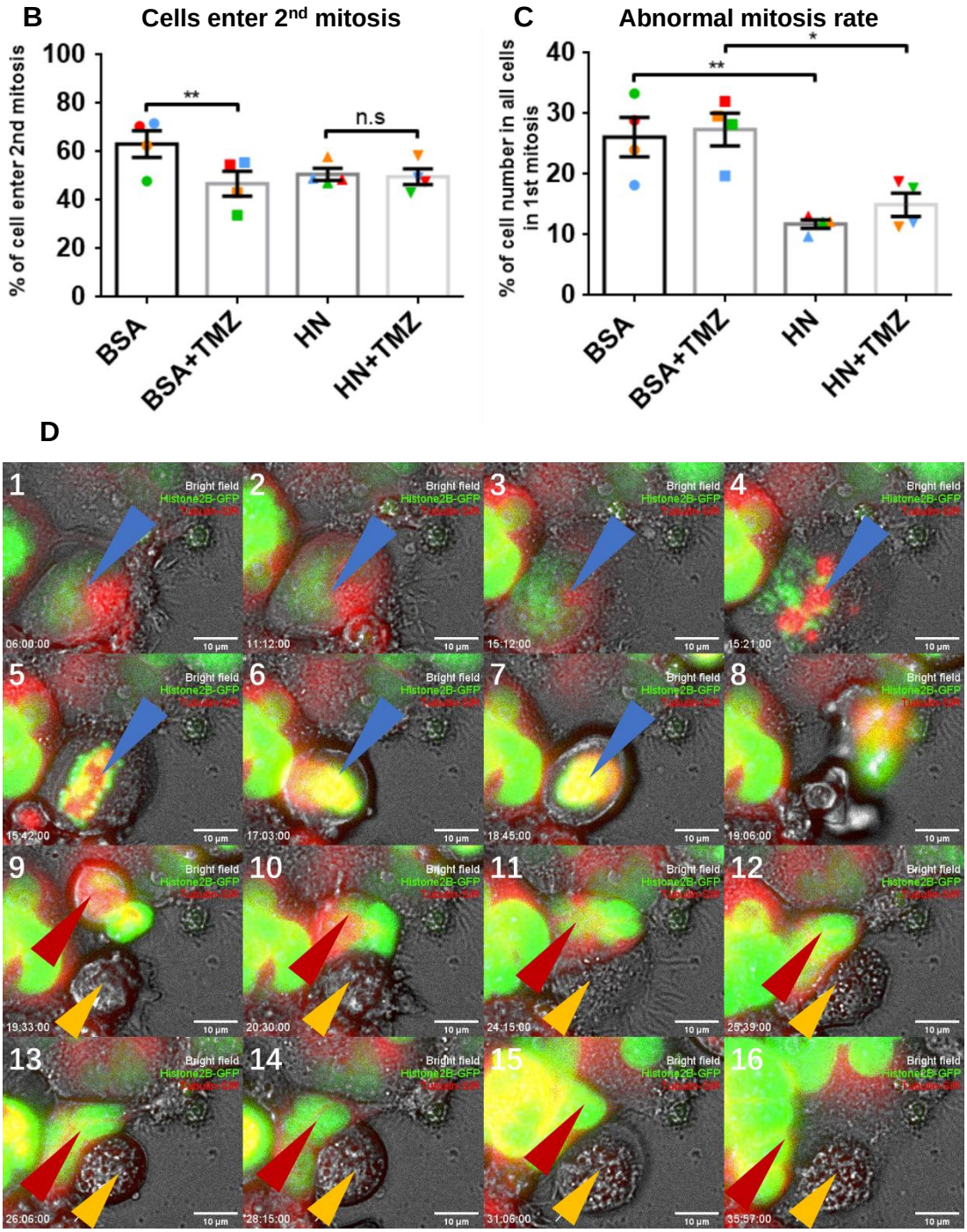

Figure 4.9.2b: Cell profile in live imaging. (A) Cell status was recorded over time and illustrated in the graph. Every line represents one cell and the x axis refers to time (approximately 3 days). Different colors on lines indicate normal or abnormal mitotic phases (notification for each color is presented in on the left side at the bottom). **(B)** Result for the comparison between groups on cells that underwent the second mitosis after the first mitosis. **(C)** Result for the comparison between groups on cells that formed a daughter cell-like "shell" without Histone2B-GFP in the first mitosis. **(D)** Example for mitosis that made non-nuclei daughter cells, where parent cell is indicated by **blue** arrow and two daughter cells pointed by **red** (indicates a daughter cell with Histone2B-GFP and Tubulin-SiR) and **yellow** (indicates a daughter cell without Histone2B-GFP or Tubulin-SiR) arrows. Four independent experiments were conducted. Each symbolic dot represents a percentage from a

single experiment, and same-color dots indicate values from the same experiment. Values are illustrated as mean ± SEM. One-way ANOVA followed by Sidak's multiple comparisons test was used to determine statistical significance between groups. *$P \leq 0.05$, **$P \leq 0.01$, n.s=not significant.

4.10 HiPSC-MG induced Humanin-mediated increase of HUS1 expression *ex vivo*

Since human TAM and GBM cells had remarkably high HN levels compared with tumor free microglia, we asked if this was a consequence of the interaction of these two cell types. HN expression in the tumor-free mouse brain and in murine glioma cell line is notably low (Figure S4.10 A)[78]. So in order to address our question, we modeled the tumor environment by coculturing human myeloid cells and hGBM on mouse brain preparation *ex vivo*. For human myeloid cells, we used human microglia-like cells induced from pluripotent stem cells (iPSC-MG)[183]. For human GBM, we used HN-sensitive NCH644 (Figure 4.10 A). In mouse brain slices endogenous microglia was depleted with clodronate liposomes[146] and the depletion efficiency was confirmed by IBA1 staining (Figure S4.10 B). After inoculation in clodronate liposome treated mouse brain slices preparations, human iPSC-MG (GFP^+) and NCH644 were identified with either human-specific GAPDH staining or human nuclei staining (Figure S4.10 C and D). In general, five groups were designed: 1) naive brain (no hiPSC-MG, no NCH644); 2) NCH644; 3) hiPSC-MG; 4) NCH644+hiPSC-MG; and 5) NCH644+hiPSC-MG+SC144 200 nM. In all five groups, endogenous microglia was depleted. After harvesting all cultivated samples, HN expression was inspected by immunostaing and ImageJ analysis. Notably, high levels of HN were only observed when hiPSC-MG and GBM cells were co-implanted (Figure 4.10 B). This suggests that strong HN expression is induced in GBM and TAM upon mutual interaction and does not result from contact with other brain parenchymal cells. The induced high level of HN was completely inverted by co-administration of GP130 inhibitor SC144. Using this organotypic brain slice model, we also investigated if HN stimulated HUS1 expression was induced by TAM and GBM interaction (and modulated by GP130). Samples from different groups were stained with HUS1 and the fluorescence intensity

was analyzed using ImageJ software (Figure 4.10 B and C). Higher expression was observed in NCH644+hiPSC-MG than in NCH644 alone, indicating that HN-sensitive GBM cells had increased HUS1 expression upon contact with microglia. The GP130 inhibitor SC144 can block this effect as HUS1 expression decreased in group 5, in which SC144 was added to NCH644 and hiPSC-MG coculture. We also noticed that HUS1 expression in the naive mouse brain and hiPSC-MG was significantly lower than that in tumor cells (Figure 4.10 B and C).

In summary, *ex vivo* experiment shows that the strong intra-tumoral HN and HUS1 expression observed in GBM depends on TAM and GBM interaction via GP130. On one hand, this new finding provided important insight into the signaling cues of extracellular HN in GBM: TAM/GBM interaction (upregulating intra-tumoral HN) initiates HUS1 (a marker for HN signaling) in downstream of GP130. On the other hand, this dataset pointed towards a mechanism for HN initiated chemoresistance: HN induced elevated HUS1 expression which is an essential component of the DNA repair RAD9A-RAD1-HUS1 (9-1-1) complex that can mediate therapy failure in cancer including GBM[184].

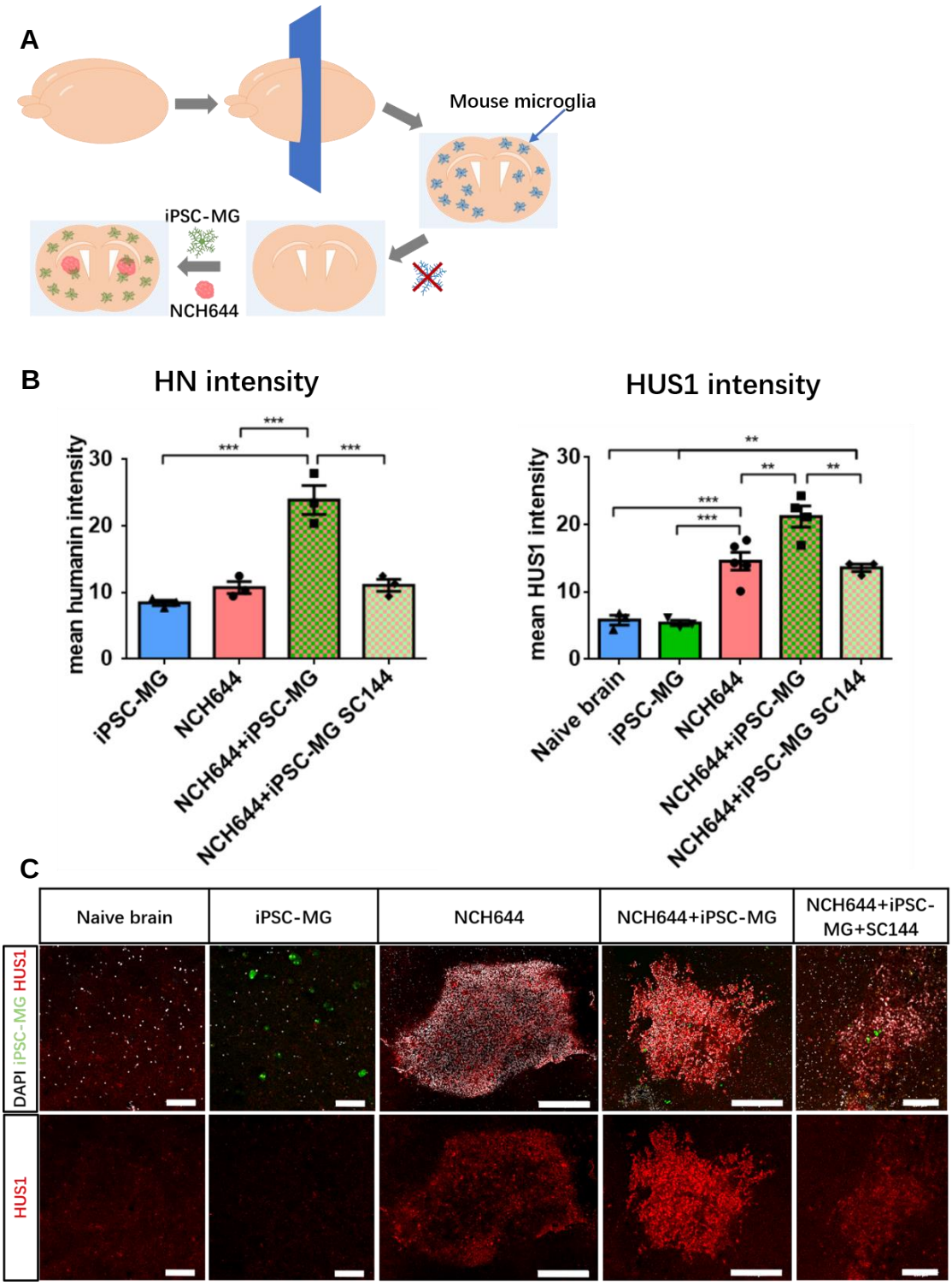

Figure 4.10: HUS1 expression in mouse brain slice preparations with hiPSC-MG and NCH644. **(A)** Workflow for preparation of *ex vivo* mouse brain samples with human iPSC-MG and NCH644. In brief, mouse brain was dissected and sectioned (using a vibratome) into 200 µm slices for culture. The endogenous microglia were depleted using clodronate liposome. Then hiPSC-MG and/or human hGBM line NCH644 were inoculated to the cultured mouse brain sample. **(B)** HUS1 and HN intensity analysis using ImageJ. For the samples with tumor, HUS1 and HN intensity was quantified only in the tumor area. Each animal is represented by a symbolic dot in the graph. **(C)**

Representative confocal images from immunofluorescence staining of HUS1(**red**). HiPSC-MG are with endogenous green fluorescence(**green**). Values are illustrated as mean ± SEM. One-way ANOVA followed by Tukey's multiple comparisons test was used to determine statistical significance between groups. $^{**}P \leq 0.01$, $^{***}P \leq 0.001$. Scale bars in naive brain and iPSC-MG=100 µm, scale bars in NCH644 group and NCH644+iPSC-MG group=500 µm, scale bars in NCH644+iPSC-MG+SC144 group=200 µm.

4.11 Humanin promotes GBM chemoresistance *in vivo*

Animal experiments were performed using immuno-incompetent mice. First, we aimed to determine whether HN can induce cytoprotective effects on NCH644 through the GP130 receptor *in vivo*, NCH644 was inoculated at 100,000 cells in 1 µL medium per mouse. Tumor growth was confirmed in a small cohort of mice 7 d after inoculation. The treatments were designed as follows: 1) aCSF, 2) HN, and 3) HN+BZA. 100 nM HN/aCSF was infused into the tumor by minipump directly after tumor inoculation, and the GP130 inhibitor BZA 4 mg/kg (or vehicle) was injected i.p. five times a week from day 7 after inoculation. The animals were sacrificed when they became symptomatic, and their brains were collected for further analysis after perfusion. Mouse brains were stained with HUS1 after sectioning, and HUS1 intensity was compared between groups. The result indicated a higher HUS1 intensity in the HN-treated group, and the increased intensity was counteracted when the GP130 inhibitor BZA was injected (Figure 4.11a E and F), which corroborated our *in vitro* findings. However, we did not observe a significant difference in survival between the two groups (Figure S4.11a). One possibility is that the protective effect of HN is more pronounced during chemotherapy. Thus, we conducted additional experiments in which TMZ treatment was also included. To be more specific, immuno-incompetent mice were inoculated with NCH644 HN-WT or NCH644 HN-C8A, and treated with TMZ or vehicle. In this experiment, additional mice with GL261 or with no tumor were also included for the comparison of HN expression. All animals with human GBM were sacrificed 23 d after inoculation. Immunohistochemistry revealed higher expression of HN in NCH644 HN-WT than in murine GL261 cells. The young mouse colon was used for positive control for HN expression (Figure 4.11a A-D)[78]. Tumor volume quantification showed NCH644 HN-C8A (function nullified HN) is sensitive toward TMZ chemotherapy, whereas

NCH644 HN-WT was resistant to TMZ treatment. We did not observe a significant difference in tumor volume between NCH644 HN-C8A and NCH644 HN-WT in no TMZ treated groups (Figure 4.11a G and H).

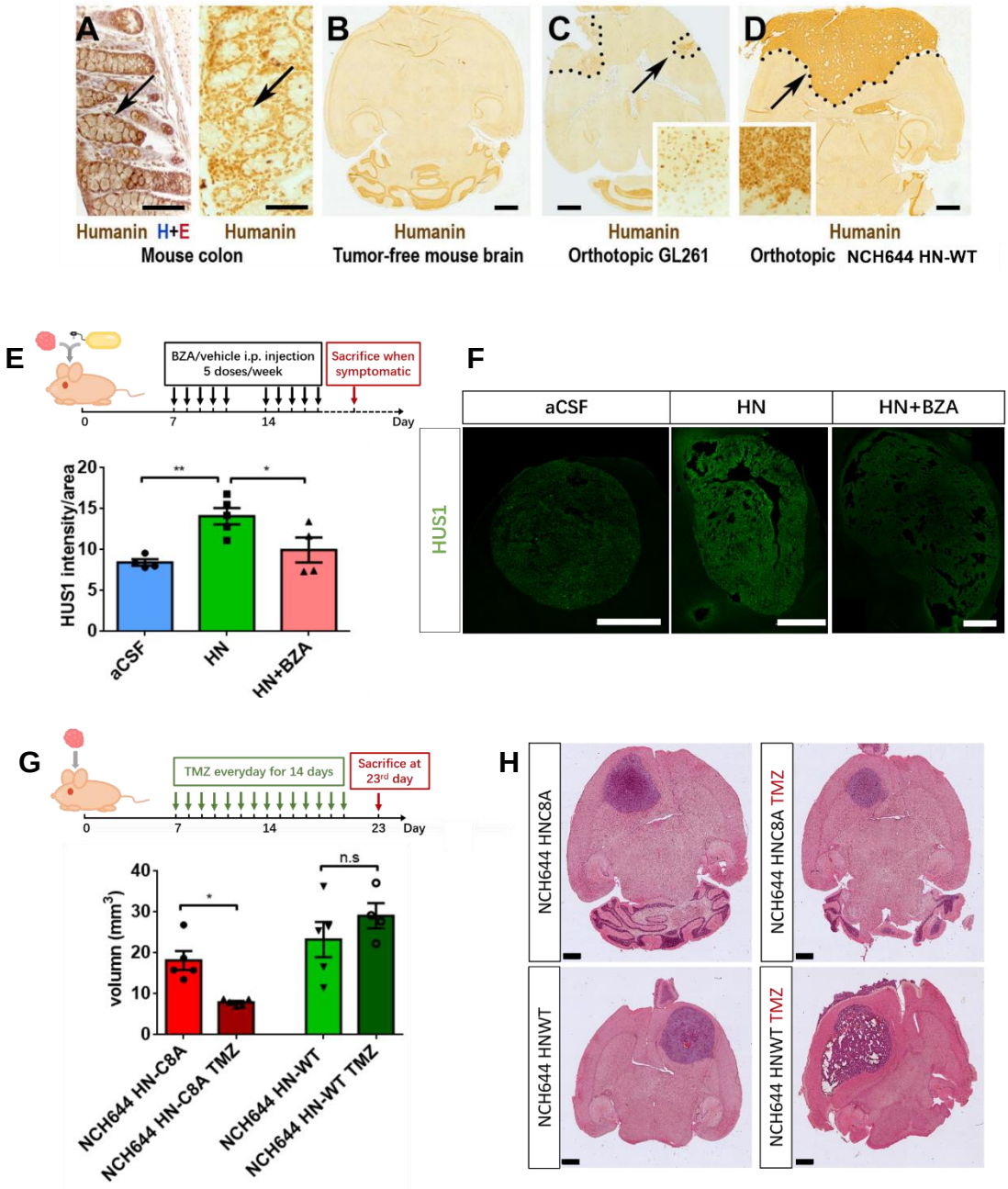

Figure 4.11a: Humanin enhanced HUS1 expression and induced chemoresistance *in vivo*. (A - C) Expression of a HN-like peptide in the mouse colon serves as a positive control for an immunostaining paradigm (using DAB staining and partly H&E, counterstaining), which revealed that the mouse forebrain (tumor-free, B) or mouse glioma models (GL261, C) are immunonegative for HN. **(D)** A humanized GBM mouse model is obtained after orthotopic xenografting HN-WT cells; we compared experimental GBM spreading both hemispheres (tumor is indicated by a dotted line; areas pointed out by arrows were magnified) and found that HN-WT GBM (but not GL261) strongly express HN. **(E)** Experimental schedule of the survival experiment. HUS1 expression

analysis based on immunostaining. **(F)** Confocal pictures illustrating different HUS1 intensity of tumors in three groups in survival study. **(G)** Experiment layout for tumor volume comparison between NCH644 HN-WT and NCH644 HN-C8A, in both TMZ-treated and non-treated conditions. Bar graph shows tumor volume at 23 d after inoculation. **(H)** H&E stainings show different tumor sizes in each group. Values are illustrated as mean ± SEM. One-way ANOVA followed by Tukey's multiple comparisons test was used to determine statistical significance between groups in E. One-way ANOVA followed by Sidak's multiple comparisons test was used to determine significant difference between groups in G. *$P \leq 0.05$, **$P \leq 0.01$, n.s=not significant. Scale bar=200 μm (A), =1 mm (B-D,F,H).

We next aimed to determine if HN also influences cells in the tumor microenvironment. We noticed that tumors overexpressing HN were more likely to have bleeding, irrespectively of TMZ treatment (Figure 4.11b A), which drew our attention to the effect of HN on vessels. Therefore, we performed H&E staining (Figure 4.11b C) and immunofluorescence staining (Figure 4.11b D) for the endothelial cell marker CD31[150] and pericyte marker PDGFRβ[151] on samples with NCH644 HN-WT and NCH644 HN-C8A, and quantified the vessel density and pericyte coverage of the vessels in the tumor area. This revealed a preponderance of abnormally shaped and condensed vessels in the HN-overexpressing tumor compared with the HN-free hGBM tumor. Interestingly, pericyte coverage and vessel density was much higher in HN-overexpressing tumors (Figure 4.11b B). It remains to be investigated why NCH644 HN-WT with higher vessel density and pericyte coverage is more likely to cause bleeding.

As TAMs account for approximately 30% of the tumor mass and play an essential role in immunosuppression and tumor expansion[20, 21], we further examined the effects of HN on TAMs to determine whether HN can affect tumor cells through TAMs. Another immunostaining experiment was performed using the TAM marker IBA1 and endothelial cell marker CD31. We observed a higher density of TAMs in the tumor area of NCH644 HN-WT than in NCH644 HN-C8A, and there were more TAMs that are not attached to the vessel (Figure 4.11b E and F). Whether this indicates a more abundant infiltration of TAMs into the HN-overexpressing tumor, or if there is any

relationship between the high infiltration of TAMs and the chemoresistance in HN-overexpressing tumor requires further study.

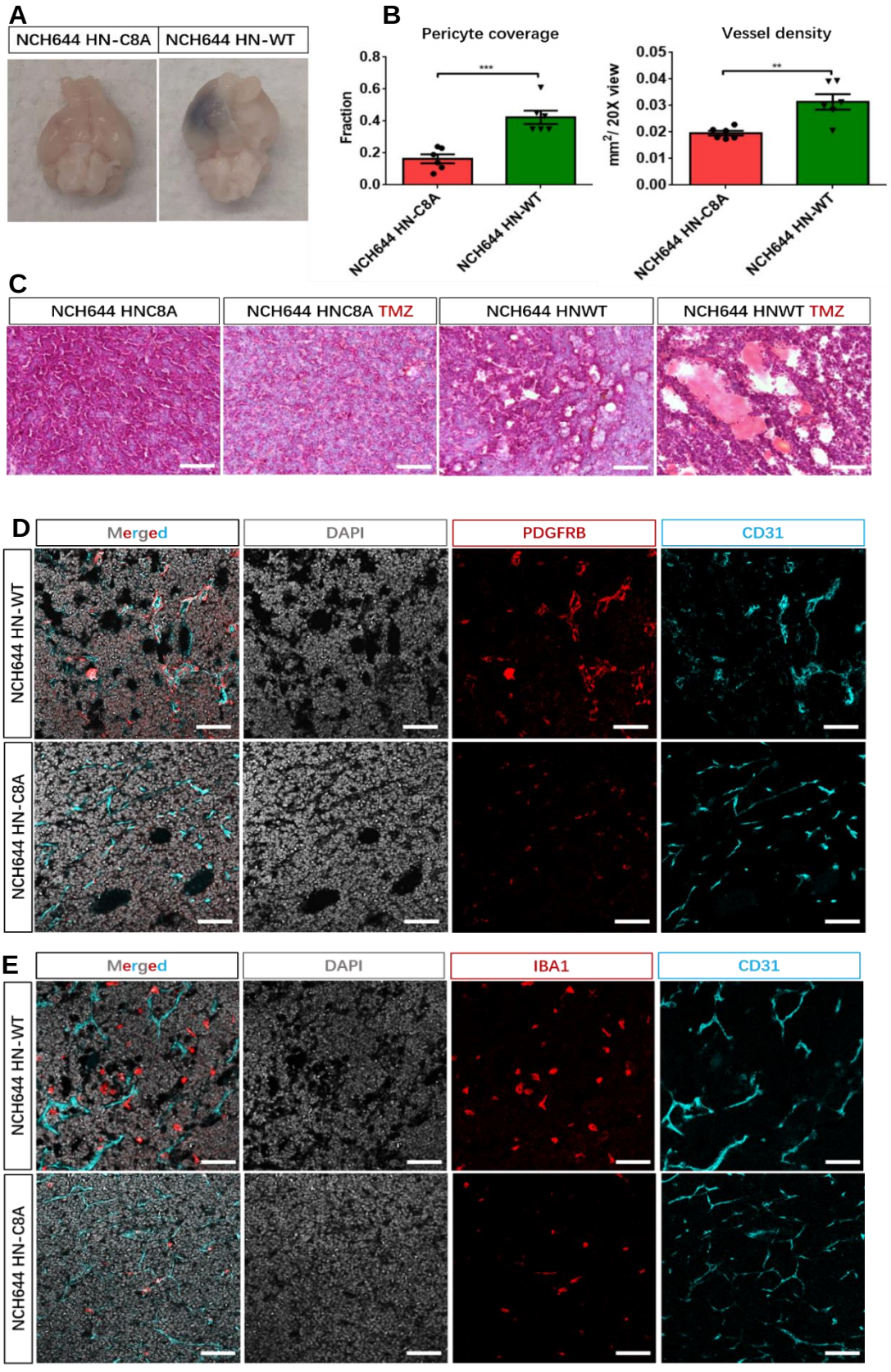

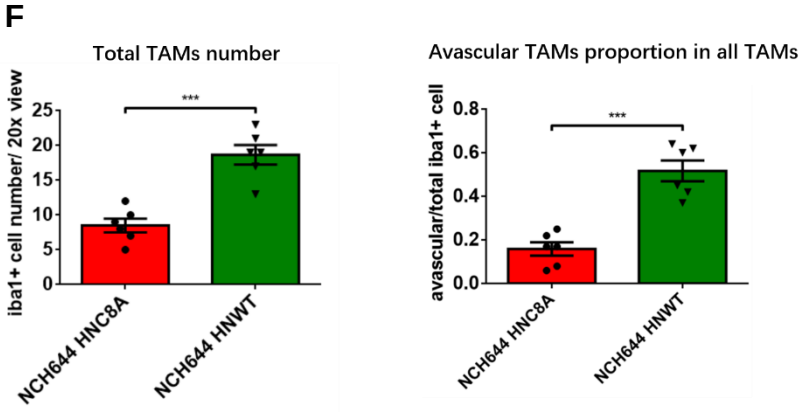

Figure 4.11b: Humanin induced vascular changes in mouse GBM xenograft models. **(A)** Comparison between mouse brains (bottom side) bearing NCH644 HN-C8A (left) and NCH644 HN-WT (right) harvested 23 d after inoculation. NCH644 HN-WT shows more bleeding than NCH644 HN-C8A in the tumor area. **(B)** Vessel analysis between NCH644 HN-C8A and NCH644 HN-WT without TMZ treatment using confocal images. Pericyte coverage was analyzed using the ImageJ software and was calculated as PDGFRβ$^+$CD31$^+$ area/CD31$^+$area. Vessel area was evaluated using the AngioTool software. **(C)** H&E staining showing different vessel shape in tumor area of NCH644 HN-WT (bigger lumen) and NCH644 HN-C8A. **(D)** Typical confocal pictures (under 20 × objective) of vasculature in NCH644 HN-WT (upper) and NCH644 HN-C8A (lower). Pericytes were stained with PDGFRβ (**red**), endothelial cells with CD31 (**cyan**). **(E)** Typical confocal pictures (under 20 × objective) of IBA1$^+$ TAMs in NCH644 HN-WT (upper) and NCH644 HN-C8A (lower), as well as TAMs spatial relationship with vessel. TAMs were stained with IBA1 (**red**), endothelial cells with CD31(**cyan**). **(F)** TAMs analysis of NCH644 HN-C8A and NCH644 HN-WT tumors without TMZ treatment basing on the confocal pictures. IBA1$^+$ TAMs cell numbers were counted and are presented on the left. Avascular TAMs (TAMs that are not attached to vessels) percentages in all TAMs are illustrated on the right. Each symbolic dot represents the averaged value from three pictures. Values are illustrated as mean ± SEM. t test was used to determine statistical significance between groups. $^{**}P \leq 0.01$, $^{***}P \leq 0.001$. Scale bar=100 μm.

Since we observed HN-induced tumor expansion especially under TMZ treatment *in vivo*, we conducted another survival experiment to determine whether the tumor-promoting effect of HN can be blocked with a GP130 inhibitor (and sensitize GBM to chemotherapy with TMZ). The experimental groups were designed as follows: 1) 100 nM HN+ 50 mg/kg TMZ, and 2) 100 nM HN+ 50mg/kg TMZ+ BZA 40mg/kg[108]. NCH644 was inoculated (100,000 cells/μL) and a minipump infusing HN or aCSF was directly installed after tumor inoculation. TMZ (five times a week) and BZA (every other day) were applied i.p. from day 7 after NCH644 inoculation. The animals were sacrificed when they were symptomatic.

No difference in survival was observed between the two groups (Figure S4.11c A). However, it was noticed that after BZA 40 mg/kg application, animals experienced apparent weight loss after one week, which was also noticed in another study[108]. Weight loss was approximately 10% of the original weight when they became symptomatic (Figue S4.11c B). Therefore, we wondered if the animals were sick because of the side effects of BZA. This question prompted us to further examine the tumors in each animal in the two groups. First, we observed, by generally inspecting the brain surface (when collecting mouse brains), a higher percentage of tumors with bleeding in the HN-treated group, some of which had subarachnoid hemorrhage (Figure 4.11c A). Second, tumor volume was quantified. Interestingly, the tumor volume in HN+TMZ+BZA group was significantly smaller than that in the HN+TMZ group (Figure 4.11c B), although these two groups of animals did not show a survival difference. Another interesting finding was that not only the tumor volume was smaller in the HN+TMZ+BZA group, but the tumor cells also did not appear to be in "good shape" in this group, as a large number of cells showed morphological signs of apoptosis, indicating that BZA sensitizes tumors to TMZ treatment[185]. Staining for cleaved caspase-3 confirmed this observation (Figure 4.11c C, Figure 4.11d A and B). Furthermore, we found many apoptotic cells in HN+TMZ+BZA group were remote from some vessel-like structures. We questioned if these cells have died of insufficient blood supply (Figure 4.11c D). CD31 and PDGFRβ were immunostained for vasculature. We noticed that, vessel density was much higher in the HN+TMZ group than in the HN+TMZ+BZA group (Figure 4.11d C and D), indicating that the blockade of GP130 by BZA decreased the vascular development in the tumor, which is in accordance with previous results that NCH644 HN-WT tumor has a higher vessel density compared with NCH644 HN-C8A (Figure 4.11b B and D).

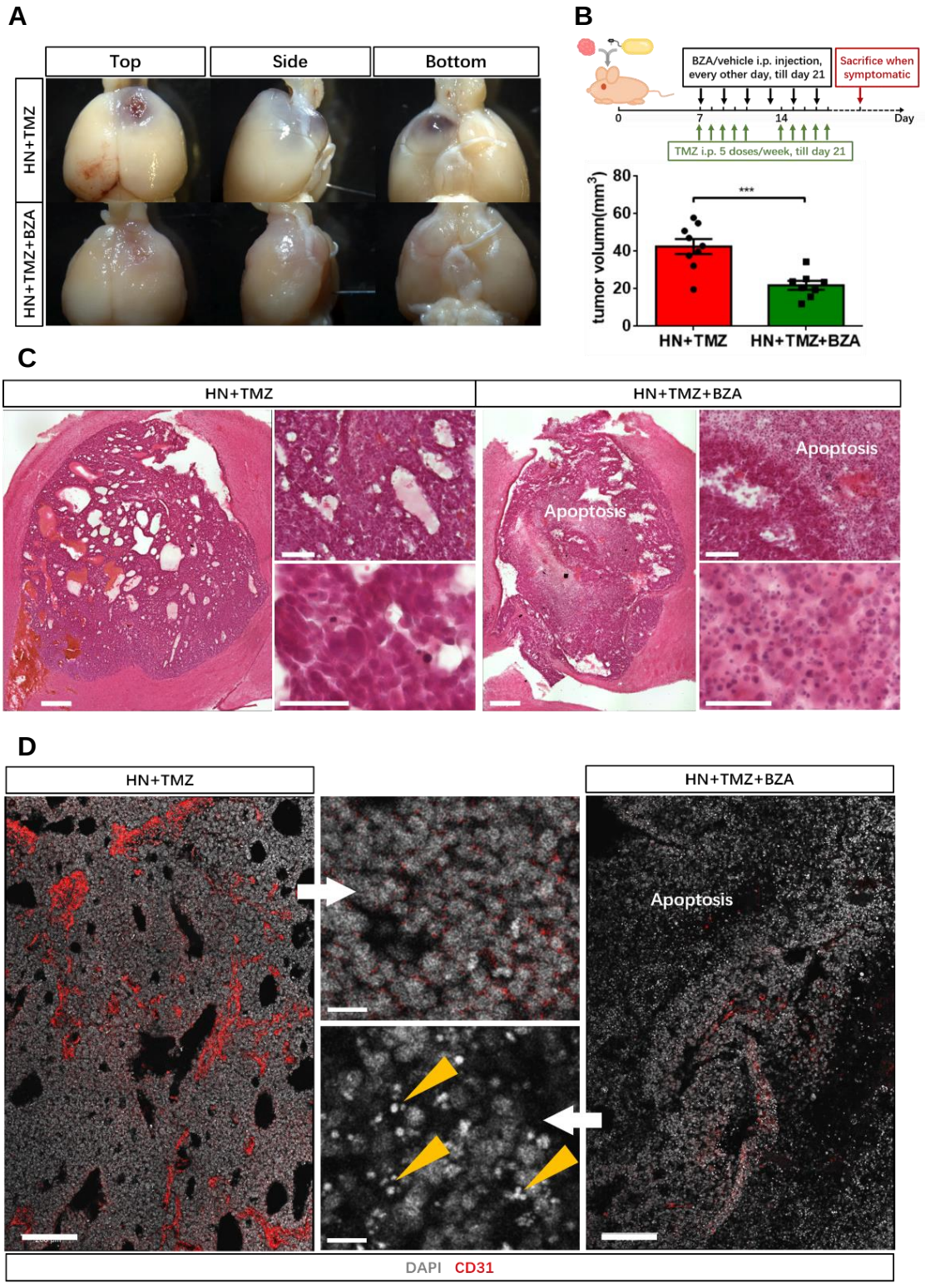

Figure 4.11c: The GP130 inhibitor BZA sensitized Humanin-perfused tumors to TMZ treatment. (A) Mice brains were collected when mice were symptomatic. The HN+TMZ group exihibited more bleeding than the HN+TMZ+BZA group. **(B)** Schedule of treatments in the survival experiment; tumor volume was quantified and compared. **(C)** H&E staining showing different levels of apoptosis in the tumor area between HN+TMZ and HN+TMZ+BZA groups. In the HN+TMZ+BZA group, many condensed nuclei can be seen, indicating apoptosis. **(D)** Endothelial

cells are labelled with CD31(**red**); immunofluorescence staining shows high vessel density and less apoptosis in HN+TMZ group, and low vessel density with more apoptosis (judging by DAPI staining, marked with **yellow** arrow) in HN+TMZ+BZA group, especially in the area far away from vessel. Each symbolic dot represents one experimental animal. Values are illustrated as mean ± SEM. The t test was used to determine statistical significance between groups. ***$P \leq 0.001$. Scale bar (C overview) =500 μm, =100 μm (C upper magnification)，=50 μm (C lower magnification), =200 μm (D overview), =20 μm (D magnification).

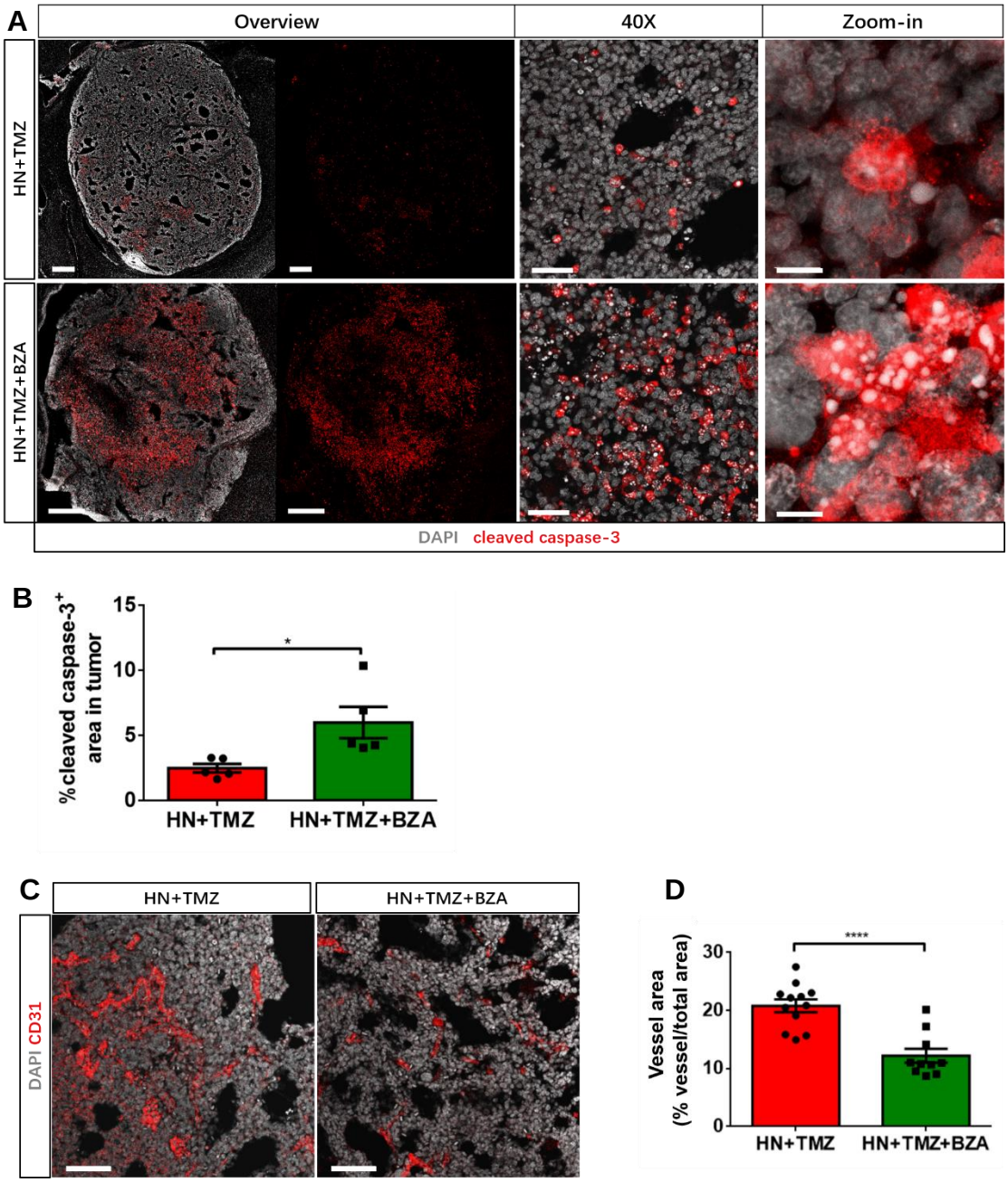

Figure 4.11d: The GP130 inhibitor BZA sensitized Humanin-perfused tumors to TMZ treatment and decreased angiogenesis. (A) Cleaved caspase-3 (**red**) staining illustrated more apoptosis cells in the HN+TMZ+BZA group than in the HN+TMZ group. **(B)** Comparison of

percentage for cleaved caspase-3^+/$DAPI^+$ in tumor area. **(C)** Endothelial cells stained with CD31 (**red**) showing different vasculature in two groups. **(D)** Comparison of vessel density between two groups. Each symbolic dot represents the averaged value from three overview pictures. Values are illustrated as mean ± SEM. The t test was used to determine statistical significance between two groups. Welch's correction was used for the comparison with heterogenous variance. *P≤0.05, ****P≤0.0001. Scale bar (A overview)=500 µm, =50 µm (A 40 ×), =10 µm (A zoom-in), =100 µm (C).

In order to continue to study the effects of GP130 inhibition on overall survival of TMZ treated, HN releasing GBM (HN-WT) we used brain infusion of SC144 (10 µM) or aCSF; all mice received TMZ (50 mg/kg, i.p.). Again, the blockade of GP130 had a strong TMZ-therapy supporting effect in HN secreting GBM. Experimental controls (TMZ + aCSF) had an average survival time of 18 days, whereas co-administration of TMZ and SC144 significantly prolonged overall survival towards 25 days (Figure 4.11e).

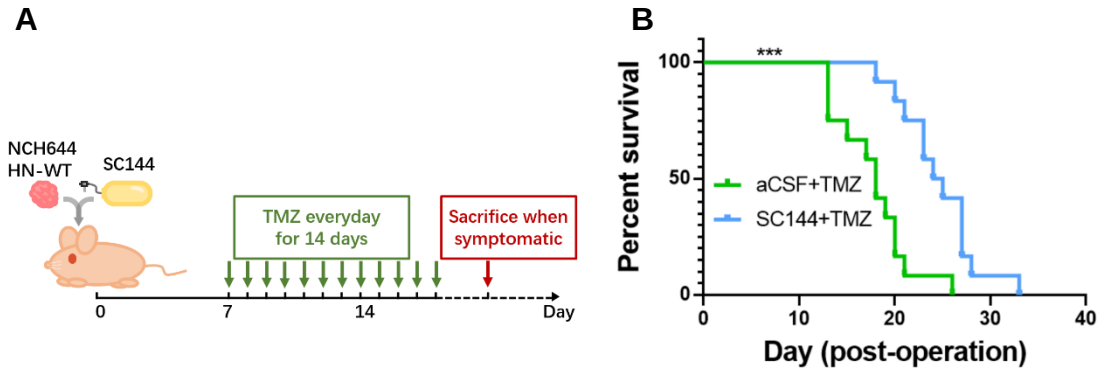

Figure 4.11e: TMZ combined with blockade of GP130 by SC144 prolonged mouse survival in a GBM model. (A) Schematic plan for the survival experiment. **(B)** Survival comparison between aCSF+TMZ and SC144+TMZ groups using Log-rank (Mantel-Cox) test. SC144 infusion extended NCH644 HN-WT bearing mouse survival. ***P≤0.001.

5. Discussion

Transcriptomics of TAMs in human GBM samples indicated upregulation of the mitochondrial ribosomal subunit MT-RNR2 in TAMs compared with other components in GBM. MT-RNR2 contains an ORF for the human-specific signaling peptide humanin (HN), which was originally reported in AD patients and has been extensively studied for its cytoprotective effect on neurons to defend against Aβ attack[76]. This attracted our attention and prompted us to investigate the effect of HN on the progression of GBM. We raised the following questions: Does the upregulation of MT-RNR2 in TAMs result in a higher expression of HN? Does the interaction of TAM with hGBM promote HN expression? Is HN a paracrine or an intracellular signaling cue in GBM? Does HN have protective effect on tumor cells? Is HN signaling a therapeutic target in GBM? To answer these questions, we conducted a series of experiments.

First, to confirm the HN expression level in TAMs, paraffin-embedded samples of tumor areas (versus tumor free area) from GBM patients were used for HN staining. Immunohistochemistry revealed that the HN peptide was preponderant in TAMs and was also detectable in tumor cells. Since HN expression in microglia is comparatively low in tumor-free brain, and TAM and GBM cells had remarkably high HN levels we hypothesized if this was a consequence of the interaction of these two cell types. Next, to test whether GBM cells can respond to exogenously applied HN, we performed a large series of experiments investigating hGBM expansion *in vitro*[145]. Based on these results, we classified the human hGBM lines into two categories: HN-sensitive hGBM (NCH644, NCH684 and GBM20) and HN-insensitive hGBM (Line2, Line10, and Line11). HN-sensitive hGBM showed significantly enhanced expansion under HN concentration at nanomolar range as low as 20 nM under growth factor-deprived conditions. In addition, HN also helps tumor cells to build up chemoresistance towards TMZ. Next, to determine whether HN also acts through an intracellular mechanism, we conducted *in vitro* experiments using HN-sensitive hGBM NCH644 overexpressing

HN-WT, HN-C8A, or HN-L9R which cannot be secreted but still has a cytoprotective effect when applied as a recombinant peptide[76]. No difference in proliferation was observed when the three cell lines were plated at low density (50,000 cells/mL). However, when seeded at a 10-fold higher density, NCH644 HN-WT expanded much faster than NCH644 HN-C8A and NCH644 HN-L9R, and no difference was found between the two mutant lines. This indicated a concentration-dependent manner of HN activity and that the tumor growth promoting effect of HN effect depends on paracrine.

Other studies have shown that HN inhibits cell death by extracellular binding to FPR2, or to a trimeric plasma membrane receptor (comprising the receptor subunits CNTFR, WSX-1, and GP130)[105, 109]. Therefore, to investigate which receptor HN binds to in human hGBM cell lines, we used qPCR to detect CNTFR, WSX-1, IL6ST(GP130) and FPR1/2. We did not detect FPR1/2 in HN-sensitive hGBM or HN-insensitive hGBM, but the trimeric receptors subunits, CNTFR, WSX-1, and GP130, were detectable. Interestingly, we found that all HN-sensitive hGBM fell into a group of hGBM cells that had high transcription of GP130. Thus, we tested whether a GP130 inhibitor could block the effect of HN. We noticed that both SC144 and the clinically used BBB-permeable inhibitor BZA[108] could counteract the HN growth promoting effect and the chemoresistance to TMZ *in vitro* and *in vivo*. Furthermore, by Western Blotting we noticed HNG could activate ERK1/2, suggesting that HN may stimulate signaling pathways related to ERK1/2 mediated by the GP130 receptor. An additional experiment, including pre-treatment with the GP130 inhibitor SC144 and stimulation of HNG is needed to further support the signaling pathway triggered by the GP130 receptor. Several studies have shown that aberrant activation of GP130 plays an essential role in enhancing GBM progression, for example, macrophages can induce GBM cells to enter a more aggressive mesenchymal-like state through the GP130/STAT3 mechanism[186, 187]. CD109 interacts with the GP130/STAT3 axis in GSCs to maintain the stemness and induce the chemoresistance[188]. The GP130 inhibitor BZA increased survival in GBM, although this therapeutic agent has toxicity

problems[108]. Our findings revealed protumorigenic effect of HN through GP130 receptor.

RNAseq revealed the involvement of the ATR pathway-related DNA repair gene HUS1 in the tumor promoting effect of HN. This finding was further confirmed by *in vitro* and *in vivo* studies. First, highly expanded NCH644, induced by overexpression of HN-WT or conditioned medium containing HN, showed higher HUS1 expression (as determined by immunofluorescence staining). Next, we asked whether the high expression of HUS1 indicates the activation of the ATR-related DNA repair pathway. We addressed this question by examining if an ATR inhibitor can block the high proliferation of HN-sensitive hGBM induced by HN. We confirmed the involvement of the ATR pathway in the HN signaling. Cell cycle analysis showed that under TMZ treatment, HN decreased the sub-G1% peak, which represents the apoptotic population. Live imaging revealed an abnormal mitosis where tumor cells formed two daughter cells with uneven Histone2B-GFP distribution (one daughter cell without nuclei). We found that Histone2B-GFP free daughter cells were less frequent in the HN-treated groups. The occurrence of daughter cells without nuclear DNA has (to the best of our knowledge) not been reported previously. By interrogating the TCGA and GTEx databases, we found a negative prognostic property of HUS1 in GBM patients, where high HUS1 expression is related to poor survival. Our study is the first to report the potential effect of HUS1 to promote GBM expansion.

HN peptide was detectable in the mouse colon, but not in the mouse forebrain. Therefore, we used hiPSC-MG and NCH644 from human sources and grew them in sectioned and cultured mouse brains to provide the “soil” for tumor growth. We observed an increased signal of HN and HUS1 in NCH644 cells co-cultured with hiPSC-MG compared to that in tumor cells or hiPSC-MG alone. Blocking GP130 using SC144 inhibited the elevation of HN and HUS1 level in NCH644. This confirmed our hypothesis that elevated HN in TAM and GBM depends on the interaction of TAM and GBM cells through GP130. So far, we have not conducted experiments to directly

visualize the binding of paracrine HN and GP130, or the following translocation in tumor cells. This can be achieved in our future experiment by culturing an HN-sensitive hGBM, such as NCH644, in a medium containing fluorophore-labeled HN peptide, and by live imaging we check if there will be internalization of fluorescent HN in the tumor cells. Moreover, to further clarify the origin of the protumorigenic HN, other experiments, such as comparing the effect of HN knock-down in TAMs and hGBM, can be performed. Or, it is also possible to use in situ hybridization to check the HN mRNA level in GBM and TAM in the *ex vivo* cultivated brain slices.

The *in vivo* studies further corroborated our *in vitro* results. The NCH644 xenograft model showed decreased tumor size under TMZ, whereas HN induces chemoresistance in GBM. We also observed the effect of HN on the tumor environment. Higher vessel density and pericyte coverage were found in HN-overexpressing tumors. Robust proliferating angiogenesis is the main feature of GBM and is characterized by a glomeruloid microvasculature (highly proliferating small blood vessels within tumor mass)[189, 190]. The tumor vasculature comprises endothelial cells as main structure, supported by pericytes, astrocytes and perivascular macrophages[191, 192]. An abundant vasculature in GBM provides oxygen and nutrients for tumor expansion[193]. Under physiological conditions, pericytes together with endothelial cells and astrocytes maintain the stability of the BBB[194]. In GBM, this barrier can become an obstacle for therapeutic treatment and block the access of therapeutics into the tumor mass. Targeting pericyte can disrupt the BBB and improve chemotherapeutic efficiency[195]. Therefore, we hypothesize that the abundant vasculature with high pericyte coverage induced by HN is another factor that induces the rapid expansion and chemoresistance of GBM. We also observed that there is more bleeding in HN overexpression tumor. Clinically, bleeding tends to occur in highly malignant gliomas. For example, 5-8% of the patients with GBM were affected by bleeding[196]. To our knowledge, high pericyte coverage is usually related to a less permeable BBB[194]. Why the high pericyte coverage coexists with higher frequency of bleeding after HN treatment is still unknown. Studies showed that intra-tumoral hemorrhage can be triggered by multiple

mechanisms including local factor such as therapeutic radiation and tumoral necrosis, or systemic reasons like hypertension and anticoagulation medication[196, 197]. We found HN overexpression tumors have more abundant vasculature, and these newly formed vessels are usually abnormal in function and structure, which can induce hypoxia and necrosis in tumor cells[198, 199], thus possibly tending to induce the intra-tumoral hemorrhage. This will be further investigated in a future study.

Overall, we identified for the first time the mechanism by which the mitochondria-encoded peptide HN induces GBM expansion and chemoresistance through GP130. Blocking the pro-tumorigenic effects of HN is a potential therapeutic adjuvant (Figure 5).

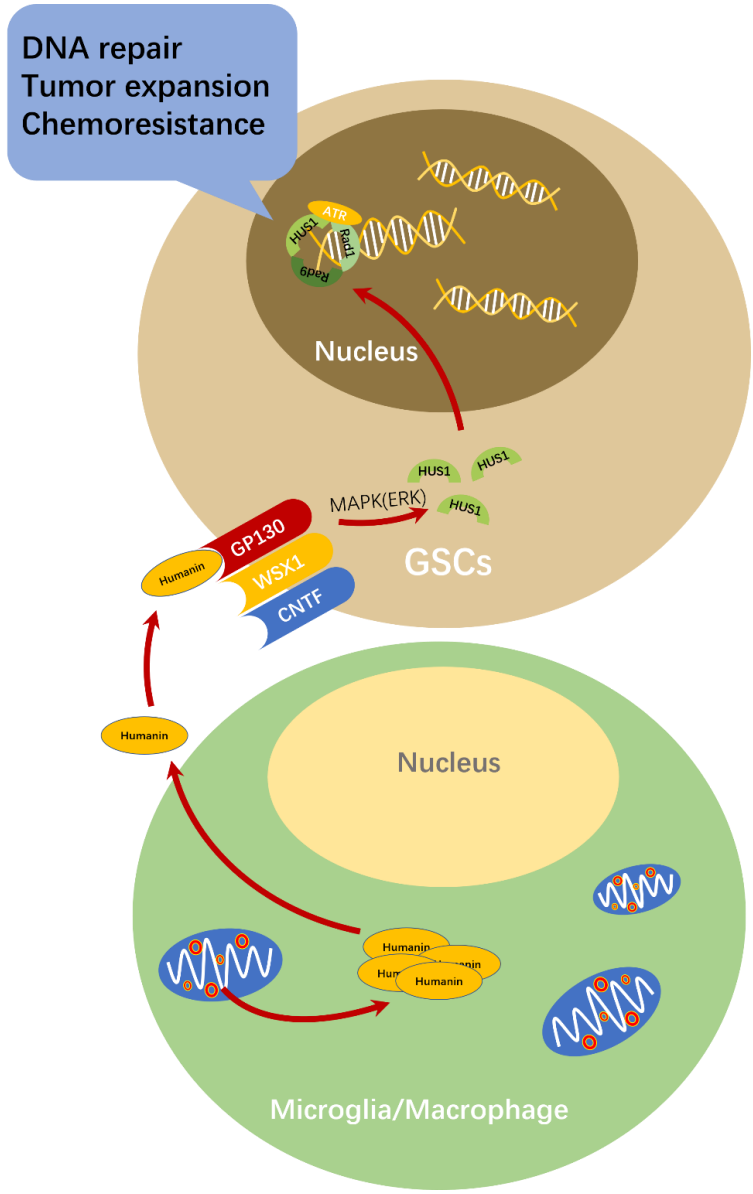

Figure 5: Schematic overview on Humanin-induced GBM expansion and chemoresistance. Transcriptomics of human TAM indicated an upregulation of the mitochondrial ribosomal subunit MT-RNR2 which contains an open reading frame for the human-specific signaling peptide HN. Immunohistology disclosed that HN was preponderant in TAMs and partly expressed in GBM cells. Paracrine HN supports the expansion of hGBM via stimulation of a trimeric cytokine receptor containing the the GP130/IL6ST subunit. HN-induced GP130 activation promotes hGBM resistance to TMZ by inducing the ATR / HUS1-dependent DNA-repair machinery.

6. Supplementary materials

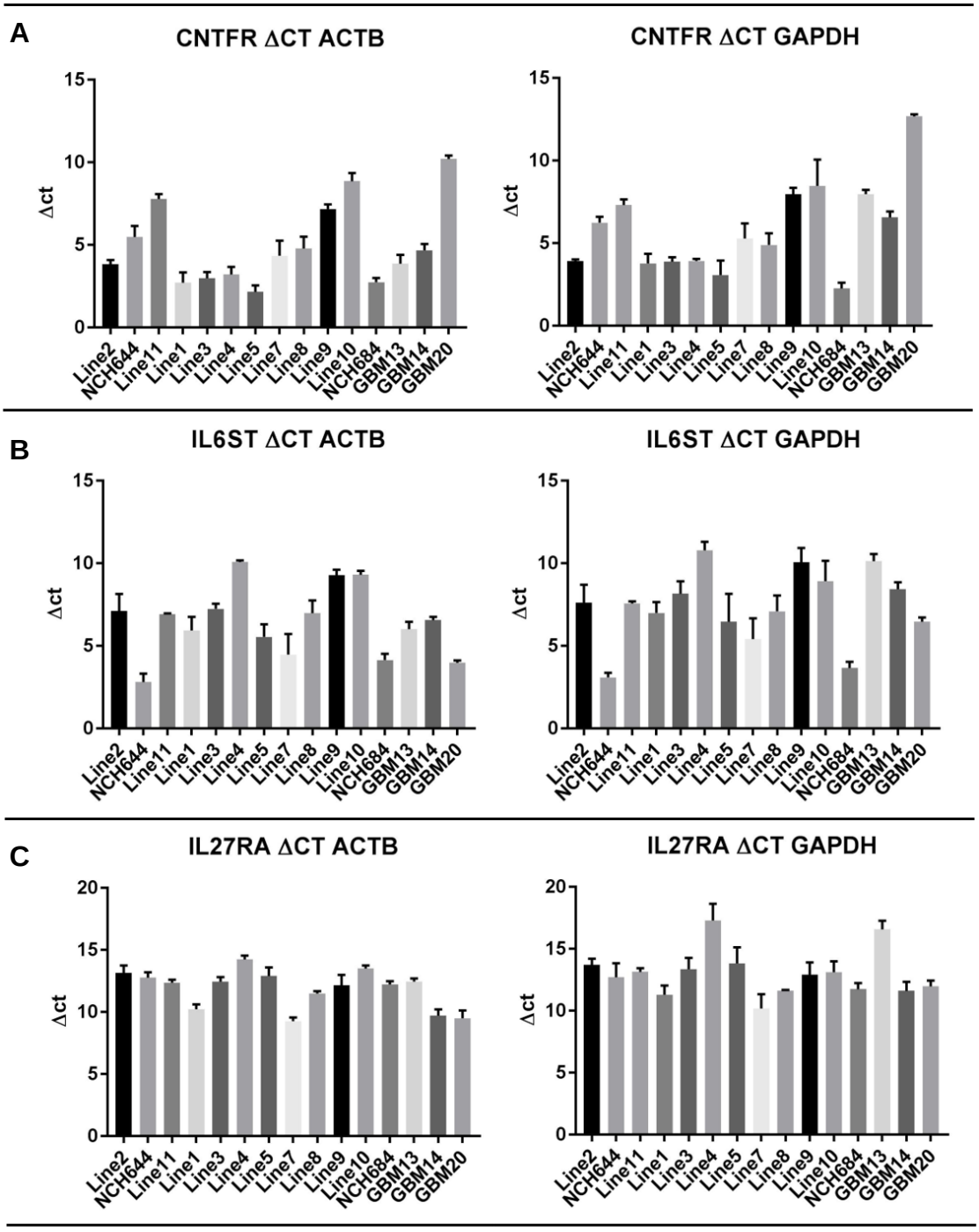

Figure S4.6.1a: QPCR detects subunits of the trimeric interleukin receptor (CNTFR/ WSX-1/ IL6ST). (A) Δct value of CNTFR obtained using qPCR, with ACTB or GAPDH as internal control. **(B)** Δct value of IL6ST(GP130) obtained using qPCR, with ACTB or GAPDH as internal control. **(C)** Δct value of IL27RA(WSX-1) obtained using qPCR, with ACTB or GAPDH as internal control. Values are illustrated as mean ± SEM.

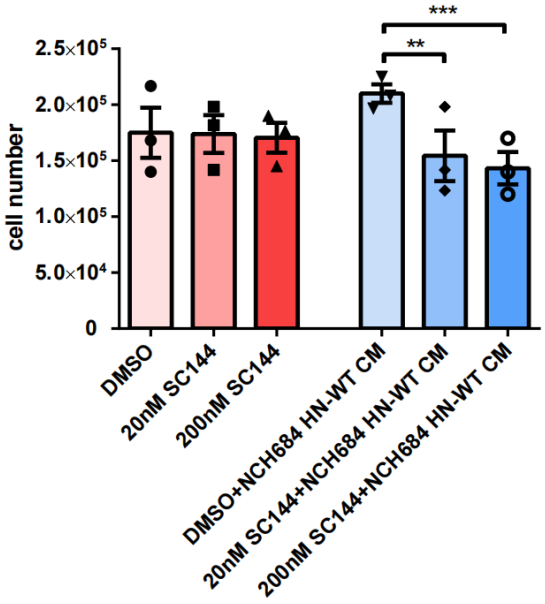

Figure S4.6.1b: Working concentration of SC144 for conditioned medium experiments. SC144 working concentration was test on NCH644 treated with conditioned medium from NCH684 HN-WT. Cells were plated at 20,000 cells in 0.5 mL conditioned medium or growth factor-deprived medium per well. Conditioned medium was changed and treatment was applied every other day as indicated in the graph. Cells were counted 7 d after seeding. Both 20 nM and 200 nM SC144 can block the protective effect of HN. Conditioned medium is abbreviated as "CM" in the graph. Three technical replicates were prepared and every individual experiment is shown as a symbolic dot in the graph. Values are illustrated as mean ± SEM. One-way ANOVA followed by Tukey's multiple comparisons test was used to determine significant difference between groups. $^{**}P \leq 0.01$, $^{***}P \leq 0.001$.

A

Each antibody is spotted in duplicate vertically		A	B	C	D	E	F	G	H	I
	1	POS 1	POS 2	POS 3	BLANK	NEG	EGFR (P-Tyr845)	EGFR (P-Tyr922)	EGFR (P-Tyr1045)	EGFR (P-Tyr1068)
	2									
	3	BLANK	BLANK	BLANK	BLANK	EGFR (P-Tyr1086)	EGFR (P-Tyr1148)	EGFR (P-Tyr1173)	EGFR (SER 1046/1047)	BLANK
	4									
	5	ErbB2 (P-Tyr877)	ErbB2 (P-Tyr112)	ErbB2 (P-Tyr 1221/1222)	ErbB2 (P-Tyr1248)	ErbB2 (P-Thr686)	ErbB2 (P-Ser1113)	ErbB3 (P-Tyr1289)	ErbB4 (P-Tyr1284)	BLANK
	6									
	7	EGFR	ErbB2	ErbB3	ErbB4	BLANK	BLANK	NEG	BLANK	POS4
	8									

control

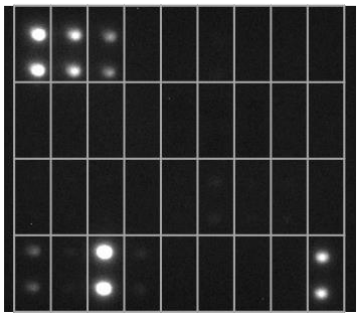

HN 100nM treated(25min)

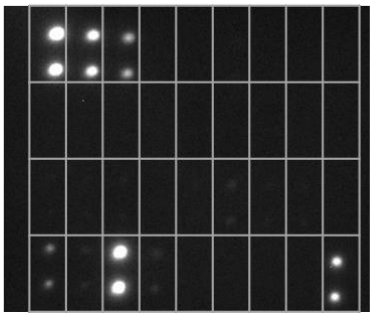

B

	A	B	C	D	E	F	G	H	I	J	K	L
1	POS1	POS1	POS2	POS2	POS3	POS3	ABL1	ABL1	ACK1	ACK1	ALK	ALK
2	NEG	NEG	NEG	NEG	Axl	Axl	Blk	Blk	BMX	BMX	Btk	Btk
3	Csk	Csk	Dtk	Dtk	EGFR	EGFR	EphA1	EphA1	EphA2	EphA2	EphA3	EphA3
4	EphA4	EphA4	EphA5	EphA5	EphA6	EphA6	EphA7	EphA7	EphA8	EphA8	EphB1	EphB1
5	EphB2	EphB2	EphB3	EphB3	EphB4	EphB4	EphB6	EphB6	ErbB2	ErbB2	ErbB3	ErbB3
6	ErbB4	ErbB4	FAK	FAK	FER	FER	FGFR1	FGFR1	FGFR2	FGFR2	FGFR2 (α isoform)	FGFR2 (α isoform)
7	Fgr	Fgr	FRK	FRK	Fyn	Fyn	Hck	Hck	HGFR	HGFR	IGF-IR	IGF-IR
8	Insulin R	Insulin R	Itk	Itk	JAK1	JAK1	JAK2	JAK2	JAK3	JAK3	LCK	LCK
9	LTK	LTK	Lyn	Lyn	MATK	MATK	M-CSFR	M-CSFR	MUSK	MUSK	NGFR	NGFR
10	PDGFR-α	PDGFR-α	PDGFR-ß	PDGFR-ß	PYK2	PYK2	RET	RET	ROR1	ROR1	ROR2	ROR2
11	ROS	ROS	RYK	RYK	SCFR	SCFR	SRMS	SRMS	SYK	SYK	Tec	Tec
12	Tie-1	Tie-1	Tie-2	Tie-2	TNK1	TNK1	TRKB	TRKB	TXK	TXK	NEG	NEG
13	Tyk2	Tyk2	TYRO10	TYRO10	VEGFR2	VEGFR2	VEGFR3	VEGFR3	ZAP70	ZAP70	POS4	POS4

control

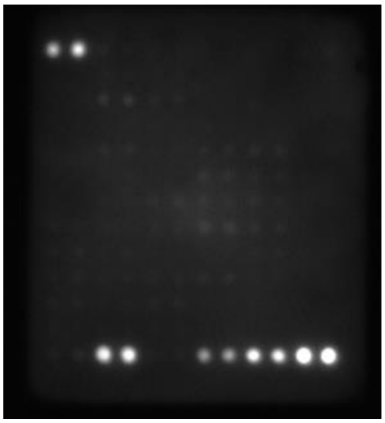

HN 100nM treated(25min)

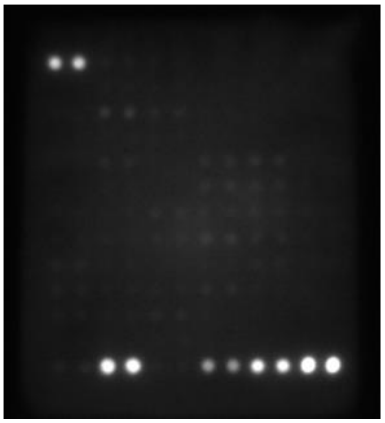

Figure S4.6.3: Immune-blot does not detect activation of tyrosine kinases-receptor or EGF-

receptor after Humanin application. (A) EGF-receptors immuno-blot showed no difference between control and HN treated NCH644 (100 nM 25 min). **(B)** Tyrosine kinases-receptors immune-blot also showed no difference between control and HN treated NCH644 (100 nM 25 min).

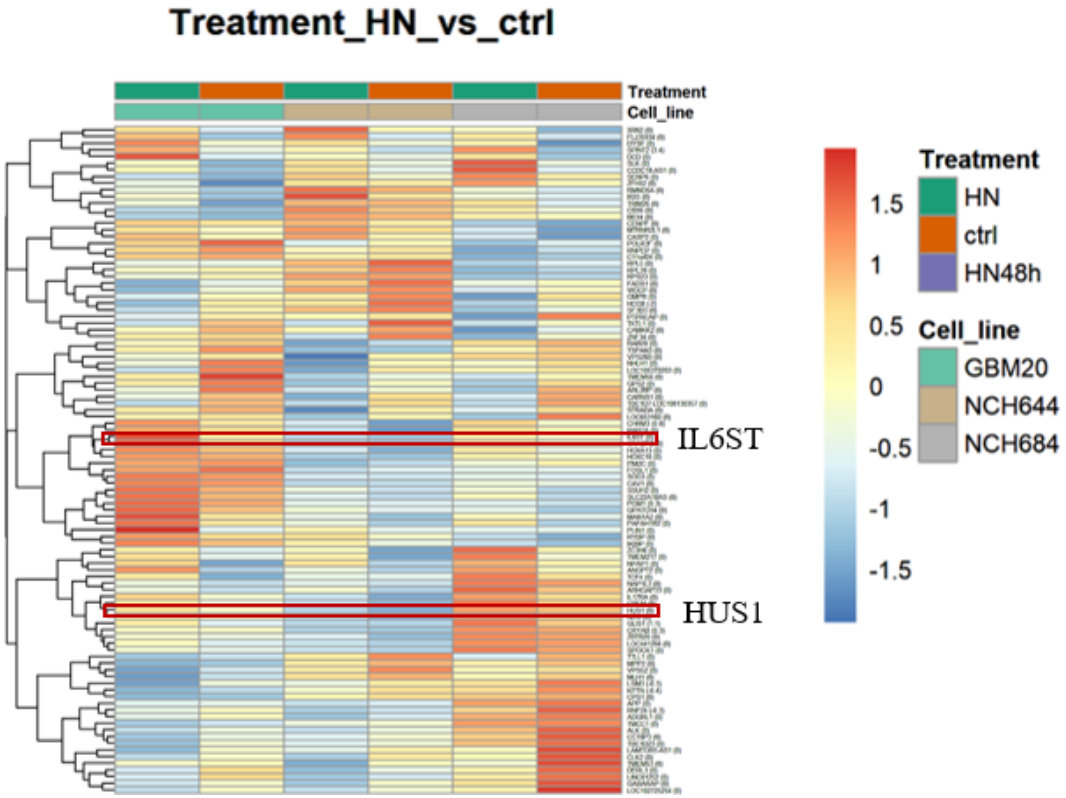

Figure S4.7: IL6ST (GP130) and HUS1 are upregulated after HN-treatment in HN-sensitive hGBM. The expression of the top 100 most differentially expressed genes HN across the treatments and cell lines are shown. In the heatmap the genes are ranked by the unadjusted p-value. RNAseq results show that, in HN-treated HN-sensitive hGBM there were higher transcription of HUS1, an ATR-dependent DNA-repair related DNA-clamp component, as well as higher IL6ST (GP130) level, compared to controls.

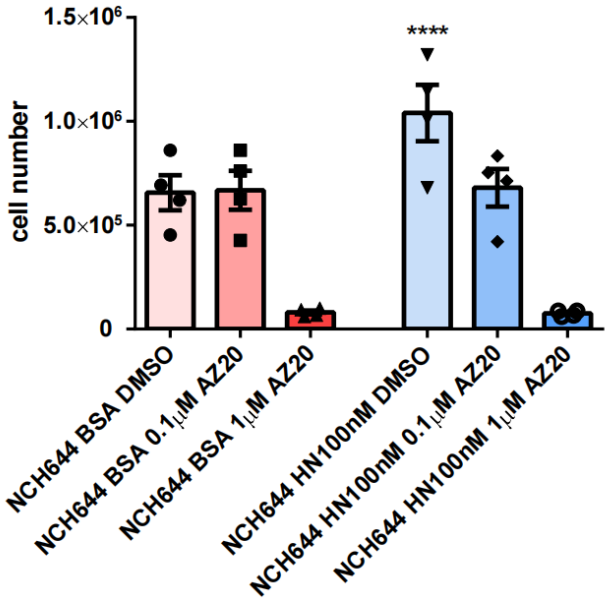

Figure S4.8: Testing the working concentration of AZ20. The ATRi AZ20 working concentration was tested on NCH644. Cells were plated at 100,000 cells in 2 mL growth factor-deprived medium per well. Treatment was added every other day as indicated in the graph. Cells were counted 6 d after seeding. Three technical replicates were prepared in each independent experiment. Averaged values from each experiment are illustrated as mean ± SEM. One-way ANOVA followed by Tukey's multiple comparisons test was used to determine significant difference between groups. ****$P \leq 0.0001$ compared with all the other groups. 0.1 µM AZ20 was selected as this concentration showed blocking effect of HN and at the same time did not do harm to the cells.

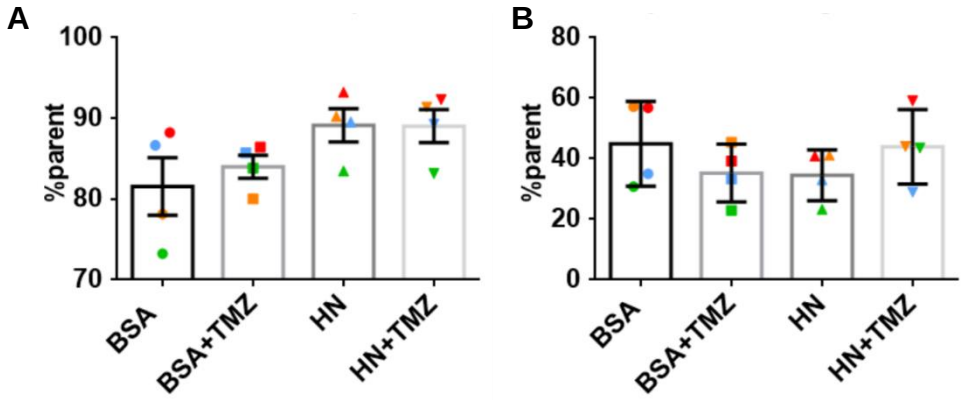

Figure S4.9.2: Live imaging shows different cell fates after Humanin treatment. (A) Result for the comparison between groups of cells that underwent at least one mitosis event in all cells. **(B)** Percentage of the cells that underwent mitosis with MTOC in first mitosis. Four independent experiments were conducted. Each symbolic dot represents percentage from one experiment, and same-color dots indicate values from the same experiment. Values are illustrated as mean ± SEM. One-way ANOVA followed by Tukey's multiple comparisons test was used to determine significant difference between groups. No significant difference was found in any group.

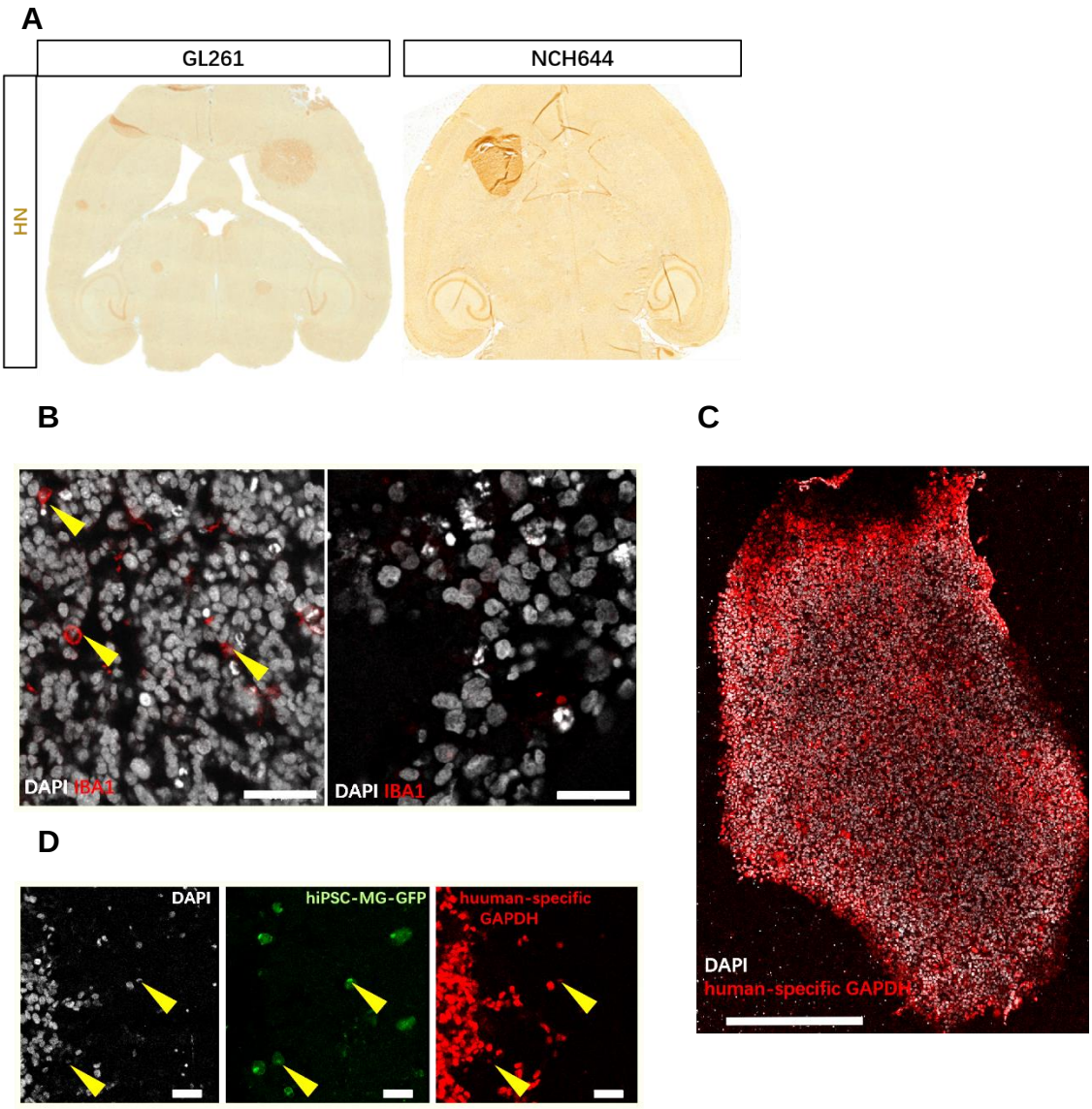

Figure S4.10: Immunostaining on mouse brain preparation with NCH644 and iPSC-MG. (A) DAB stainings show comparison of HN expression between murine glioma cell line GL261(left) and human GBM NCH644(right) in mouse xenograft models. **(B)** Mouse brain sample with NCH644 (left) shows IBA1^{+} (**red**)TAMs (**yellow arrows**) in tumor area, whereas the *ex vivo* microglia-depleted mouse brain preparations were not detected of IBA1^{+} cells (right). **(C)** Mouse *ex vivo* mouse brain inoculated with NCH644; human-specific GAPDH (**red**) indicates the tumor cells are human-originated. **(D)** Mouse *ex vivo* mouse brain inoculated with NCH644 and iPSC-MG-GFP(**green**); human-specific GAPDH (**red**) indicates the iPSC-MG(**yellow arrows**) are human-originated. Scale bar=50 µm (B, D), =500 µm (C).

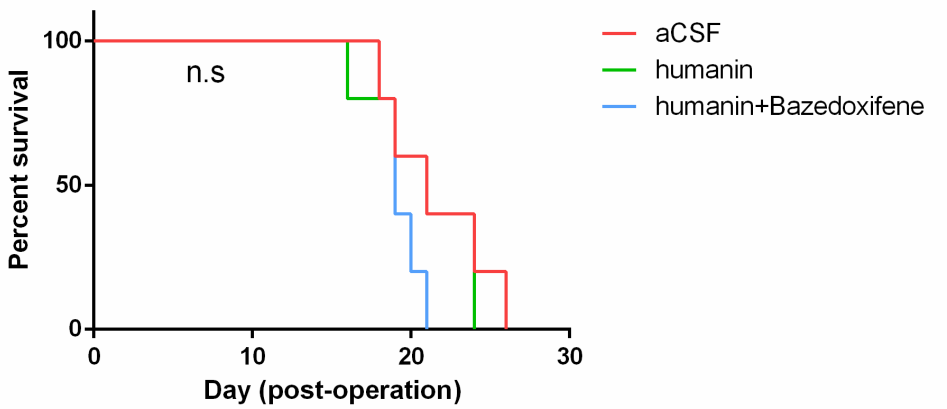

Figure S4.11a: Survival analysis for mice with Humanin peptide perfusion and BZA. No significant difference was found in the median survival time between the three groups. Log-rank (Mantel-Cox) test was used to determine statistical significance. n.s=not significant.

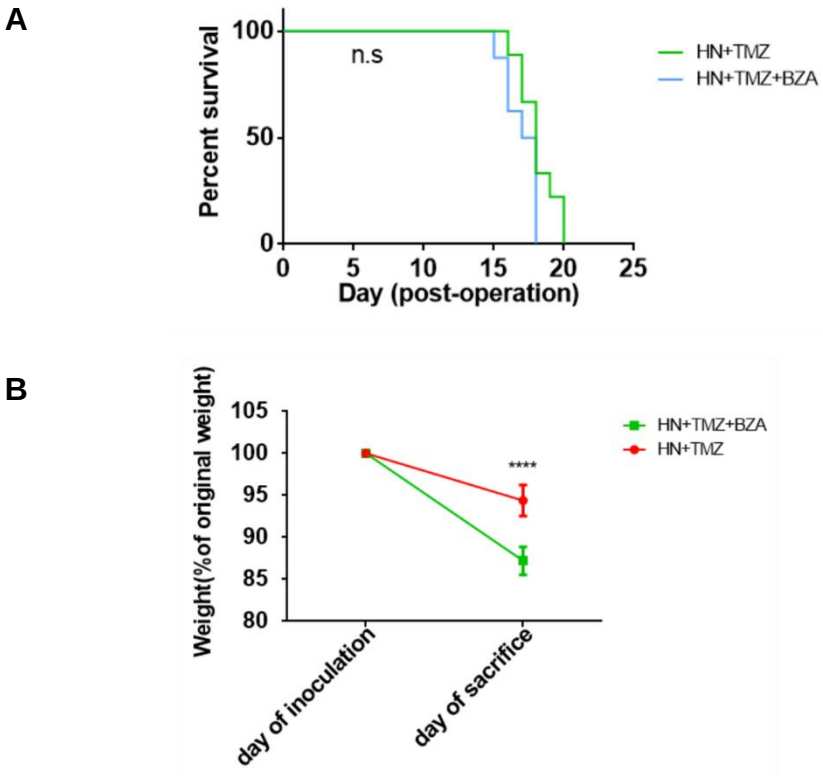

Figure S4.11c: Overall survival and health status of animals after tumor inoculation and treatment. (A) Survival comparison between HN+TMZ and HN+TMZ+BZA groups using Log-rank (Mantel-Cox) test. **(B)** Weight change of the animals from the day of inoculation to the day of sacrifice. The t test was used to determine the difference of weight change between two groups. ****$P \leq 0.0001$, n.s=not significant.

References

[1]. Kim, H.J., J.W. Park and J.H. Lee, Genetic Architectures and Cell-of-Origin in Glioblastoma. Front Oncol, 2020. 10: p. 615400.

[2]. Goodenberger, M.L. and R.B. Jenkins, Genetics of adult glioma. Cancer Genet, 2012. 205(12): p. 613-21.

[3]. Weller, M., et al., Glioma. Nat Rev Dis Primers, 2015. 1: p. 15017.

[4]. Louis, D.N., et al., The 2021 WHO Classification of Tumors of the Central Nervous System: a summary. Neuro Oncol, 2021. 23(8): p. 1231-1251.

[5]. Ostrom, Q.T., et al., CBTRUS Statistical Report: Primary Brain and Other Central Nervous System Tumors Diagnosed in the United States in 2011-2015. Neuro Oncol, 2018. 20(suppl_4): p. iv1-iv86.

[6]. Verhaak, R.G., et al., Integrated genomic analysis identifies clinically relevant subtypes of glioblastoma characterized by abnormalities in PDGFRA, IDH1, EGFR, and NF1. Cancer Cell, 2010. 17(1): p. 98-110.

[7]. Sidaway, P., CNS cancer: Glioblastoma subtypes revisited. Nat Rev Clin Oncol, 2017. 14(10): p. 587.

[8]. Neftel, C., et al., An Integrative Model of Cellular States, Plasticity, and Genetics for Glioblastoma. Cell, 2019. 178(4): p. 835-849.e21.

[9]. Hussain, S.F., et al., The role of human glioma-infiltrating microglia/macrophages in mediating antitumor immune responses. Neuro Oncol, 2006. 8(3): p. 261-79.

[10]. Hambardzumyan, D., D.H. Gutmann and H. Kettenmann, The role of microglia and macrophages in glioma maintenance and progression. Nat Neurosci, 2016. 19(1): p. 20-7.

[11]. Brandenburg, S., et al., Distinction of Microglia and Macrophages in Glioblastoma: Close Relatives, Different Tasks? Int J Mol Sci, 2020. 22(1).

[12]. Prionisti, I., et al., Harnessing Microglia and Macrophages for the Treatment of Glioblastoma. Front Pharmacol, 2019. 10: p. 506.

[13]. Chen, Z. and D. Hambardzumyan, Immune Microenvironment in Glioblastoma Subtypes. Front Immunol, 2018. 9: p. 1004.

[14]. Pombo, A.A., et al., Understanding the glioblastoma immune microenvironment as basis for the development of new immunotherapeutic strategies. Elife, 2020. 9.

[15]. Dirkse, A., et al., Stem cell-associated heterogeneity in Glioblastoma results from intrinsic tumor plasticity shaped by the microenvironment. Nat Commun, 2019. 10(1): p. 1787.

[16]. Zhang, X., et al., Chemoresistance caused by the microenvironment of glioblastoma and the corresponding solutions. Biomed Pharmacother, 2019. 109: p. 39-46.

[17]. Martinez-Lage, M., et al., Immune landscapes associated with different glioblastoma molecular subtypes. Acta Neuropathol Commun, 2019. 7(1): p. 203.

[18]. Friedrich, M., et al., Dysfunctional dendritic cells limit antigen-specific T cell response in glioma. Neuro Oncol, 2022.

[19]. Mormino, A. and S. Garofalo, Dialogue among Lymphocytes and Microglia in Glioblastoma Microenvironment. Cancers (Basel), 2022. 14(11).

[20]. Gieryng, A., et al., Immune microenvironment of gliomas. Lab Invest, 2017. 97(5): p. 498-518.

[21]. Buonfiglioli, A. and D. Hambardzumyan, Macrophages and microglia: the cerberus of glioblastoma. Acta Neuropathol Commun, 2021. 9(1): p. 54.

[22]. Cuadros, M.A., et al., Microglia and Microglia-Like Cells: Similar but Different. Front Cell Neurosci, 2022. 16: p. 816439.

[23]. Ginhoux, F., et al., Fate mapping analysis reveals that adult microglia derive from primitive macrophages. Science, 2010. 330(6005): p. 841-5.

[24]. Kierdorf, K. and M. Prinz, Microglia in steady state. J Clin Invest, 2017. 127(9): p. 3201-3209.

[25]. Yang, I., et al., The role of microglia in central nervous system immunity and glioma immunology. J Clin Neurosci, 2010. 17(1): p. 6-10.

[26]. Gomez, P.E., C. Schulz and F. Geissmann, Development and homeostasis of "resident" myeloid cells: the case of the microglia. Glia, 2013. 61(1): p. 112-20.

[27]. Amici, S.A., J. Dong and M. Guerau-de-Arellano, Molecular Mechanisms Modulating the Phenotype of Macrophages and Microglia. Front Immunol, 2017. 8: p. 1520.

[28]. Jurga, A.M., M. Paleczna and K.Z. Kuter, Overview of General and Discriminating Markers of Differential Microglia Phenotypes. Front Cell Neurosci, 2020. 14: p. 198.

[29]. Greter, M., I. Lelios and A.L. Croxford, Microglia Versus Myeloid Cell Nomenclature during Brain Inflammation. Front Immunol, 2015. 6: p. 249.

[30]. Grabert, K., et al., Microglial brain region-dependent diversity and selective regional sensitivities to aging. Nat Neurosci, 2016. 19(3): p. 504-16.

[31]. Badie, B. and J.M. Schartner, Flow cytometric characterization of tumor-associated macrophages in experimental gliomas. Neurosurgery, 2000. 46(4): p. 957-61; discussion 961-2.

[32]. Benmamar-Badel, A., T. Owens and A. Wlodarczyk, Protective Microglial Subset in Development, Aging, and Disease: Lessons From Transcriptomic Studies. Front Immunol, 2020. 11: p. 430.

[33]. Haage, V., et al., Comprehensive gene expression meta-analysis identifies signature genes that distinguish microglia from peripheral monocytes/macrophages in health and glioma. Acta Neuropathol Commun, 2019. 7(1): p. 20.

[34]. Zhang, G.X., et al., Parenchymal microglia of naive adult C57BL/6J mice express high levels of B7.1, B7.2, and MHC class II. Exp Mol Pathol, 2002. 73(1): p. 35-45.

[35]. Zhou, W., et al., Periostin secreted by glioblastoma stem cells recruits M2 tumour-associated macrophages and promotes malignant growth. Nat Cell Biol, 2015. 17(2): p. 170-82.

[36]. Feng, X., et al., Loss of CX3CR1 increases accumulation of inflammatory monocytes and promotes gliomagenesis. Oncotarget, 2015. 6(17): p. 15077-94.

[37]. Masuda, T., et al., Novel Hexb-based tools for studying microglia in the CNS. Nat Immunol, 2020. 21(7): p. 802-815.

[38]. Butovsky, O., et al., Identification of a unique TGF-beta-dependent molecular and functional signature in microglia. Nat Neurosci, 2014. 17(1): p. 131-43.

[39]. Van Hove, H., et al., A single-cell atlas of mouse brain macrophages reveals unique transcriptional identities shaped by ontogeny and tissue environment. Nat Neurosci, 2019. 22(6): p. 1021-1035.

[40]. Zeisel, A., et al., Brain structure. Cell types in the mouse cortex and hippocampus revealed by single-cell RNA-seq. Science, 2015. 347(6226): p. 1138-42.

[41]. Goldmann, T., et al., Origin, fate and dynamics of macrophages at central nervous system interfaces. Nat Immunol, 2016. 17(7): p. 797-805.

[42]. Jordao, M., et al., Single-cell profiling identifies myeloid cell subsets with distinct fates during neuroinflammation. Science, 2019. 363(6425).

[43]. Masuda, T., et al., Spatial and temporal heterogeneity of mouse and human microglia at single-cell resolution. Nature, 2019. 566(7744): p. 388-392.

[44]. Mrdjen, D., et al., High-Dimensional Single-Cell Mapping of Central Nervous System Immune Cells Reveals Distinct Myeloid Subsets in Health, Aging, and Disease. Immunity, 2018. 48(2): p. 380-395.e6.

[45]. Gieryng, A., et al., Immune microenvironment of experimental rat C6 gliomas resembles human glioblastomas. Sci Rep, 2017. 7(1): p. 17556.

[46]. Gabrusiewicz, K., et al., Characteristics of the alternative phenotype of microglia/macrophages and its modulation in experimental gliomas. PLoS One, 2011. 6(8): p. e23902.

[47]. Chen, Z., et al., Cellular and Molecular Identity of Tumor-Associated Macrophages in Glioblastoma. Cancer Res, 2017. 77(9): p. 2266-2278.

[48]. Yu, K., et al., A nonmyeloablative chimeric mouse model accurately defines microglia and macrophage contribution in glioma. Neuropathol Appl Neurobiol, 2019. 45(2): p. 119-140.

[49]. Wei, J., et al., Osteopontin mediates glioblastoma-associated macrophage infiltration and is a potential therapeutic target. J Clin Invest, 2019. 129(1): p. 137-149.

[50]. Mi, Y., et al., The Emerging Role of Myeloid-Derived Suppressor Cells in the Glioma Immune Suppressive Microenvironment. Front Immunol, 2020. 11: p. 737.

[51]. Chang, A.L., et al., CCL2 Produced by the Glioma Microenvironment Is Essential for the Recruitment of Regulatory T Cells and Myeloid-Derived Suppressor Cells. Cancer Res, 2016. 76(19): p. 5671-5682.

[52]. Flores-Toro, J.A., et al., CCR2 inhibition reduces tumor myeloid cells and unmasks a checkpoint inhibitor effect to slow progression of resistant murine gliomas. Proc Natl Acad Sci U S A, 2020. 117(2): p. 1129-1138.

[53]. Felsenstein, M., et al., CCR2 of Tumor Microenvironmental Cells Is a Relevant Modulator of Glioma Biology. Cancers (Basel), 2020. 12(7).

[54]. Kvisten, M., et al., Microglia and macrophages in human glioblastomas: A morphological and immunohistochemical study. Mol Clin Oncol, 2019. 11(1): p. 31-36.

[55]. Chen, Z., J.L. Ross and D. Hambardzumyan, Intravital 2-photon imaging reveals distinct morphology and infiltrative properties of glioblastoma-associated macrophages. Proc Natl Acad Sci U S A, 2019. 116(28): p. 14254-14259.

[56]. Stein, M., et al., Interleukin 4 potently enhances murine macrophage mannose receptor activity: a marker of alternative immunologic macrophage activation. J Exp Med, 1992. 176(1): p. 287-92.

[57]. Mills, C.D., et al., M-1/M-2 macrophages and the Th1/Th2 paradigm. J Immunol, 2000. 164(12): p. 6166-73.

[58]. Mantovani, A., et al., Macrophage polarization: tumor-associated macrophages as a paradigm for polarized M2 mononuclear phagocytes. Trends Immunol, 2002. 23(11): p. 549-55.

[59]. Funes, S.C., et al., Implications of macrophage polarization in autoimmunity. Immunology, 2018. 154(2): p. 186-195.

[60]. Mosser, D.M. and J.P. Edwards, Exploring the full spectrum of macrophage activation. Nat Rev Immunol, 2008. 8(12): p. 958-69.

[61]. Mantovani, A., A. Sica and M. Locati, Macrophage polarization comes of age. Immunity, 2005. 23(4): p. 344-6.

[62]. Martinez, F.O. and S. Gordon, The M1 and M2 paradigm of macrophage activation: time for reassessment. F1000Prime Rep, 2014. 6: p. 13.

[63]. Cui, X., et al., Hacking macrophage-associated immunosuppression for regulating glioblastoma angiogenesis. Biomaterials, 2018. 161: p. 164-178.

[64]. Carlson, M.R., et al., Relationship between survival and edema in malignant gliomas: role of vascular endothelial growth factor and neuronal pentraxin 2. Clin Cancer Res, 2007. 13(9): p. 2592-8.

[65]. Herting, C.J., et al., Tumour-associated macrophage-derived interleukin-1 mediates glioblastoma-associated cerebral oedema. Brain, 2019. 142(12): p. 3834-3851.

[66]. De Palma, M., et al., Tie2 identifies a hematopoietic lineage of proangiogenic monocytes required for tumor vessel formation and a mesenchymal population of pericyte progenitors. Cancer Cell, 2005. 8(3): p. 211-26.

[67]. Bonm, A. and S. Kesari, DNA Damage Response in Glioblastoma: Mechanism for Treatment Resistance and Emerging Therapeutic Strategies. Cancer J, 2021. 27(5): p. 379-385.

[68]. Chatterjee, N. and G.C. Walker, Mechanisms of DNA damage, repair, and mutagenesis. Environ Mol Mutagen, 2017. 58(5): p. 235-263.

[69]. Helleday, T., et al., DNA repair pathways as targets for cancer therapy. Nat Rev Cancer, 2008. 8(3): p. 193-204.

[70]. Clay, D.E. and D.T. Fox, DNA Damage Responses during the Cell Cycle: Insights from Model Organisms and Beyond. Genes (Basel), 2021. 12(12).

[71]. Aasland, D., et al., Temozolomide Induces Senescence and Repression of DNA Repair Pathways in Glioblastoma Cells via Activation of ATR-CHK1, p21, and NF-kappaB. Cancer Res, 2019. 79(1): p. 99-113.

[72]. Jackson, S.P. and J. Bartek, The DNA-damage response in human biology and disease. Nature, 2009. 461(7267): p. 1071-8.

[73]. Barciszewska, A.M., et al., A New Epigenetic Mechanism of Temozolomide Action in Glioma Cells. PLoS One, 2015. 10(8): p. e0136669.

[74]. Janssen, A. and R.H. Medema, Genetic instability: tipping the balance. Oncogene, 2013. 32(38): p. 4459-70.

[75]. Hafner, A., et al., The multiple mechanisms that regulate p53 activity and cell fate. Nat Rev Mol Cell Biol, 2019. 20(4): p. 199-210.

[76]. Hashimoto, Y., et al., Mechanisms of neuroprotection by a novel rescue factor humanin from Swedish mutant amyloid precursor protein. Biochem Biophys Res Commun, 2001. 283(2): p. 460-8.

[77]. Hashimoto, Y., et al., A rescue factor abolishing neuronal cell death by a wide spectrum of familial Alzheimer's disease genes and Abeta. Proc Natl Acad Sci U S A, 2001. 98(11): p. 6336-41.

[78]. Tajima, H., et al., Evidence for in vivo production of Humanin peptide, a neuroprotective factor against Alzheimer's disease-related insults. Neurosci Lett, 2002. 324(3): p. 227-31.

[79]. Maximov, V., et al., Mitochondrial 16S rRNA gene encodes a functional peptide, a potential drug for Alzheimer's disease and target for cancer therapy. Med Hypotheses, 2002. 59(6): p. 670-3.

[80]. Paharkova, V., et al., Rat Humanin is encoded and translated in mitochondria and is localized to the mitochondrial compartment where it regulates ROS production. Mol Cell Endocrinol, 2015. 413: p. 96-100.

[81]. Yamagishi, Y., et al., Identification of essential amino acids in Humanin, a neuroprotective factor against Alzheimer's disease-relevant insults. Peptides, 2003. 24(4): p. 585-95.

[82]. Benaki, D., et al., Solution structure of Ser14Gly-humanin, a potent rescue factor against

neuronal cell death in Alzheimer's disease. Biochem Biophys Res Commun, 2006. 349(2): p. 634-42.
[83]. Alsanousi, N., et al., Solution NMR structure and inhibitory effect against amyloid-beta fibrillation of Humanin containing a d-isomerized serine residue. Biochem Biophys Res Commun, 2016. 477(4): p. 647-653.
[84]. Arakawa, T., T. Niikura and Y. Kita, The biological activity of Humanin analogs correlates with structure stabilities in solution. Int J Biol Macromol, 2011. 49(1): p. 93-7.
[85]. Terashita, K., et al., Two serine residues distinctly regulate the rescue function of Humanin, an inhibiting factor of Alzheimer's disease-related neurotoxicity: functional potentiation by isomerization and dimerization. J Neurochem, 2003. 85(6): p. 1521-38.
[86]. Ashkenazi, A., et al., From basic apoptosis discoveries to advanced selective BCL-2 family inhibitors. Nat Rev Drug Discov, 2017. 16(4): p. 273-284.
[87]. Wolter, K.G., et al., Movement of Bax from the cytosol to mitochondria during apoptosis. J Cell Biol, 1997. 139(5): p. 1281-92.
[88]. Kariya, S., et al., Effect of humanin on decreased ATP levels of human lymphocytes harboring A3243G mutant mitochondrial DNA. Neuropeptides, 2005. 39(2): p. 97-101.
[89]. Ma, Z.W. and D.X. Liu, Humanin decreases mitochondrial membrane permeability by inhibiting the membrane association and oligomerization of Bax and Bid proteins. Acta Pharmacol Sin, 2018. 39(6): p. 1012-1021.
[90]. Guo, B., et al., Humanin peptide suppresses apoptosis by interfering with Bax activation. Nature, 2003. 423(6938): p. 456-61.
[91]. Luciano, F., et al., Cytoprotective peptide humanin binds and inhibits proapoptotic Bcl-2/Bax family protein BimEL. J Biol Chem, 2005. 280(16): p. 15825-35.
[92]. Zhai, D., et al., Humanin binds and nullifies Bid activity by blocking its activation of Bax and Bak. J Biol Chem, 2005. 280(16): p. 15815-24.
[93]. Lin, Y.W., et al., IGFBP-1 in cancer: expression, molecular mechanisms, and potential clinical implications. Am J Transl Res, 2021. 13(3): p. 813-832.
[94]. Bach, L.A., IGF-binding proteins. J Mol Endocrinol, 2018. 61(1): p. T11-T28.
[95]. LeRoith, D., J. Holly and B.E. Forbes, Insulin-like growth factors: Ligands, binding proteins, and receptors. Mol Metab, 2021. 52: p. 101245.
[96]. Johnson, M.A. and S.M. Firth, IGFBP-3: a cell fate pivot in cancer and disease. Growth Horm IGF Res, 2014. 24(5): p. 164-73.
[97]. Chen, C.H., et al., Suppression of tumor growth via IGFBP3 depletion as a potential treatment in glioma. J Neurosurg, 2019. 132(1): p. 168-179.
[98]. Baxter, R.C., Nuclear actions of insulin-like growth factor binding protein-3. Gene, 2015. 569(1): p. 7-13.
[99]. Ikonen, M., et al., Interaction between the Alzheimer's survival peptide humanin and insulin-like growth factor-binding protein 3 regulates cell survival and apoptosis. Proc Natl Acad Sci U S A, 2003. 100(22): p. 13042-7.
[100]. Njomen, E., et al., Humanin Peptide Binds to Insulin-Like Growth Factor-Binding Protein 3 (IGFBP3) and Regulates Its Interaction with Importin-beta. Protein Pept Lett, 2015. 22(10): p. 869-76.
[101]. Santosh, V., et al., Grade-specific expression of insulin-like growth factor-binding proteins-2, -3, and -5 in astrocytomas: IGFBP-3 emerges as a strong predictor of survival in patients with newly diagnosed glioblastoma. Cancer Epidemiol Biomarkers Prev, 2010. 19(6): p. 1399-408.
[102]. Lee, C., et al., IGF-I regulates the age-dependent signaling peptide humanin. Aging Cell, 2014.

13(5): p. 958-61.
[103]. Bar, J.W., et al., Prolyl endopeptidase cleaves the apoptosis rescue peptide humanin and exhibits an unknown post-cysteine cleavage specificity. Adv Exp Med Biol, 2006. 575: p. 103-8.
[104]. Le Y, P.M. Murphy and J.M. Wang, Formyl-peptide receptors revisited. Trends Immunol, 2002. 23(11): p. 541-8.
[105]. Tiffany, H.L., et al., Amyloid-beta induces chemotaxis and oxidant stress by acting at formylpeptide receptor 2, a G protein-coupled receptor expressed in phagocytes and brain. J Biol Chem, 2001. 276(26): p. 23645-52.
[106]. Ying, G., et al., Humanin, a newly identified neuroprotective factor, uses the G protein-coupled formylpeptide receptor-like-1 as a functional receptor. J Immunol, 2004. 172(11): p. 7078-85.
[107]. Muller-Newen, G., The cytokine receptor gp130: faithfully promiscuous. Sci STKE, 2003. 2003(201): p. PE40.
[108]. Wightman, S.M., et al., Bazedoxifene inhibits sustained STAT3 activation and increases survival in GBM. Transl Oncol, 2021. 14(11): p. 101192.
[109]. Hashimoto, Y., et al., Humanin inhibits neuronal cell death by interacting with a cytokine receptor complex or complexes involving CNTF receptor alpha/WSX-1/gp130. Mol Biol Cell, 2009. 20(12): p. 2864-73.
[110]. Kim, S.J., et al., The mitochondrial-derived peptide humanin activates the ERK1/2, AKT, and STAT3 signaling pathways and has age-dependent signaling differences in the hippocampus. Oncotarget, 2016. 7(30): p. 46899-46912.
[111]. Hashimoto, Y., et al., Molecular characterization of neurohybrid cell death induced by Alzheimer's amyloid-beta peptides via p75NTR/PLAIDD. J Neurochem, 2004. 90(3): p. 549-58.
[112]. Hitomi, M., et al., Asymmetric cell division promotes therapeutic resistance in glioblastoma stem cells. JCI Insight, 2021. 6(3).
[113]. Meldolesi, J., Neurotrophin Trk Receptors: New Targets for Cancer Therapy. Rev Physiol Biochem Pharmacol, 2018. 174: p. 67-79.
[114]. Jung, S.S. and W.E. Van Nostrand, Humanin rescues human cerebrovascular smooth muscle cells from Abeta-induced toxicity. J Neurochem, 2003. 84(2): p. 266-72.
[115]. Widmer, R.J., et al., Circulating humanin levels are associated with preserved coronary endothelial function. Am J Physiol Heart Circ Physiol, 2013. 304(3): p. H393-7.
[116]. Karu, I., et al., Exposure to sixty minutes of hyperoxia upregulates myocardial humanins in patients with coronary artery disease - a pilot study. J Physiol Pharmacol, 2015. 66(6): p. 899-906.
[117]. Bachar, A.R., et al., Humanin is expressed in human vascular walls and has a cytoprotective effect against oxidized LDL-induced oxidative stress. Cardiovasc Res, 2010. 88(2): p. 360-6.
[118]. Xie, Y., et al., Protection effect of [Gly14]-Humanin from apoptosis induced by high glucose in human umbilical vein endothelial cells. Diabetes Res Clin Pract, 2014. 106(3): p. 560-6.
[119]. Zhu, W.W., et al., Gly[14]-humanin inhibits ox-LDL uptake and stimulates cholesterol efflux in macrophage-derived foam cells. Biochem Biophys Res Commun, 2017. 482(1): p. 93-99.
[120]. Zacharias, D.G., et al., Humanin, a cytoprotective peptide, is expressed in carotid atherosclerotic [corrected] plaques in humans. PLoS One, 2012. 7(2): p. e31065.
[121]. Oh, Y.K., et al., Humanin preserves endothelial function and prevents atherosclerotic plaque progression in hypercholesterolemic ApoE deficient mice. Atherosclerosis, 2011. 219(1): p. 65-73.
[122]. Muzumdar, R.H., et al., Acute humanin therapy attenuates myocardial ischemia and reperfusion injury in mice. Arterioscler Thromb Vasc Biol, 2010. 30(10): p. 1940-8.

[123]. Thummasorn, S., et al., Humanin exerts cardioprotection against cardiac ischemia/reperfusion injury through attenuation of mitochondrial dysfunction. Cardiovasc Ther, 2016. 34(6): p. 404-414.
[124]. Xu, X., et al., Humanin is a novel neuroprotective agent against stroke. Stroke, 2006. 37(10): p. 2613-9.
[125]. Kumfu, S., et al., Humanin prevents brain mitochondrial dysfunction in a cardiac ischaemia-reperfusion injury model. Exp Physiol, 2016. 101(6): p. 697-707.
[126]. Xu, X., et al., Neuroprotective effect of humanin on cerebral ischemia/reperfusion injury is mediated by a PI3K/Akt pathway. Brain Res, 2008. 1227: p. 12-8.
[127]. Takeshita, Y., et al., SH3-binding protein 5 mediates the neuroprotective effect of the secreted bioactive peptide humanin by inhibiting c-Jun NH2-terminal kinase. J Biol Chem, 2013. 288(34): p. 24691-704.
[128]. Gao, G., et al., Neuroprotective effect of G(14)-humanin on global cerebral ischemia/reperfusion by activation of SOCS3 - STAT3 - MCL-1 signal transduction pathway in rats. Neurol Res, 2017. 39(10): p. 895-903.
[129]. Thummasorn, S., et al., High-dose Humanin analogue applied during ischemia exerts cardioprotection against ischemia/reperfusion injury by reducing mitochondrial dysfunction. Cardiovasc Ther, 2017. 35(5).
[130]. Kumfu, S., et al., Humanin Exerts Neuroprotection During Cardiac Ischemia-Reperfusion Injury. J Alzheimers Dis, 2018. 61(4): p. 1343-1353.
[131]. Peng, T., et al., The Neurovascular Protective Effect of S14G-Humanin in a Murine MCAO Model and Brain Endothelial Cells. IUBMB Life, 2018. 70(7): p. 691-699.
[132]. Chen, J., et al., Increased oligodendrogenesis by humanin promotes axonal remyelination and neurological recovery in hypoxic/ischemic brains. Hippocampus, 2015. 25(1): p. 62-71.
[133]. Wang, T., et al., [Gly14]-Humanin reduces histopathology and improves functional outcome after traumatic brain injury in mice. Neuroscience, 2013. 231: p. 70-81.
[134]. Wang, T., et al., [Gly14]-Humanin offers neuroprotection through glycogen synthase kinase-3beta inhibition in a mouse model of intracerebral hemorrhage. Behav Brain Res, 2013. 247: p. 132-9.
[135]. Bose, P., et al., Bortezomib for the treatment of non-Hodgkin's lymphoma. Expert Opin Pharmacother, 2014. 15(16): p. 2443-59.
[136]. Scott, K., et al., Bortezomib for the treatment of multiple myeloma. Cochrane Database Syst Rev, 2016. 4: p. CD010816.
[137]. Eriksson, E., et al., Protective role of humanin on bortezomib-induced bone growth impairment in anticancer treatment. J Natl Cancer Inst, 2014. 106(3): p. djt459.
[138]. Lue, Y., et al., Humanin analog enhances the protective effect of dexrazoxane against doxorubicin-induced cardiotoxicity. Am J Physiol Heart Circ Physiol, 2018. 315(3): p. H634-H643.
[139]. Jia, Y., et al., The effects of humanin and its analogues on male germ cell apoptosis induced by chemotherapeutic drugs. Apoptosis, 2015. 20(4): p. 551-61.
[140]. Lue, Y., et al., The Potent Humanin Analogue (HNG) Protects Germ Cells and Leucocytes While Enhancing Chemotherapy-Induced Suppression of Cancer Metastases in Male Mice. Endocrinology, 2015. 156(12): p. 4511-21.
[141]. Moreno, A.M., et al., Humanin Promotes Tumor Progression in Experimental Triple Negative Breast Cancer. Sci Rep, 2020. 10(1): p. 8542.
[142]. Gottardo, M.F., et al., Antiapoptotic factor humanin is expressed in normal and tumoral pituitary cells and protects them from TNF-alpha-induced apoptosis. PLoS One, 2014. 9(10): p. e111548.

[143]. Gottardo, M.F., et al., Baculovirus-based gene silencing of Humanin for the treatment of pituitary tumors. Apoptosis, 2018. 23(2): p. 143-151.
[144]. Mottaghi-Dastjerdi, N., et al., Genome expression analysis by suppression subtractive hybridization identified overexpression of Humanin, a target gene in gastric cancer chemoresistance. Daru, 2014. 22(1): p. 14.
[145]. Li, Min , 2020, Studies on the two secretory peptides Apelin and Humanin to target the tumor microenvironment for glioblastoma therapy. Dissertation, LMU München Faculty of Medicine.
[146]. Van Rooijen, N., The liposome-mediated macrophage 'suicide' technique. J Immunol Methods, 1989. 124(1): p. 1-6.
[147]. Muffat, J., et al., Efficient derivation of microglia-like cells from human pluripotent stem cells. Nat Med, 2016. 22(11): p. 1358-1367.
[148]. Hill, R.A., et al., Bazedoxifene - a promising brain active SERM that crosses the blood brain barrier and enhances spatial memory. Psychoneuroendocrinology, 2020. 121: p. 104830.
[149]. Viel, T., et al., Optimizing glioblastoma temozolomide chemotherapy employing lentiviral-based anti-MGMT shRNA technology. Mol Ther, 2013. 21(3): p. 570-9.
[150]. Lertkiatmongkol, P., et al., Endothelial functions of platelet/endothelial cell adhesion molecule-1 (CD31). Curr Opin Hematol, 2016. 23(3): p. 253-9.
[151]. Winkler, E.A., R.D. Bell and B.V. Zlokovic, Pericyte-specific expression of PDGF beta receptor in mouse models with normal and deficient PDGF beta receptor signaling. Mol Neurodegener, 2010. 5: p. 32.
[152]. Bleeker, F.E., et al., IDH1 mutations at residue p.R132 (IDH1(R132)) occur frequently in high-grade gliomas but not in other solid tumors. Hum Mutat, 2009. 30(1): p. 7-11.
[153]. Arakawa, T., T. Niikura and Y. Kita, Inactive C8Ahumanin analog is as stable as a potent S14Ghumanin analog. Mol Med Rep, 2014. 9(1): p. 375-9.
[154]. Lee, C., K. Yen and P. Cohen, Humanin: a harbinger of mitochondrial-derived peptides? Trends Endocrinol Metab, 2013. 24(5): p. 222-8.
[155]. Kang, S., et al., Targeting Interleukin-6 Signaling in Clinic. Immunity, 2019. 50(4): p. 1007-1023.
[156]. Shi, Y., et al., Tetraspanin CD9 stabilizes gp130 by preventing its ubiquitin-dependent lysosomal degradation to promote STAT3 activation in glioma stem cells. Cell Death Differ, 2017. 24(1): p. 167-180.
[157]. Shi, Y., et al., Ibrutinib inactivates BMX-STAT3 in glioma stem cells to impair malignant growth and radioresistance. Sci Transl Med, 2018. 10(443).
[158]. Brantley, E.C. and E.N. Benveniste, Signal transducer and activator of transcription-3: a molecular hub for signaling pathways in gliomas. Mol Cancer Res, 2008. 6(5): p. 675-84.
[159]. Filppu, P., et al., CD109-GP130 interaction drives glioblastoma stem cell plasticity and chemoresistance through STAT3 activity. JCI Insight, 2021. 6(9).
[160]. Miningou, N. and K.T. Blackwell, The road to ERK activation: Do neurons take alternate routes? Cell Signal, 2020. 68: p. 109541.
[161]. Bao, S., et al., Disruption of the Rad9/Rad1/Hus1 (9-1-1) complex leads to checkpoint signaling and replication defects. Oncogene, 2004. 23(33): p. 5586-93.
[162]. Lindner, A.K., et al., HUS1 as a Potential Therapeutic Target in Urothelial Cancer. J Clin Med, 2022. 11(8).
[163]. Pereira, C., et al., ATR signaling in mammalian meiosis: From upstream scaffolds to

downstream signaling. Environ Mol Mutagen, 2020. 61(7): p. 752-766.
[164]. Eich, M., et al., Contribution of ATM and ATR to the resistance of glioblastoma and malignant melanoma cells to the methylating anticancer drug temozolomide. Mol Cancer Ther, 2013. 12(11): p. 2529-40.
[165]. Foote, K.M., et al., Discovery and Characterization of AZD6738, a Potent Inhibitor of Ataxia Telangiectasia Mutated and Rad3 Related (ATR) Kinase with Application as an Anticancer Agent. J Med Chem, 2018. 61(22): p. 9889-9907.
[166]. Frosina, G., et al., ATR kinase inhibitors NVP-BEZ235 and AZD6738 effectively penetrate the brain after systemic administration. Radiat Oncol, 2018. 13(1): p. 76.
[167]. Foote, K.M., et al., Discovery of 4-{4-[(3R)-3-Methylmorpholin-4-yl]-6-[1-(methylsulfonyl)cyclopropyl]pyrimidin-2-y l}-1H-indole (AZ20): a potent and selective inhibitor of ATR protein kinase with monotherapy in vivo antitumor activity. J Med Chem, 2013. 56(5): p. 2125-38.
[168]. Niida, H. and M. Nakanishi, DNA damage checkpoints in mammals. Mutagenesis, 2006. 21(1): p. 3-9.
[169]. Barbie, D.A., et al., Systematic RNA interference reveals that oncogenic KRAS-driven cancers require TBK1. Nature, 2009. 462(7269): p. 108-12.
[170]. Subramanian, A., et al., Gene set enrichment analysis: a knowledge-based approach for interpreting genome-wide expression profiles. Proc Natl Acad Sci U S A, 2005. 102(43): p. 15545-50.
[171]. Vitovcova, B., et al., Biology of Glioblastoma Multiforme-Exploration of Mitotic Catastrophe as a Potential Treatment Modality. Int J Mol Sci, 2020. 21(15).
[172]. Loeper, S., et al., Frequent mitotic errors in tumor cells of genetically micro-heterogeneous glioblastomas. Cytogenet Cell Genet, 2001. 94(1-2): p. 1-8.
[173]. Asano, T., et al., Highly efficient gene transfer into primate embryonic stem cells with a simian lentivirus vector. Mol Ther, 2002. 6(2): p. 162-8.
[174]. Essers, J., et al., Dynamics of relative chromosome position during the cell cycle. Mol Biol Cell, 2005. 16(2): p. 769-75.
[175]. Courtois, A., P. Solc and T.S. Kitajima, Triple-Color Live Imaging of Mouse Oocytes. Methods Mol Biol, 2018. 1818: p. 89-97.
[176]. Priyanga, J., G. Guha and D. Bhakta-Guha, Microtubule motors in centrosome homeostasis: A target for cancer therapy? Biochim Biophys Acta Rev Cancer, 2021. 1875(2): p. 188524.
[177]. Klaasen, S.J. and G. Kops, Chromosome Inequality: Causes and Consequences of Non-Random Segregation Errors in Mitosis and Meiosis. Cells, 2022. 11(22).
[178]. Jones, S.M. and A. Kazlauskas, Growth factor-dependent signaling and cell cycle progression. FEBS Lett, 2001. 490(3): p. 110-6.
[179]. Pihan, G.A., Centrosome dysfunction contributes to chromosome instability, chromoanagenesis, and genome reprograming in cancer. Front Oncol, 2013. 3: p. 277.
[180]. Paz, J. and J. Luders, Microtubule-Organizing Centers: Towards a Minimal Parts List. Trends Cell Biol, 2018. 28(3): p. 176-187.
[181]. Mateuca, R., et al., Chromosomal changes: induction, detection methods and applicability in human biomonitoring. Biochimie, 2006. 88(11): p. 1515-31.
[182]. Littler, S., et al., Oncogenic MYC amplifies mitotic perturbations. Open Biol, 2019. 9(8): p. 190136.
[183]. Pocock, J.M. and T.M. Piers, Modelling microglial function with induced pluripotent stem

cells: an update. Nat Rev Neurosci, 2018. 19(8): p. 445-452.
[184]. Balmus, G., et al., HUS1 regulates in vivo responses to genotoxic chemotherapies. Oncogene, 2016. 35(5): p. 662-9.
[185]. Roos, W.P., et al., Apoptosis in malignant glioma cells triggered by the temozolomide-induced DNA lesion O6-methylguanine. Oncogene, 2007. 26(2): p. 186-97.
[186]. Kim, Y., et al., Perspective of mesenchymal transformation in glioblastoma. Acta Neuropathol Commun, 2021. 9(1): p. 50.
[187]. Hara, T., et al., Interactions between cancer cells and immune cells drive transitions to mesenchymal-like states in glioblastoma. Cancer Cell, 2021. 39(6): p. 779-792.e11.
[188]. Filppu, P., et al., CD109-GP130 interaction drives glioblastoma stem cell plasticity and chemoresistance through STAT3 activity. JCI Insight, 2021. 6(9).
[189]. Louis, D.N., et al., The 2007 WHO classification of tumours of the central nervous system. Acta Neuropathol, 2007. 114(2): p. 97-109.
[190]. Louis, D.N., et al., The 2016 World Health Organization Classification of Tumors of the Central Nervous System: a summary. Acta Neuropathol, 2016. 131(6): p. 803-20.
[191]. Zhao, Z., et al., Establishment and Dysfunction of the Blood-Brain Barrier. Cell, 2015. 163(5): p. 1064-1078.
[192]. Schiffer, D., et al., Glioblastoma: Microenvironment and Niche Concept. Cancers (Basel), 2018. 11(1).
[193]. Vasudev, N.S. and A.R. Reynolds, Anti-angiogenic therapy for cancer: current progress, unresolved questions and future directions. Angiogenesis, 2014. 17(3): p. 471-94.
[194]. Bergers, G. and S. Song, The role of pericytes in blood-vessel formation and maintenance. Neuro Oncol, 2005. 7(4): p. 452-64.
[195]. Zhou, W., et al., Targeting Glioma Stem Cell-Derived Pericytes Disrupts the Blood-Tumor Barrier and Improves Chemotherapeutic Efficacy. Cell Stem Cell, 2017. 21(5): p. 591-603.e4.
[196]. Ostrowski, P.R., et al., Hemorrhage in brain tumor – An unresolved issue. Brain Hemorrhages, 2022. 3(2):p. 98-102..
[197]. Pressman, E., D. Penn and N.J. Patel, Intracranial Hemorrhage from Meningioma: 2 Novel Risk Factors. World Neurosurg, 2020. 135: p. 217-221.
[198]. Wong, E.T. and S. Brem, Antiangiogenesis treatment for glioblastoma multiforme: challenges and opportunities. J Natl Compr Canc Netw, 2008. 6(5): p. 515-22.
[199]. Gordan, J.D., et al., HIF-2alpha promotes hypoxic cell proliferation by enhancing c-myc transcriptional activity. Cancer Cell, 2007. 11(4): p. 335-47.

Acknowledgement

I want to express my gratitude to my supervisor Prof. Dr. Rainer Glass. I am grateful that he gave me the chance to work in his lab where I gained very precious scientific experience. I also want to thank Dr. Roland Kaelin and our technician Ms. Stefanie Lange for their suggestions and help. I appreciate the funding from Guangzhou Elite Project, without their support I would not have had chance to even start my study in Germany. Besides, I want to give my thank to our co-operators: Dr. Charlotte Flüh's group from MDC for providing the *ex vivo* cultured mouse brain with human hGBM and hiPSC-MG, and Dr. Krishna Bhat from MD Anderson Cancer Center for performing the Western Blotting experiments. In addition, I want to thank my previous and present colleagues for their accompany and help, they are Dr. Li Min, Dr. Cai Linzhi, Dr. Zhang Huabin, Dr. Zhao Dongxu, Deivi Barci, Song Wangyang, Li Gen and Zhou Ding. Helps from Dr. Steffen Dietzel and his colleagues from imaging faculty, Laura Dengler from AG Baumgarten, and Dr. Denise Messerer from AG Shultz are also appreciated. At last, I want to thank my family for supporting me to do the thing I like, especially my husband Chen Wei, he gave me lots of courage which is of great importance for me to go through all the difficulties. Thank my dear mum, she is always the biggest spiritual lighthouse for me.

The gate to the mystery of science has just opened in front of me, I hope I can always keep my original curiosity toward this world, think deep, work hard, discover the truth, and help the people in pain with tumor.

Affidavit

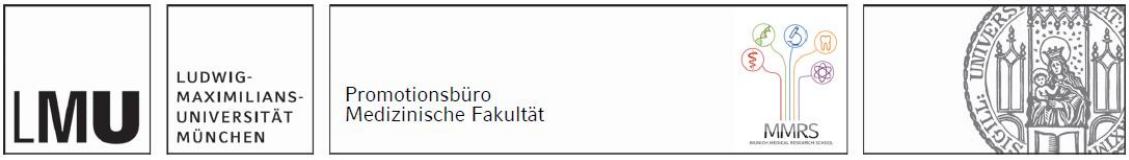

Affidavit

Cheng, Jiying

Surname, first name

123, Huangpudadaozhong

Street

510000, Guangzhou, China

Zip code, town, country

I hereby declare, that the submitted thesis entitled:

Paracrine humanin signaling promotes glioma chemoresistance

is my own work. I have only used the sources indicated and have not made unauthorised use of services of a third party. Where the work of others has been quoted or reproduced, the source is always given.

I further declare that the dissertation presented here has not been submitted in the same or similar form to any other institution for the purpose of obtaining an academic degree.

Guangzhou
14.11.2023 Cheng Jiying

place, date Signature doctoral candidate

List of publications

1. Volmar MNM, **Cheng J**, Alenezi H, Richter S, Haug A, Hassan Z, Goldberg M, Li Y, Hou M, Herold-Mende C, Maire CL, Lamszus K, Flüh C, Held-Feindt J, Gargiulo G, Topping GJ, Schilling F, Saur D, Schneider G, Synowitz M, Schick JA, Kälin RE, Glass R. Cannabidiol converts NF-κB into a tumor suppressor in glioblastoma with defined antioxidative properties. Neuro Oncol. 2021 Nov 2;23(11):1898-1910. doi: 10.1093/neuonc/noab095. PMID: 33864076; PMCID: PMC8563328.

2. Kälin RE, Cai L, Li Y, Zhao D, Zhang H, **Cheng J**, Zhang W, Wu Y, Eisenhut K, Janssen P, Schmitt L, Enard W, Michels F, Flüh C, Hou M, Kirchleitner SV, Siller S, Schiemann M, Andrä I, Montanez E, Giachino C, Taylor V, Synowitz M, Tonn JC, von Baumgarten L, Schulz C, Hellmann I, Glass R. TAMEP are brain tumor parenchymal cells controlling neoplastic angiogenesis and progression. Cell Syst. 2021 Mar 17;12(3):248-262.e7. doi: 10.1016/j.cels.2021.01.002. Epub 2021 Feb 15. PMID: 33592194.

3. Poster: Paracrine humanin signaling promotes glioma chemoresistance, 11th Brain Tumor Meeting 2022, Berlin